Validation of New Control Concepts by Advanced Fluid-Structure Interaction Tools

Agreement n.:	308974
Duration	November 2012 – October 2017
Co-ordinator:	DTU Wind

Support by:

PROPRIETARY RIGHTS STATEMENT
This document contains information, which is proprietary to the “INNWIND.EU” Consortium. Neither this document nor the information contained herein shall be used, duplicated or communicated by any means to any third party, in whole or in parts, except with prior written consent of the “INNWIND.EU” consortium.

Document information

Document Name:	Validation of new control concepts by advanced fluid-structure interaction tools
Document Number:	
Author:	**Eva Jost, Athanasios Barlas, Vasilis Riziotis, Sachin T. Navalkar**
Document Type	Report
Dissemination level	PU
Review:	**Jan-Willem van Wingerden and Flemming Rasmussen**
Date:	**02-09-2015**
WP:	**2**
Task:	**3**
Approval:	Approved by WP Leader

EXECUTIVE SUMMARY

The general objective of INNWIND Work Package 2.3 is the evaluation of the technology-readiness level of advanced load control strategies primarily targeting the attenuation of rotor loads. In the previous deliverable, a preliminary analysis of various load control techniques was done, and the trailing edge flap control mechanism was downselected as the most promising and technically feasible solution. The integration of this mechanism with conventional rotor design is evaluated in terms of its load reduction potential using different numerical tools.

As a first step, a high-fidelity investigation of a rotor instrumented with trailing-edge flaps is done using a Computational Fluid Dynamics (CFD) model, which solves the Reynold's-averaged Navier-Stokes (RANS) equations numerically. Mesh generation for the CFD solution is automated, and the flap motion is simulated via grid deformation. As an initial check, a 2D CFD model of a representative aerofoil with a trailing edge flap is simulated and successfully validated against previous results. It is seen that with an increasing flap actuation frequency, the time lag between actuation and aerodynamic forces increases.

This is also observed in a 3D CFD case where a periodic 120° model of the rotor is simulated at the rated wind speed of 11.4 m/s and an above-rated wind speed of 19 m/s. For actuation frequency equal to the rotational frequency (1P), no hysteresis in aerodynamic response is observed at rated wind speed, however higher frequencies show increasing phase shifts, indicating that there exists an aerodynamic bandwidth for trailing edge flap actuators. This bandwidth increases with increasing wind speed. A typical load control signal is also simulated in a full 3D CFD model. It is observed that sudden changes in the flap actuation lead to large aerodynamic (and hence structural) forces.

Next, the potential of flap control was explored using the aeroelastic code hGAST extended with trailing edge flap actuators. The unsteady aerodynamics of the flap were accounted for using inviscid corrections and a dynamic stall model. Different chordwise and spanwise sizes of the flap were investigated, with larger sizes showing increased load reduction potential. Two different flap control methods were studied: a conventional cyclic control method and a direct individual control method. It was seen that the direct method shows moderate load reductions with lower flap activity. On the other hand, it also leads to a small decrease in extreme loads. Overall, the control methods showed load reductions of 6-18%.

Different levels of turbulence intensity were investigated and it was shown that load reductions are higher at lower turbulence levels. The use of trailing edge flaps was extended by demonstrating that extreme idling loads can be reduced through flap control for high wind speed conditions.

The combination of flap control with pitch control was studied using the turbine certification aeroelastic code GH Bladed™ which implements flaps by using direct 2D aerodynamic force modifications. The conventional cyclic control in this case, with a small spanwise flap length yields load reductions of the order of 6.5-10%. By separating the frequency of actuation of the pitch and the flap actuators, it is shown that pitch bearing

damage can be minimised while maximally exploiting the limited control authority of the trailing edge flaps. Then, a self-tuning algorithm (Subspace Predictive Repetitive Control) is developed and validated that is able to account for changes in the dynamics of the flap actuators, while maintaining optimal control performance.

Next, the aeroelastic code HAWC2 is used to validate the load reduction potential of trailing edge flaps combined with individual pitch control for the case of a flap actuator of increased spanwise size. Significant load reductions upto 25% are demonstrated, however the controller may cause increased loading in a few extreme load cases, such that the trade-off between fatigue damage and extreme loading needs to be given further consideration.

To put the individual results in perspective, the aerodynamic response of all three engineering models is compared with that of the high-fidelity CFD simulations. It is observed that the aerodynamic forces, both steady and unsteady, in the engineering models and in CFD, compare well with each other. While the axial forces show close correspondence, the engineering models tend to overpredict the tangential forces on account of the inherent 2D nature of the engineering models, alleviated to some extent by the corrections in the NTUA code. Finally, since the CFD model lacks a coupled structural model, the power and thrust variations are overpredicted, however they compare well across the engineering models.

In conclusion, this document validates the fidelity of engineering models in evaluating the load reduction potential of trailing edge flap actuators. Further, with various design extensions, a lifetime blade load reduction potential from 8-25% is conclusively demonstrated from numerical simulations. The next step is experimental validation of the results presented in this deliverable.

TABLE OF CONTENTS

EXECUTIVE SUMMARY 4

TABLE OF CONTENTS 7

1 INTRODUCTION 9
  1.1 Background 9
  1.2 The Aeroelastic Reference Case 10
  1.3 Design Load Cases 10
  1.4 References 11

2 VALIDATION 1: COMPUTATIONAL FLUID DYNAMICS (USTUTT-IAG) 12
  2.1 Introduction 12
  2.2 Simulation process chain 12
  2.3 Flap modelling through grid deformation 13
  2.4 Validation studies in 2D 15
  2.5 Validation studies of the flap model in 3D 17
  2.6 Simulation of reference cases 21
  2.7 Modifications of the flap signal 31
  2.8 Conclusions/Outlook 32
  2.9 References 33

3 VALIDATION 2: LOAD ALLEVIATION CAPABILITIES OF AN SMA SHAPE MORPHING CONCEPT (NTUA) 34
  3.1 Aeroelastic load control simulations 34
  3.2 Design load cases 34
  3.3 Modelling Environment and Configuration 34
  3.4 Controllers 39
  3.5 Results Normal Operation 41
  3.6 Results Idling Operation 53
  3.7 Conclusions 55
  3.8 References 56

4 VALIDATION 3: ENGINEERING MODEL SIMULATIONS WITH COMBINED ACTIVE FLAP AND INDIVIDUAL PITCH CONTROL, EXTENSIONS FOR ADAPTIVITY (TUD) 57
  4.1 Introduction 57
  4.2 Frequency Separation of Pitch and Flap Control 69
  4.3 Subspace Predictive Repetitive Control for IFC 73
  4.4 Conclusions 79
  4.5 References 80

5 VALIDATION 4: DESIGN LOAD BASIS AEROELASTIC SIMULATIONS WITH INDIVIDUAL FLAP/PITCH CONTROL (DTU) 81

5.1 Aeroelastic load control simulations 81
5.2 Modelling Environment and Configuration 81
5.3 Post-processing and Sensors 81
5.4 Controllers 82
5.5 Results 84
5.6 Conclusions 97
5.7 References 98

6 VALIDATION 5: PURE ROTOR AERODYNAMIC SIMULATIONS WITH PRESCRIBED FLAP (ALL) 99
6.1 Pure Rotor Aerodynamic Simulations 99
6.2 Operating Cases 99
6.3 Modelling Environment and Configuration 99
6.4 Results 100
6.5 Conclusions 123

7 CONCLUSIONS 125

1 INTRODUCTION

1.1 Background

The need for reducing the cost of wind energy, especially in the resource-rich offshore locations, has been a driving factor in the increasing size of modern wind turbines. However, an increased turbine size also increases the component loading, especially dynamic (fatigue) loading, pushing it to beyond the limits of engineering experience. It is the objective of the INNWIND program to investigate innovations in wind technology that can allow for an increase in the rating of turbines while circumventing an exponential increase in the turbine loads and their concomitant material costs.

One of the primary cost drivers in wind turbines is the rotor design. The rotor blades themselves, on account of the complex aerostructural design and glass-fibre/carbon-fibre composition, form an important part of turbine costs that is sought to be minimised by limiting dynamic blade loads. Further, the blade loads cascade down through the entire structure, as such, blade load attenuation can prove beneficial in reducing total turbine costs, in terms of initial outlay as well as maintenance cost. Therefore, the objective of INNWIND Task 2 is the investigation of rotor design concepts that can alleviate blade loads in a passive (structural) or active (aeroservoelastic) manner.

INNWIND Task 2.3 devotes its attention to the control implications of these concepts. In the previous deliverable, several different rotor (re)design concepts for blade load reduction were explored in terms of advantages and limitations. The focus of the deliverable was on the technical feasibility and readiness level of various technologies for their implementation in the field. It was concluded that active trailing edge flaps, that can modify aerofoil camber in response to varying wind loads, show the highest technology-readiness level. Other concepts, namely passive trailing-edge flaps and material/geometric coupling, need further validation in the simulation and experimental environment.

The advantages and limitations of shape memory actuators for the application of wind turbine blade trailing edge flaps was discussed in the deliverable. Significant potential for blade load reduction is expected, technical limitations include a moderately low fatigue lifetime of the material, and the low bandwidth without active cooling. Trailing edge flaps, using other smart materials, have already been demonstrated in wind tunnels on wind turbine scaled prototypes, and in one instance, on a small-scale field turbine using large conventional actuators.


Figure 1: Wind turbine with trailing edge flaps

It is necessary to understand the fundamental behaviour of trailing edge flaps and the uncertainties associated in order to be able to integrate these smart actuators with conventional aeroelastic rotor design. Hence, as a first step, in this report, the current numerical tools for wind turbine analysis, extended such that they are able to incorporate the new actuators are validated for turbine lifetime load cases. These engineering tools are expected to be able to model the influence of the actuators to an acceptable degree of fidelity, specifically capturing the effect of actuator variations on the load profile of the wind turbines. Further, they are required to run within a reasonable amount of time such that design iterations can be carried out efficiently. The tools developed are then compared against a high-fidelity benchmark, such as a Computational Fluid Dynamics (CFD) model of a turbine to ensure the requisite level of accuracy.

Next, in this report, different control approaches and different actuator configurations are validated against each other using the engineering tools in order to understand their unique benefits and drawbacks. Finally, given the validated numerical tools for the investigation of trailing edge flap actuators, a conclusion is drawn regarding their load alleviation potential.

For ease of comparison, all numerical simulations are run on the same reference turbine, using comparable actuators and design load cases, as defined in the following sections.

1.2 The Aeroelastic Reference Case

The turbine model used to validate the combined flap and pitch controller is the Innwind 10 MW turbine, which is a reference turbine with a rotor diameter of 178.3 m, described fully in [1]. An overview of turbine properties can be found in Table 1.

Table 1: Main parameters of the DTU 10 MW turbine

DTU 10MW Reference Wind Turbine	
Rated power	10 MW
Rotor diameter	178.3 m
Rated rotor speed	9.6 rpm
Rated wind speed	11.4 m/s
Cut-in, cut-out wind speed	4 m/s, 25 m/s
Gearbox Ratio	50.0
Pitch Rate Limit	10°/s

A trailing-edge flap, with 2D aerodynamic characteristics as described in the previous chapter, was implemented outboard on each of the three blades. Based on the work of [2], the spanwise and chordwise extent of the flap was determined. The overall dimensions and location of the trailing edge flap are indicated in Table 2.

Table 2: Flap Configuration

Flap configuration	
Chordwise extension	10%
Deflection angle limits	±10°
Spanwise length	8.63m (10% blade length)
Spanwise location	59.59m-68.23m (from blade root)
Airfoil	FFA-W3-241
Max ΔC_l	0.4
Deflection rate limit	100°/s
Actuator time constant	100ms

1.3 Design Load Cases

A subset of the DLB defined in DTU Wind Energy [3] is implemented, which is based on the third edition of the IEC 61400-1 standard [4] and covers the typical cases for assessment of extreme and fatigue loads on the turbine components. The normal power production (DLC 1.2) cases are simulated for above rated operation, which is relevant for evaluation of the fatigue load alleviation potential of active flaps. The main parameters are shown in Table 3. Six turbulence seeds per wind speed are used, with no yaw misalignment or upflow.

Table 3: Normal Power Production Load Cases

Design Load Case	DLC 1.2
Wind Speed	12 : 2 : 26 m/s
Wind Direction	0 °
Turbulence	NTM
Wind shear exponent	0.2
Fault	None
Simulation Time	600 s

For cases with flap controls, the standard list of DLCs is augmented with some additional cases, simulating reference fault cases related to the flap system in Table 4.

Table 4: Power Production Load Cases with Fault

Design Load Case	DLC 2.2
Wind Speed	12 : 2 : 26 m/s
Wind Direction	0 °
Turbulence	NTM
Wind shear exponent	0.2
Fault	Flap runaway symmetric
	Flap runaway asymmetric
	Flap time constant x5
Simulation Time	600 s

Further details on the exact implementation of the wind turbine model and the load cases investigated varies with the turbine simulation environment used, and will be explained more clearly in the following chapters. The last chapter compares the aeroelastic behaviour of the trailing edge flaps in each engineering model against the response observed in a rotating CFD implementation of the reference turbine with trailing edge flaps.

1.4 References

[1] Bak, C. et al Description of the DTU 10 MW Reference Wind Turbine, Technical report, DTU Vindenergi-I-0092, 2013.

[2] Madsen, H. A. et al., Towards an industrial manufactured morphing trailing edge flap system for wind turbines, Proceedings of EWEC 2014, Barcelona, Spain, 2014.

[3] Hansen, M. H. et al., Design Load Basis for onshore turbines, Technical report, DTU Vindenergi-E-0174(EN), 2015 (orbit.dtu.dk).

[4] IEC. IEC 61400-1. Wind turbines – Part 1: Design Requirements, 2005.

2 VALIDATION 1: COMPUTATIONAL FLUID DYNAMICS (USTUTT-IAG)

2.1 Introduction

The aerodynamics of wind turbines have become one of the main research topics at the Institute of Aerodynamics and Gas Dynamics (IAG) of the University of Stuttgart (USTUTT). Time and scale resolving CFD simulations with a fully resolved rotor are performed to gain knowledge of the behaviour of the unsteady flow around the turbine. Current research focus points are for example: the impact of inflow turbulence, complex terrain on transient loads and studies on passive and active load reduction.

Within the Innwind project, the potential of load reduction with active trailing edge flaps was studied. For this purpose, a variety of simulations have been performed with different complexities and setups.

2.2 Simulation process chain

Over the last years, a process chain for the simulation of wind turbines has been developed at the IAG [1]. The main part constitutes the CFD code FLOWer, which was developed by the German Aerospace Center (DLR) within the MEGAFLOW project [2] in the late 1990s. In recent years this code has been continually enhanced specifically for the needs of wind turbine applications by the IAG. Different tools have been developed for pre- and post-processing.

FLOWer is a compressible code that solves the three-dimensional, Reynolds-averaged Navier-Stokes equations in integral form. The numerical scheme is based on a finite-volume formulation for block-structured grids. To determine the convective fluxes, a second order central discretisation with artificial damping is used, also called the Jameson-Schmidt-Turkel (JST) method. The time integration is accomplished by an explicit multi-stage scheme. In the case of steady computations, convergence can be accelerated by implicit residual smoothing, local time stepping and the Multigrid algorithm. Time-accurate simulations make use of the Dual-time-stepping method as an implicit scheme. The pseudo time iterations can be accelerated with the same methods as steady computations. To close the Navier Stokes equation system, several state-of-the-art turbulence models can be applied, as for example the model by Menter [3]. The turbulence model equations are solved separately from the main flow equations using a fully implicit time integration method.

There are two main code features for the simulation of wind turbines. The ROT module for moving and rotating reference frames in combination with the CHIMERA technique [4] for overlapping meshes allows body motions relative to each other in time-accurate simulations. FLOWer is optimized for parallel computing and uses a Message-Passing Interface (MPI).

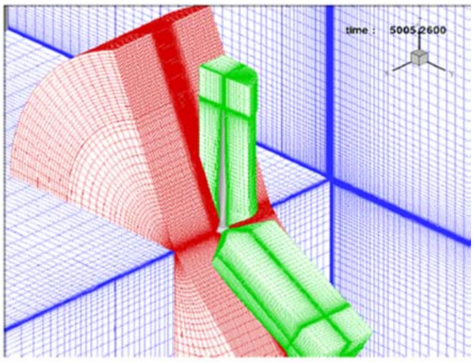

Figure 2: CHIIMERA grid

Grid generation is widely automated. The generation of the blade grid is conducted with Automesh, a script for the commercial grid generator Gridgen by Pointwise® developed at the IAG. As can be seen in Figure 2, the blade grids are of C-type with a tip block and coning towards the blade root. Depending on the simulation purpose, the blade grid is embedded into different background grids. In case of pure rotor simulations, a 120 degree model with periodic boundary conditions is used. In this work, the harmonic flap deflections study was performed within this environment. For the simulation of the full model, the turbine is placed in a rectangular shaped background grid. To save computational cells and effort the principle of hanging grid nodes is used. Spinner, nacelle, and in case of the full model, the tower are individually meshed with the commercial grid generation software Pointwise by Pointwise®.

The simulation methodology differs from case to case. For simulations in the 120 degree model, it is possible to start with a steady simulation for fast initial convergence. To resolve transient effects like those for example at the blade root, the computation is then restarted in unsteady mode. This approach is not possible for the full model. The simulation is conducted in unsteady mode from the start, which leads to a longer convergence time as the flow field needs to develop within the computation area. In all cases of this study, the stiff straight blade is regarded without any fluid-structure iterations.

On the post-processing side, several scripts are available for the evaluation of the simulation. The two tools relevant to this work are explained in detail in the following section to better understand the results.

Load determination

For the calculation of the integral characteristic values such as power and thrust, the pressure and friction coefficients are simply integrated over the surface area and transformed into the desired coordinate system. The computation of moments is done in a similar manner, also considering the position of the cells.

Distributed forces over the blade span are also regarded within this work. One way to calculate these forces is to integrate each spanwise section separately over its surface area and then divide the result by the radial width of the regarded section. In the following section, this force distribution will be denoted as sectional load. Another way to compute distributed forces is to integrate pressure and friction along a spanwise cut as line integral. In the following section, this methodology is cited as line load. Although these forces are similar, the sectional load tends to be slightly higher due the fact that radial width is smaller than the spanwise surface lines. For the comparison to blade element methods sectional loads are more suitable.

Determination of the angle of attack and aerodynamic coefficients

Angles of attack and aerodynamic coefficients cannot directly be extracted from the 3D CFD solution as the local angle of attack is influenced by the induction field. Different models have been developed to compute these values. Within this work, the first method by Shen, Hansen and Sørensen [5] is used, in which the induced velocity is determined through modelling a point circulation at the center of pressure of the airfoil. The model has been implemented and validated in [6].

2.3 Flap modelling through grid deformation

Within the last years, a new grid deformation algorithm based on radial basis functions (RBF) has been developed at the IAG and was implemented into FLOWer [7]. This new method is much more flexible than previous implementations as it also allows the deformation of multiple overlapping grids based on arbitrary defined surfaces. As deformation input an un-deformed and deformed surface set is needed to compute the deformation coefficients which will be applied on the grids.
This tool can also be used for the simulation of leading or trailing edge flaps. Therefore, the un-deformed and deformed surface as shown in Figure 3 serves as input. In case of a rigid flap which has defined hinge point, the deformed surface is generated during runtime based on the geometric specifications of hinge axis and flap angle. A quaternion rotation is then performed to deflect the flap. Unsteady simulations can therefore easily be conducted by simply specifying the flap motion kinematics.

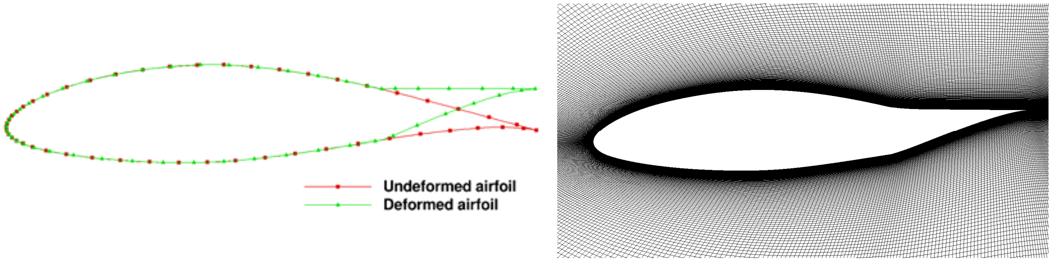

Figure 3: Flap deformation

For the Innwind project, a morphing flap deformation has been implemented into the code. It combines the models of two articles by Daynes [8] and Madsen [9], in which a polynomial is used to describe the form of the deflected flap.

$$w = \varphi(x)\beta \qquad \varphi(x) = \begin{cases} 0, & 0 \le x < c-b \\ \dfrac{(c-x-b)^n}{b^{n-1}}, & c-b \le x \le c \end{cases}$$

In this formula, c constitutes the chord length, b the flap length and β the deflection angle. The result w is then the vertical change in y-direction. The use of this function requires the chord to be aligned with the x-direction. The polynom order n is differing in both articles. Daynes internal flap structure requires a coefficient of 3, while the rubber flap by Madsen requires a coefficient of 2.

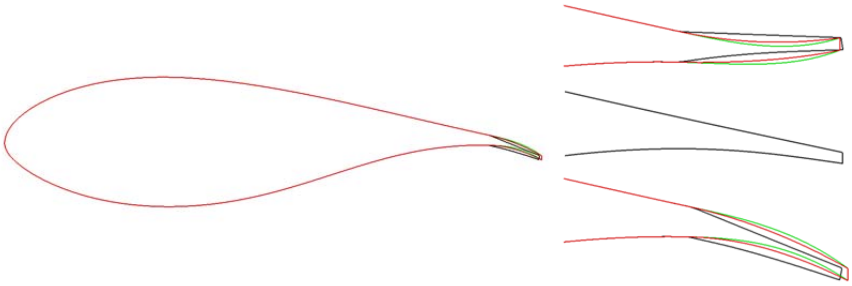

Figure 4: 10% flap with different polynom orders

In Figure 4, the different shapes of the flaps are shown for +/- 10° deflection angle. The black curve shows the rigid flap, the red the second order morphing flap and the green curve the third order morphing flap. As the rigid flap was derived by rotation it also shows a horizontal change of chord length, while the polynomial approach neglects this as the difference is only 0.45% of the total chord length. In the following Figure 5, a comparison of the surface generated through grid deformation and the DTU measurement by Madsen is shown. The 2nd order polynomial agrees very well with the measured surface.

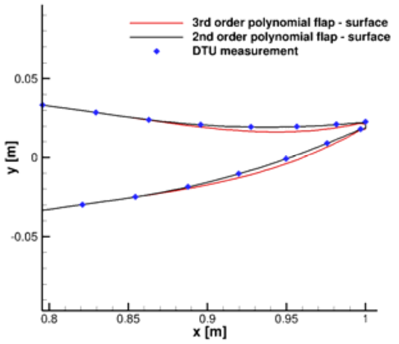

Figure 5: Morphing flap comparison to DTU measurement

The methodology for three dimensional simulations is shown in Figure 6. The flap part of the rotor blade is deformed like in the two dimensional case and connected to the remaining rotor blade with a transition area.

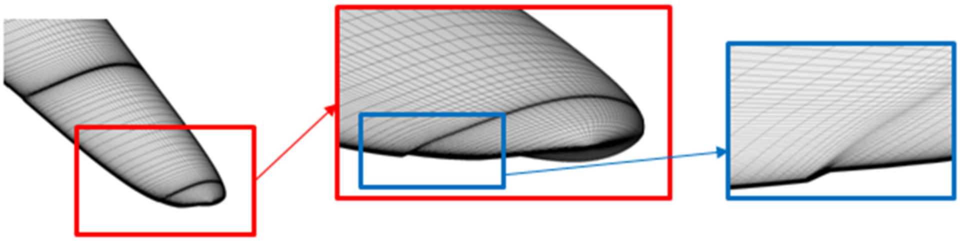

Figure 6: 3D trailing edge flap

This area is refined in the blade grid to achieve a smooth spanwise transition and capture spanwise gradients.

2.4 Validation studies in 2D

To analyse the flap model and the grid deformation algorithm extensive studies have been made in 2D and 3D environment. In 2D a comparison to measurements by Lambie [10] has been performed in [11] for steady deflection cases of combined leading and trailing edge flap. In the following the results of 2D simulations with a harmonic flap motion will be shown.

The background of this study is to compare the effectiveness of morphing and rigid flaps and to determine the needed time step to resolve unsteady aerodynamic effects like lift or drag hysteresis. As the results are supposed to be directly transferable to the three dimensional case, the profile at the radial of position of 75% blade span is chosen. In the three-dimensional reference case the flap extends from 70 to 80% blade span. At this location the FFA-w3-241 airfoil with a chord length of 3.3m is located. For the 2D simulations the flow conditions were extracted from a 3D simulation of the Innwind reference rotor at rated wind speed of 11.4 m/s to be as congruent to the 3D case as possible. The final setup parameters are shown in the following Table 5.

Parameter	Value
Reynolds number	15.40 Mio
Mach number	0.2
Angle of attack	6.4°

Table 5: 2D simulation setup

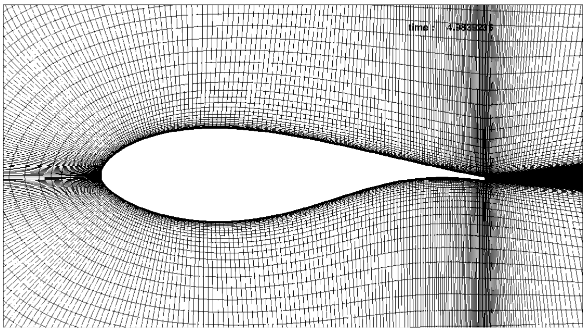

Figure 7: FFA-w3-241 airfoil grid

The deflection frequency is chosen to 6p at rated rotational speed, a very high frequency compared to the planned application. But as the background of this study is to validate the model with regard to unsteady effects a higher frequency is more meaningful. The chord extension of the flap was set to 10% like specified in the reference cases. The computational grid is of C-type and consists of approximately 60 000 cells. It was generated with an in-house script which has been extensively used for 2D cases. Most parameters were chosen based on experience. The airfoil is resolved with 320 nodes and the boundary layer with regard to a Y+ equal 1.

Figure 7 shows the final grid.

All simulations have been started with a steady state simulation with 0° flap angle to achieve a fully converged solution at first. From this initial point an unsteady restart was performed and the flap started to deflect. At first the results of the comparison between rigid, morphing flap of 2nd order and morphing flap 3rd order will be shown. The simulations have been performed with a time step corresponding to 100 points per convective time unit, which is in this case the chord length and leads to 3.5e-4 seconds.

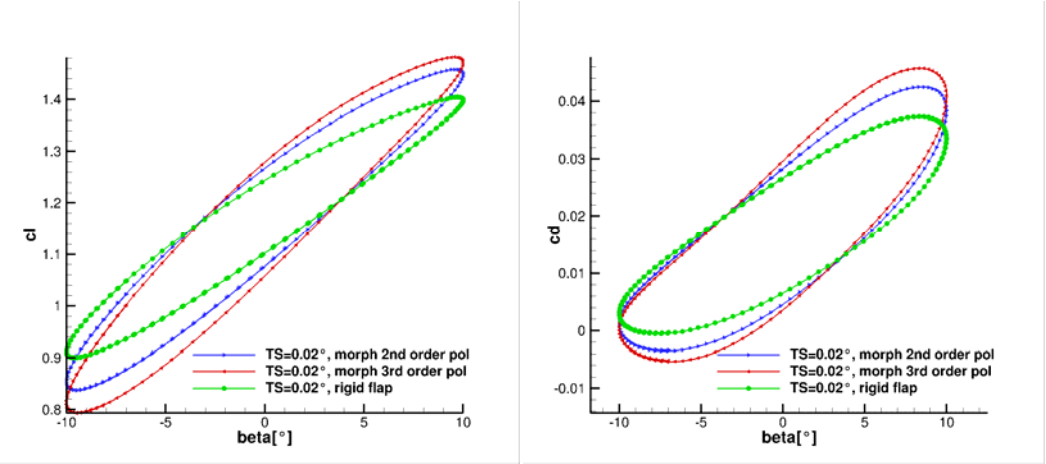

Figure 8: Comparison between rigid and morphing flap 2D

Figure 8 shows the hysteresis of lift and drag coefficient for all flap types. The 3rd order polynomial flap shows the highest lift and drag increase. The 2nd order polynomial shows slightly smaller maxima while the rigid flap, as a reference, has a greater offset to the other two curves. These results agree well with the theory by Kutta. As seen in Figure 4 the trailing edge angle is increasing with the polynomial order and therefore also the lift increase is higher. As conservative approach with regard to load variation reduction the 2nd polynomial was chosen for the final simulations.

Three different time steps have been investigated to determine the needed time step for a full rotor computation:

- 8.7e-3 s (corresponding 0.5° azimuth at rated rotational speed)
- 1.7e-2 s (corresponding 1° azimuth at rated rotational speed)
- 3.5e-2 s (corresponding 2° azimuth at rated rotational speed)

As reference the very small step of 3.5e-4 s (0.02° azimuth) was used. In a full rotor computation, this time would correspond to approximately 0.02° azimuth step at rated wind speed. For 2D simulations this time step is generally possible, but for 3D cases with a full rotor the computational time is far too high. In 3D cases, typically, a time step of 2° is chosen and has been used in many studies at the IAG. However, to resolve unsteady flap effects this time step is expected to be insufficient.

In the following section, the results of the simulations with 2nd polynomial flap will be shown. Figure 9 shows a time series of the flap angle β, lift coefficient cl and drag coefficient cd on the left. On the right the hysteresis of cl can be seen. The influence of the different time steps is very distinct in all diagrams. The greater time step corresponding to 2° azimuth cannot resolve the effects correctly in magnitude. In addition there is a temporal offset with regard to the smaller time steps. The time steps corresponding to 0.02° and 0.5° show a good agreement in nearly all points in time, while the time step corresponding to 1° has a little offset, which is still within an acceptable range.

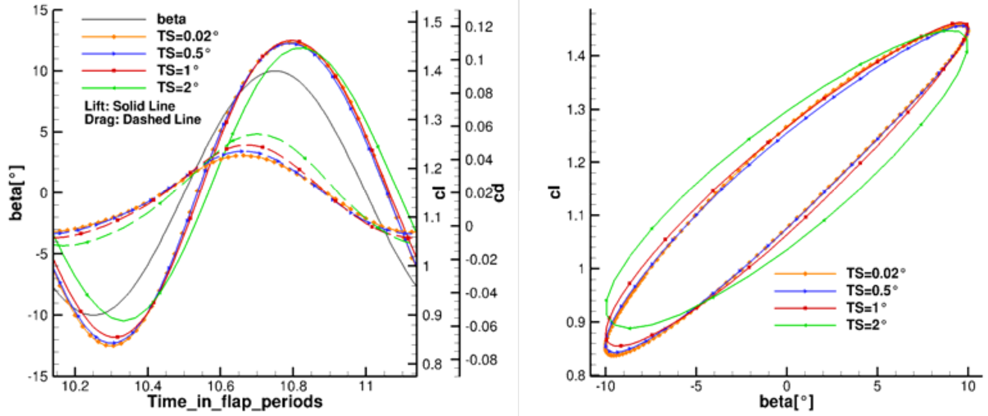

Figure 9: Morphing flap based on 2nd order polynomial

In general, it can be observed that the lift and drag curves show slight phase shifts with regard to the flap signal. Drag is running ahead and lift lags the flap phase. This phenomenon can be explained with Theodorsen's theory of unsteady airfoil aerodynamics [12]. Although Theodorsen regards a harmonically pitching airfoil, the results can be applied on an airfoil with flap as the effect is the same, a harmonically changing bounded circulation. As explained by Leishman in [13], the lift coefficient in unsteady motion is divided into two components, a circulatory part which is driven by the bound circulation and a non-circulatory part, also known as apparent mass effect. Leishman states that for reduced frequencies of less than 0.2, as regarded here, the circular forces are dominant and lead to a lag of the lift coefficient. The phenomenon can be well explained with vorticities which are shed into the wake due to the change of bound circulation on the airfoil. These vortices themselves induce velocities at the airfoil opposing the effect of lift change.

2.5 Validation studies of the flap model in 3D

The bases of the three-dimensional studies are the results of the AVATAR Deliverable 2.3 [14]. Within this task simulations of the power curve of the DTU 10 MW turbine and the AVATAR rotor have been conducted. The main objective was to perform a code-to-code validation between all partners as for now and in the foreseeable future no measurements will be available for a 10 MW turbine. In Figure 10 the results of the comparison for the DTU 10 MW turbine are shown. FLOWer (USTUTT) is in good agreement with the CFD codes Ellypsis3D (DTU-ELL) and MapFLOW (NTUA) in the under-rated regime, while HMB2 used by CENER and ULIV predicts slightly higher power and thrust. The vortex code by DTU (DTU-MIRAS) generally tends to underestimate thrust. In the over-rated cases larger discrepancies can be observed with FLOWer and Ellypsis3D being in the mid of all curves.

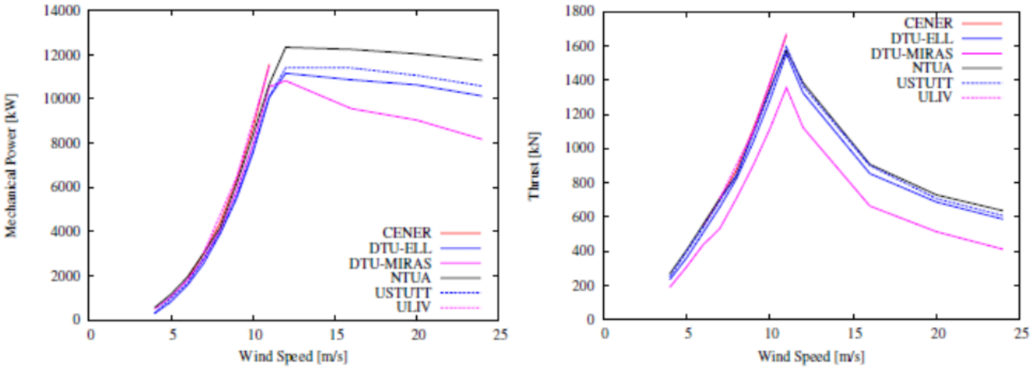

Figure 10: Simulations of the power curve [14]

Across the board the prediction of thrust is more congruent than power as this force is more pressure driven. As conclusion it can be stated that the spread between the results was larger as expected, but nevertheless it gives an impression of accuracy.

The three-dimensional simulation of trailing edge flaps was started with a grid independency study especially regarding the spanwise and chordwise resolution in the area where the flap will be located. Although this study was performed for a rigid deflection and a slightly different spanwise flap location the results are transferable to the reference cases regarded in this task.

The investigation was performed with a pure rotor configuration in 120° model with periodic boundary conditions. All grids apart from the blade grid are identical to those used in [14]. Also the numerical setup didn't require any changes apart from the application of the grid deformation module.

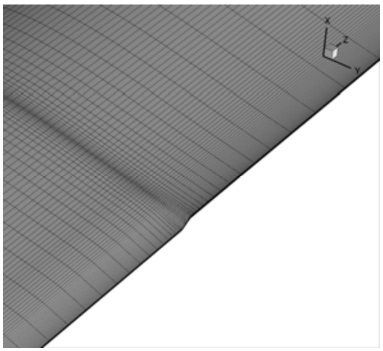
Figure 11: Spanwise refinement

	Coarse	Medium	Fine	Baseline
Blade grid cells [million cells]	7.52	8.75	10.53	6.84
Chordwise nodes	221	233	253	221
Spanwise nodes	153	181	221	133
Spanwise spacing at flap transition [m]	0.1	0.05	0.01	-

Table 6: Grid resolution

In Table 6 the different investigated resolutions are shown with the baseline grid representing the mesh used in [14]. The grids include three spanwise refinements as shown in Figure 11 at the radial stations of 57.8m, 62.8m and 67.8m. Hence two flaps can be deflected separately. An increase of approximately 1.3 million cells per flap for medium resolutions can be determined. For this study only the inner flap was deflected with +/- 10°.

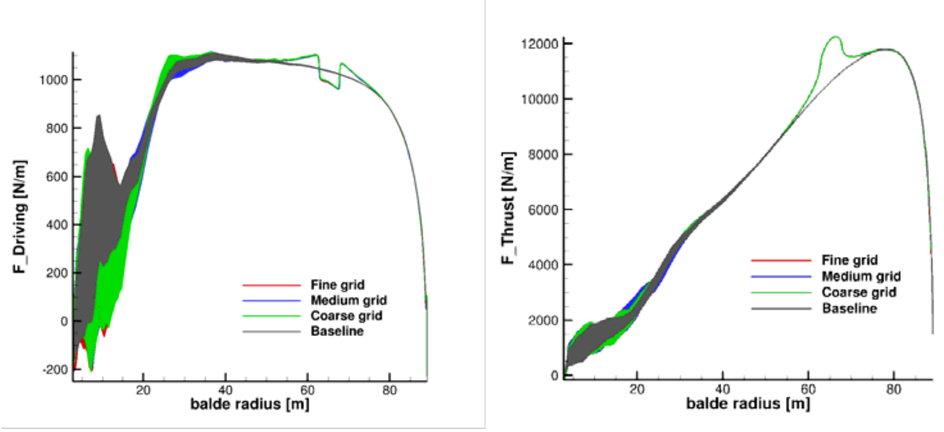

Figure 12: Flap grid convergence β=10°

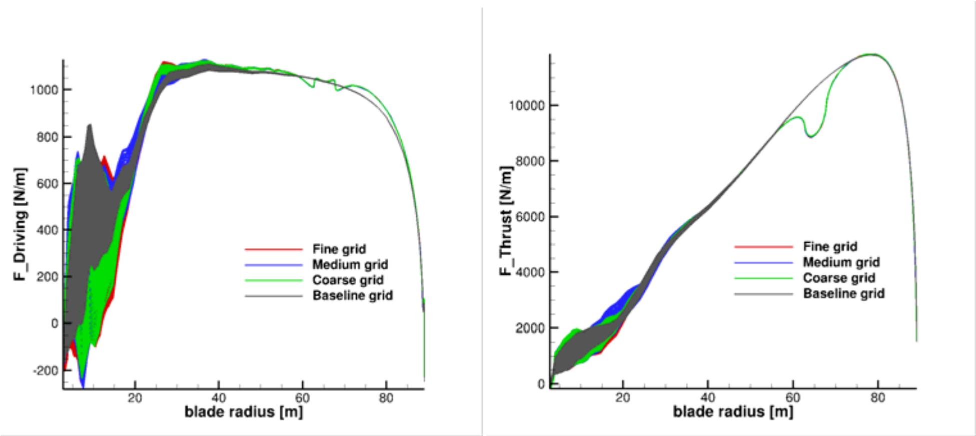

Figure 13: Flap grid convergence β=-10°

In Figure 12 and Figure 13 the unsteady driving and thrust force over the blade span is plotted for one revolution. At the spanwise location where the flap is deflected only very small differences between the different resolutions can be observed and therefore the results can be regarded as grid independent in this area. Remarkable is also that no unsteady effects are visible at the flap location for a static deflection.

At the blade root larger discrepancies occur due to the transient flow separation at the cylindrical cross sections located there. Especially in the driving forces, the effect is very strong up to a radius of approximately 20m. As these blade stations have a small lever arm, the effect is less dominant in torque and power. However, it has to be stated that large-scaled blade root separation is occurring and that the physical correctness cannot be assessed without a detailed investigation or even experimental measurements. Separation is strongly dependant on grid resolution, turbulence model and the chosen time step. But as the focus point of this task is on the application of trailing edge flaps on the outer part of the blade, these effects are not regarded in detail.

An intriguing result of the study is that a deflection of 10° leads obviously to an increase in thrust but to a decrease in the driving force. The opposite behaviour can be observed for a deflection of minus 10°. Therefore an evaluation of the angle of attack and aerodynamic coefficients was performed at distinct radial stations and the results are shown in Figure 14. An increase or decrease of lift and drag due to the deflection can be seen at the flap location. For the positive deflection lift increases by a factor of 1.12 and drag by a factor of 2. This leads to a much higher increase of drag and therefore a decrease of the driving force.

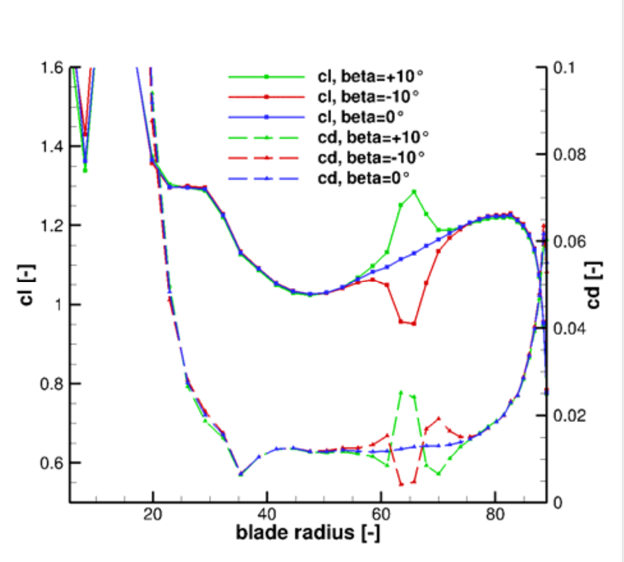

Figure 14: Aerodynamic coefficients

The next step to validate the setup was to conduct unsteady simulations with harmonic flap oscillations to examine the time step based on the results from 2D. The 120 degree model with the pure rotor was also chosen for this investigation. The final flap configuration was available for this study and thus the flap extends from 70 to 80 % radius. The chordwise extension with 10% did not change. Like in the two-dimensional case the regarded flapping frequency is 6p. All computations were started from a converged solution with a steady deflection of 10°. The results were obtained for a rigid flap. Again the three different time steps from the 2D investigation are examined: 0.05°, 1° and 2° azimuth.

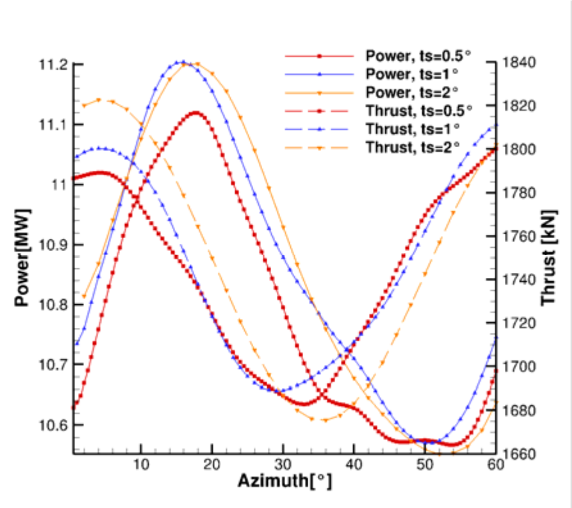

Figure 15: Time step study - Integral power and thrust

Figure 15 shows a time series of the integral power and loads over one flapping period. The deflection is a cosine function starting from 10° deflection. A large spread can be seen in power and thrust, although the impact of the flap movement is present in all curves. Power varies from approximately 10.55 to 11.2 MW and thrust from 1680 to 1820 kN. One major part of the differences results from the blade root separation which is in different states for all simulations due to the different time steps. A better conclusion can be drawn by regarding the sectional forces at the mid profile of the flap section which are shown in Figure 16.

In this picture the sectional driving and thrust force are shown over one period of flap deflection. In thrust a fair agreement between all different time steps is observed. Like in the two-dimensional case a time lag with regard to the flap deflection is present and increasing with the time step. Again the 0.05° and 1° time step show a better agreement with regard to the 2° step. The driving force shows larger discrepancies between the different time steps. In general a delay of the maximum and minimum peak with regard to the deflection can be seen. 2° shows a nearly sinusoidal behaviour. 0.5° and 1° resolve more unsteady effects and show a flattening of the force when the flap is moved downwards.

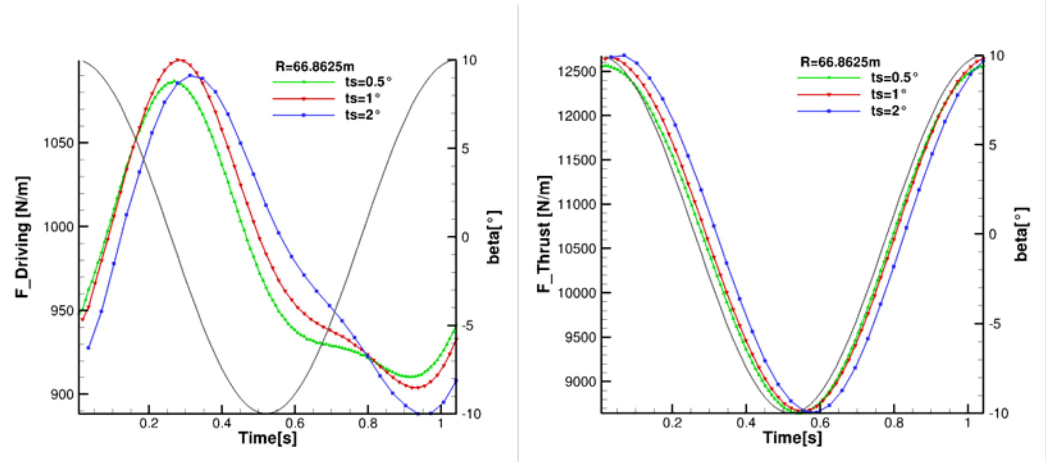

Figure 16: Time step study - sectional forces at 75% blade cut

A further reduction of the time step will probably give more detailed knowledge about the influence of temporal resolution on the result, but was not possible within this study. For the simulations with the full turbine model a time step of 1° was selected as trade-off between simulation accuracy and computation time and power. Simulations in the 120° degree model were performed with a time step of 0.05° for high flapping frequencies like 6p and 1° for the frequencies 1p and 3p. Also with regard to trailing edge flaps it can be noticed that the main focus point is a reduction of thrust variations.

2.6 Simulation of reference cases

The following chapter presents the reference cases in detail including integral power and loads, sectional forces over blade span and time, local line forces at 75% blade cut and aerodynamic coefficients. At first the results of the pure rotor simulations are shown followed by the discussion afterwards.

Pure rotor simulation with harmonic 1p flap oscillation at 11.4 m/s

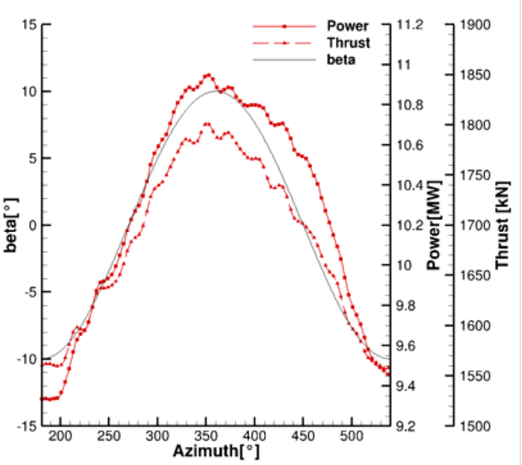

Figure 17: Integral power and thrust - pure rotor 1p 11.4 m/s

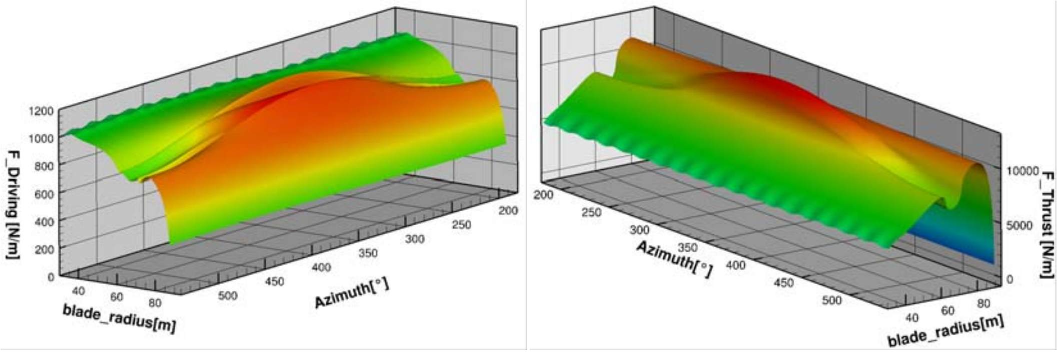

Figure 18: Sectional forces time series - pure rotor 1p 11.4 m/s

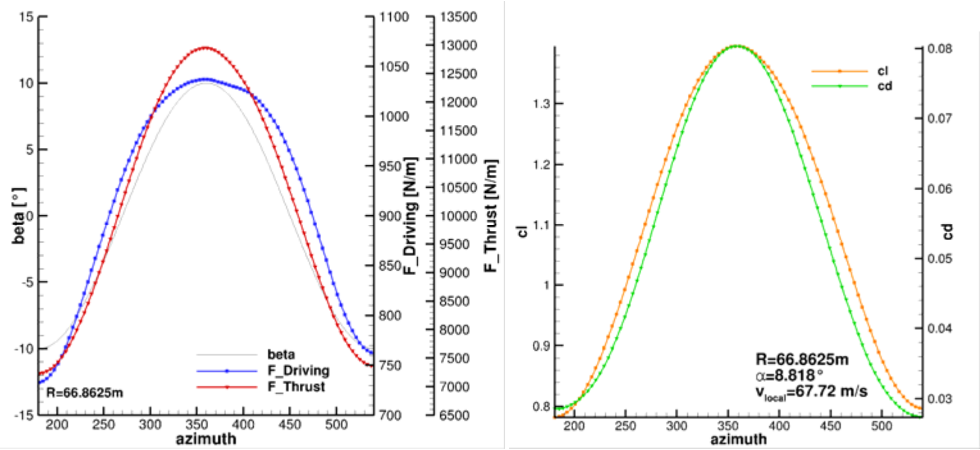

Figure 19: 75% blade cut - pure rotor 1p 11.4 m/s

Pure rotor simulation with harmonic 3p flap oscillation at 11.4 m/s

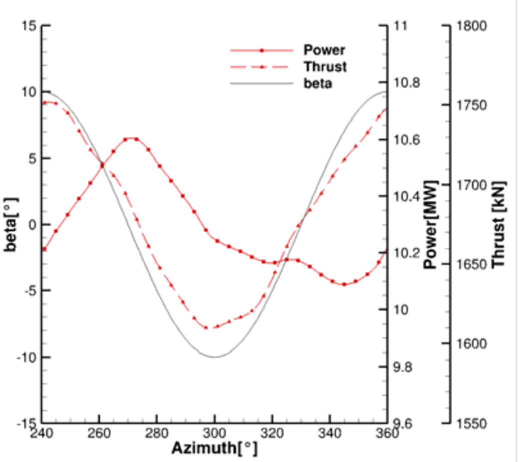

Figure 20: Integral power and thrust - pure rotor 3p 11.4 m/s

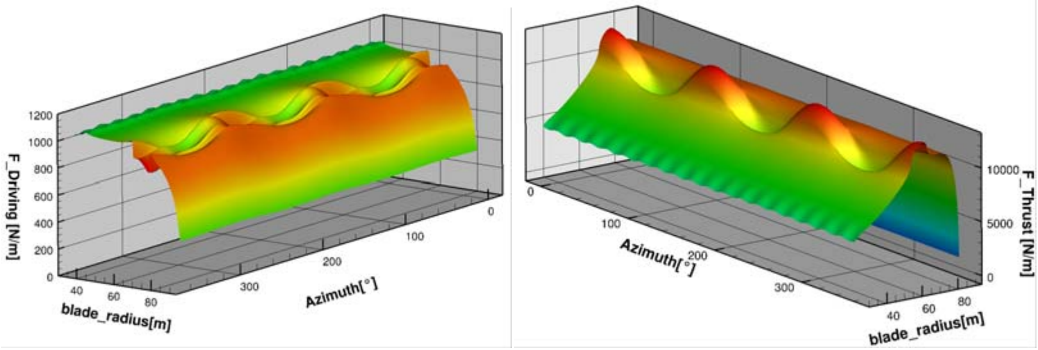

Figure 21: Sectional forces time series - pure rotor 3p 11.4 m/s

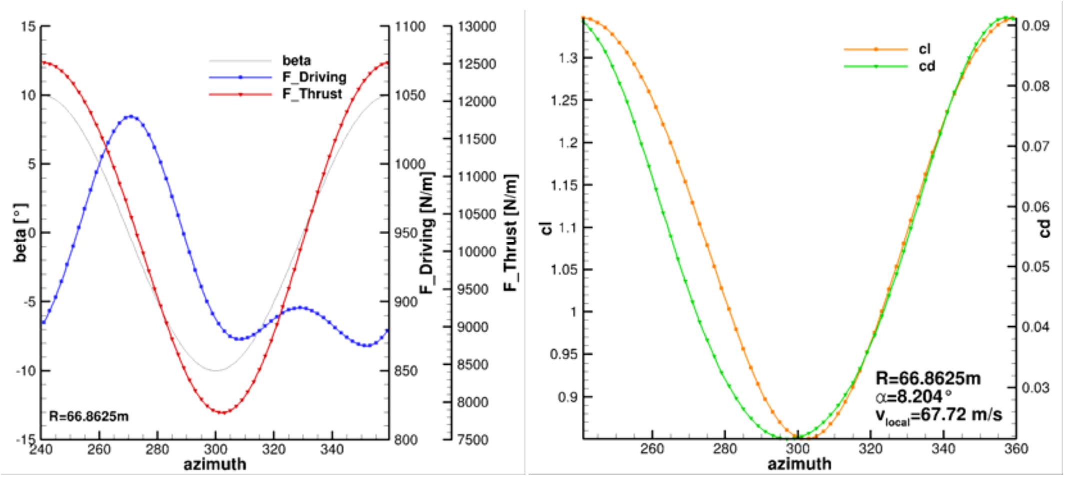

Figure 22: 75% blade cut - pure rotor 3p 11.4 m/s

Pure rotor simulation with harmonic 6p flap oscillation at 11.4 m/s

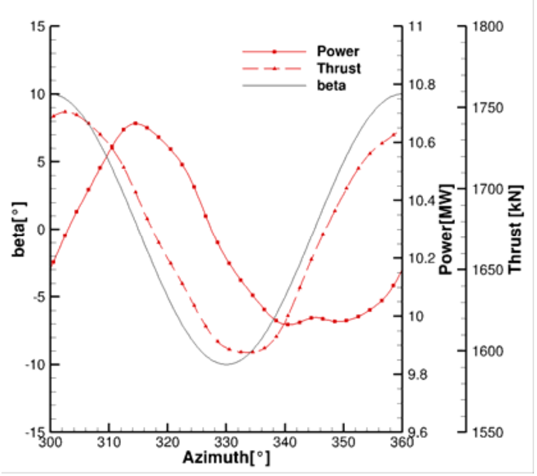

Figure 23: Integral power and thrust - pure rotor 6p 11.4 m/s

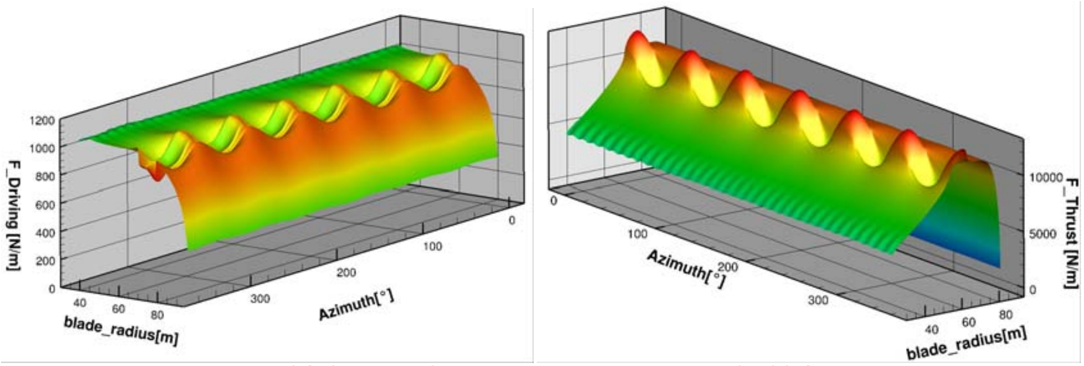

Figure 24: Sectional forces time series - pure rotor 6p 11.4 m/s

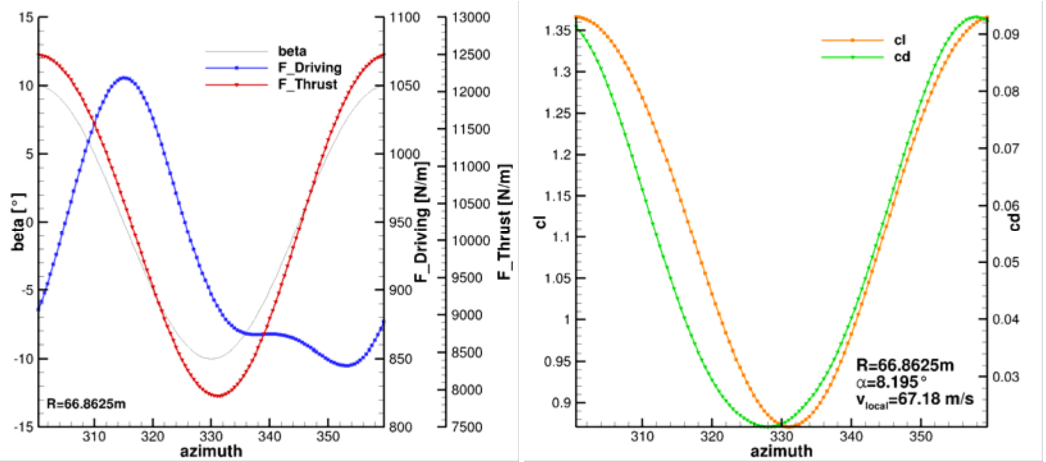

Figure 25: 75% blade cut - pure rotor 6p 11.4 m/s

Pure rotor simulation with harmonic 6p flap oscillation at 19 m/s

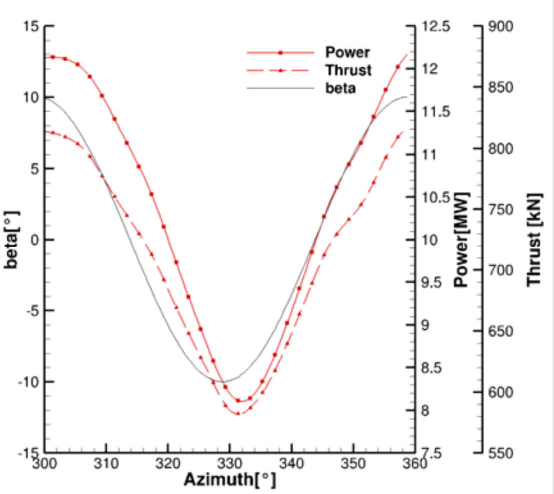

Figure 26: Integral power and thrust - pure rotor 6p 19 m/s

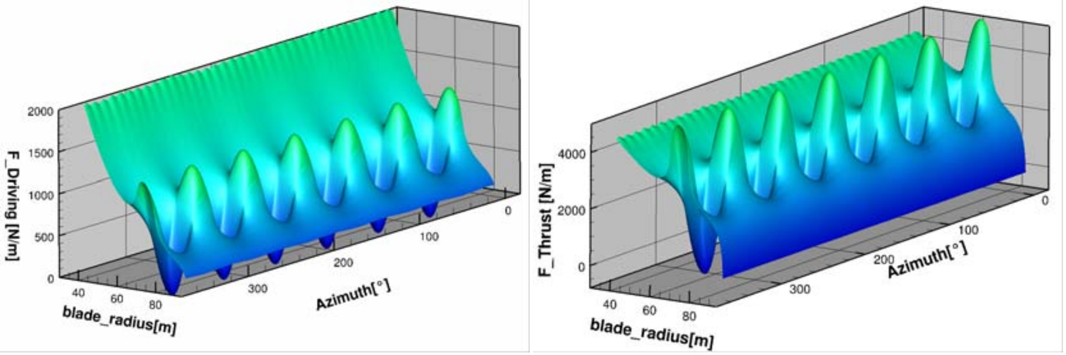

Figure 27: Sectional forces time series - pure rotor 6p 19 m/s

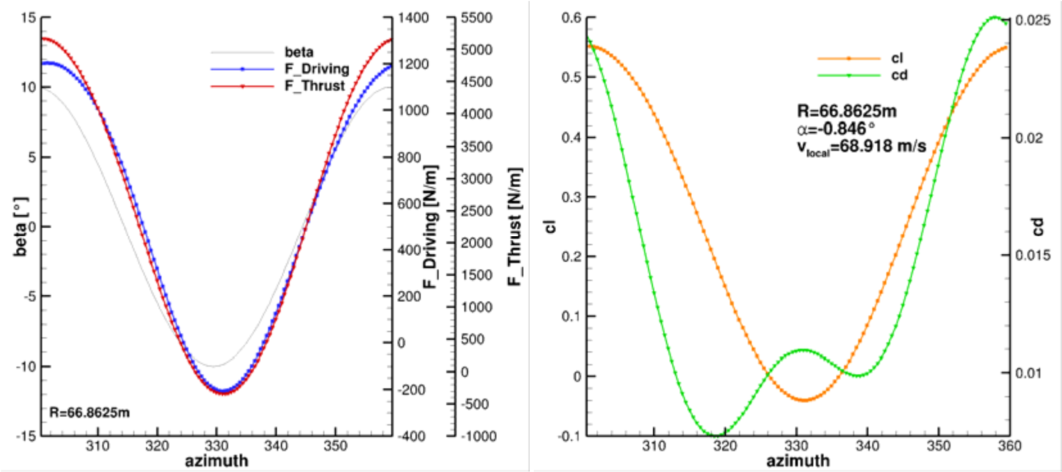

Figure 28: 75% blade cut - pure rotor 6p 19 m/s

Discussion

The first reference case is regarding the 1p frequency at rated wind speed. This leads to reduced frequency of approximately 0.024 at the regarded blade cut at 75% radius, a value being well below the limit 0.05 for quasi-steady conditions. No unsteady effects like hysteresis are expected and can be seen in the results shown in Figure 17, Figure 18 and Figure 19. Integral power and thrust are overlapped by the fluctuations due to the root separation. The sectional examinations show smooth curves for driving and thrust force and also the analysis of the aerodynamic coefficients is plausible with no phase shift between lift and drag. Noteworthy is the flattening of the driving force peak due to the high drag.

In the second reference case an interesting phenomenon can be seen in power and driving force, printed in Figure 20, Figure 21 and Figure 22. The force shows a second small peak at approximately 330° azimuth which corresponds to a phase of 0.75 flap period. This peak is a result of the time shift between lift and drag that can be observed at this frequency.

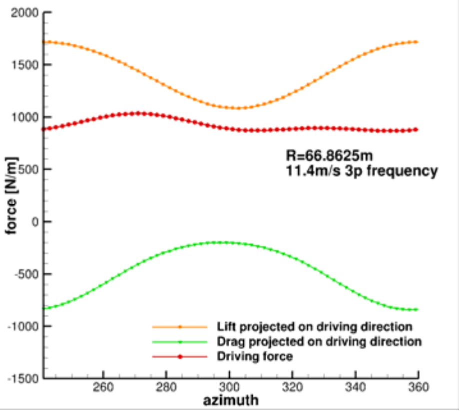

Figure 29: 11.4 m/s 3p - Driving force components

As shown in Figure 29, drag has a very strong influence at the rated condition due to the superposition of forces. In the diagram y-projections (driving direction) of lift and drag are shown and summed up to the final driving force. With a reduced frequency of 0.072 the unsteady phenomena that can be seen are reasonable and compare well to the effects seen in 2D.

The highest examined frequency is the 6p case with period length 60° azimuth or 1.04 seconds. This frequency corresponds to a reduction of the tower shadow effect as in previous studies [15] with simulations of the full turbine it was found that the power and thrust decrease is very distinct in a period of 30° azimuth. Figure 23, Figure 24 and Figure 25 show the results for this case. The time series for integral power and thrust as well as sectional forces demonstrate reasonable curve progressions. The results for lift and drag are also in a good agreement to theory as the time lag of lift did not increase due to the higher frequency like it is explained in [13].

In the last case an over-rated condition at 19 m/s is regarded. At this operating point the blade is already highly pitched with 16.432° and this is very apparent in the results printed in Figure 26, Figure 27 and Figure 28. In the sectional forces it can be observed that the power is produced more in-board of the blade span compared to the rated case. The high pitch angle also leads to higher influence of the local lift force on the driving force and therefore power is now much more dependent on the flap angle. Due to the high pitch angle the local angle of attack on the blade is quite low with approximately -0.85°. This leads to a negative lift in the course of the flap hysteresis as seen in Figure 28. The negative lift production is connected to a temporary increase of drag.

Generally the influence of the flap is highly elevated in the over-rated case compared to the rated cases.

Table 7 shows a line-up of the variations in integral power and thrust. In the rated cases the low frequency shows the highest influence due to the quasi-steady conditions. The 3p and 6p rated case show a similar influence on thrust while the driving is highly influenced by the phase of lift and drag to each other.

	11.4 m/s 1p		11.4 m/s 3p		11.4 m/s 6p		19 m/s 6p	
	Min	max	min	max	min	max	min	max
Power [MW]	9.33	10.95	10.05	10.62	9.86	10.72	8.11	12.17
Power variation	8%		2.7%		4.2%		20%	
Thrust [kN]	1557	1802	1595	1767	1590	1757	582	818
Thrust variation	7.3 %		5%		5 %		17%	

Table 7: Comparison of power and thrust variation for the harmonic flap cases

Figure 30 shows the minor influence of three-dimensional effects at the flap location due to the deflection. Plots of the pressure coefficient normalised with blade tip rotational velocity are shown in addition to surface stream traces. Only in the 1p case a spanwise distraction is visible at the beginning and ending of the flap. In all plots the thicker black line represents the 75% blade cut.

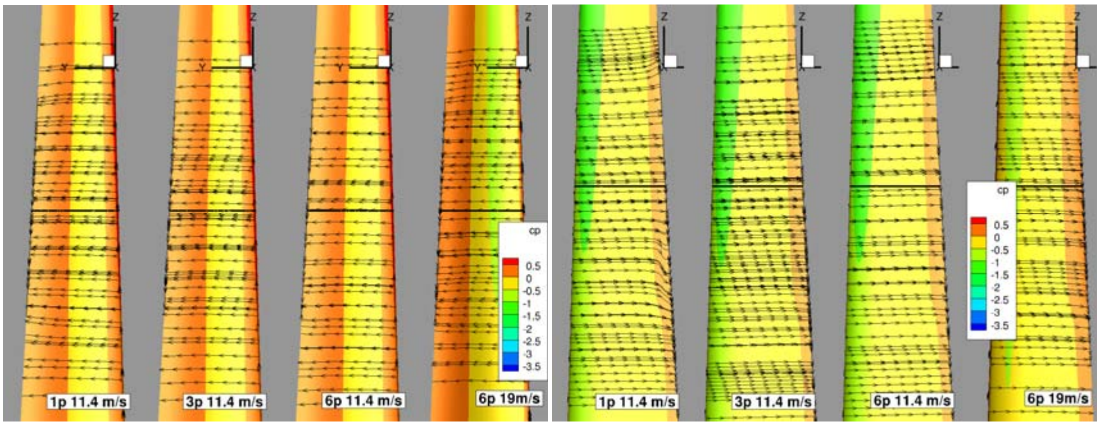

Figure 30: Comparison of surface stream traces at $0.66T_{flap}$– pressure side (left) and suction side (right)

Full turbine with TU Delft flap signal at 19 m/s shear profile

The last reference case considers a full turbine configuration including tower and nacelle. As inflow a steady atmospheric boundary layer was chosen based on the power law. The flap signal was kindly provided by TU Delft.

The computational meshes can be seen in Figure 31. The grids of tower in combination with nacelle, spinner and blade are embedded into a rectangular background mesh. This background grid uses the principle of hanging grid nodes, which is available in FLOWer to reduce the amount of grid cells. Convergence studies showed that a vortex grid at the blade tips significantly increases the quality of the simulation and it was therefore introduced into the simulations. The background grid extends in x- (flow-) direction from -540m to 996m, in y-direction from -608m t0 608m and in z-direction from 0m to 768m. Cell sizes were set to 1m^3 around the turbine and 4m^3 in the direct inflow area close to the ground where the gradient due to the shear profile is still large. The turbine tower is located at the origin of the background grid. Grid sizes are shown in Table 8.

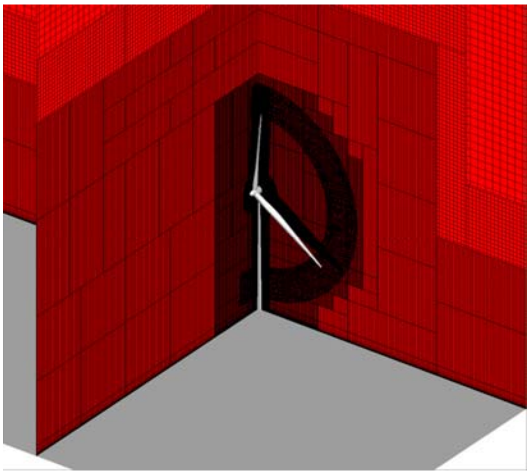

Figure 31: Computational grid - Full model

Grid	Amount of cells
Background	23.3 Mio
Tower and Nacelle	7.4 Mio
Spinner	4.95 Mio
Blade per blade	7.5 Mio
Vortex grid	2.16 Mio
Total	60 Mio

Table 8: Grid sizes

Ten revolutions have been simulated with a time step of 2° azimuth before analyzing the computation. As mentioned above in unsteady simulations the flow field needs to develop and be propagated. After this time period power and thrust have converged to constant average value. The final evaluation period was chosen to be the 11th to 12th revolution. For the evaluation period the time step was reduced to 1° azimuth.

Two separate cases were simulated: a reference case without flaps and a case with flap deflection based on the signal provided by TU Delft.

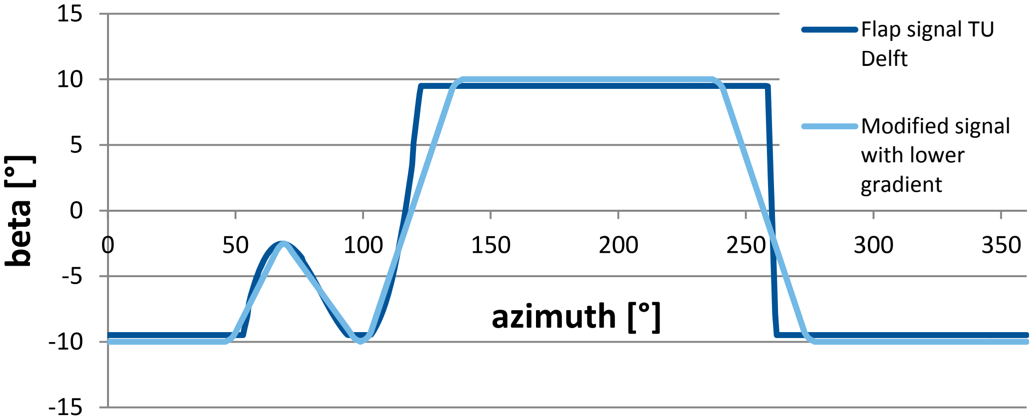

Figure 32: Flap signal TU Delft

The provided flap signal was covering a 10 minute time period and was simulated with blade element methods. To ensure a steady controller state the last two revolutions have been extracted and analysed. As it can be seen in Figure 32, the original signal had to be modified to satisfy the needs of a CFD simulation. The original signal shows very steep slopes at approximately 120° and 260° azimuth that cannot be captured correctly with the proposed time step. Therefore a slope limiter was set to 0.58° flap deflection per step. Also, the curvature was adjusted to achieve smooth transitions.

Figure 33 shows the results of integral power and thrust with and without flap deflection for all blades. In the plot azimuth axis an angle of 0° corresponds to the start of the 11th revolution of the simulation. Results starting from approximately 120° are shown here. Generally a reduction of the magnitude of power and load is apparent in the plot. The power level is reduced by approximately 0.5 MW and the thrust level by approximately 25 kN. No reduction of the total load variation can be observed.

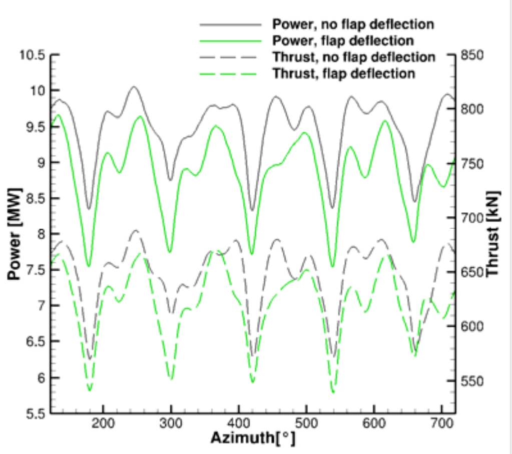

Figure 33: Integral power and thrust for all blades - 19 m/s shear profile

In Figure 34 the share of each blade of the turbine loads is plotted. These separated values show a reduction of the variations per blade. For blade 3 as example power varies from 0.53 MW in front of the tower to 4.7 MW at 0°azimuth position and thrust from 71 to 292 kN. The use of flaps reduces these fluctuations to a range from 1.1 to 4 MW in power and 110 to 257 kN in thrust.
Nevertheless, the turbine power output was significantly reduced due to the negative deflection when the blade is operating in the range from 240°to 90° azimuth in free stream inflow. This decrease could not be compensated by the increase of power on the lower side of the rotor disk from 90° to 240°. An improvement of the behaviour could probably be achieved by generally lowering the pitch angle of the blade or especially in the free stream inflow range from 240° to 90° azimuth for individual pitch control.

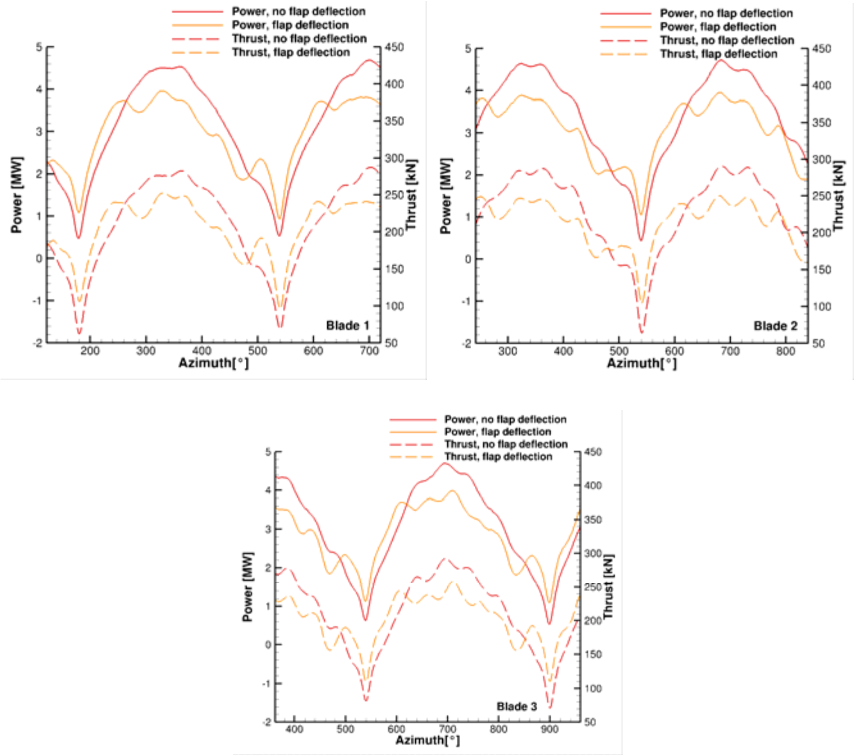

Figure 34: Blade power and thrust - 19 m/s shear profile

The resulting out-of-plane blade root moment is plotted in Figure 35 for blade 1. It shows less fluctuations compared to the blade thrust forces shown above due to the minor influence of the blade root separation on the moment.

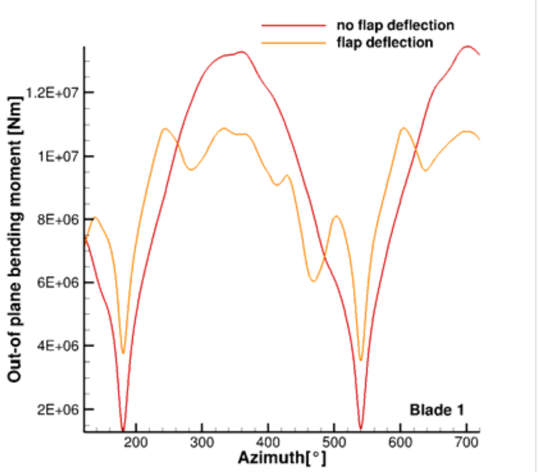

Figure 35: Blade 1 out-of-plane bending moment - 19 m/s shear profile

Figure 36 and Figure 37 show the distribution of sectional forces over azimuth and blade span for the case with and without flaps. The influence of the flaps is very distinct in both forces, driving and thrust. Without flaps very smooth distributions can be seen with a high influence of the tower shadow. The impact of shear is apparent especially in thrust, in which a steady increase and decrease can be seen dependant on azimuth and blade radius. Flaps introduce severe variations the spanwise distributions. Especially when the blade is approaching or moving away from the tower high thrust peaks can be seen, which introduce high forces on the blade and might cause dynamic vibrations.

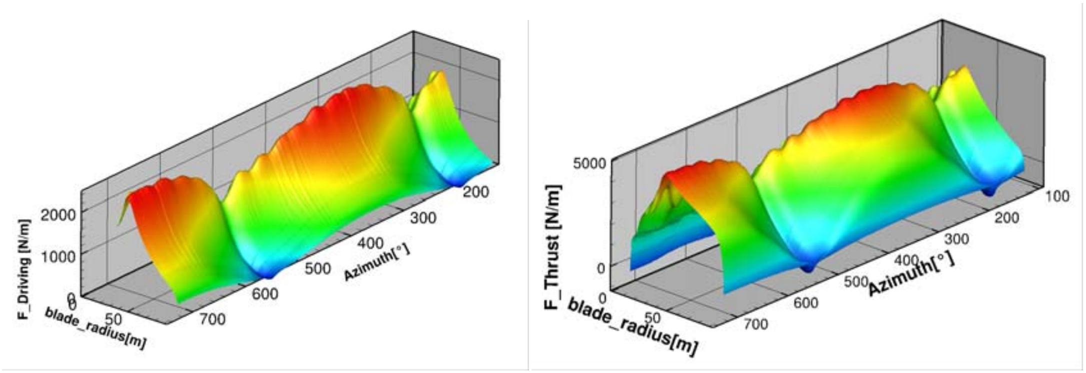

Figure 36: Sectional forcing blade 1 - 19 m/s shear profile

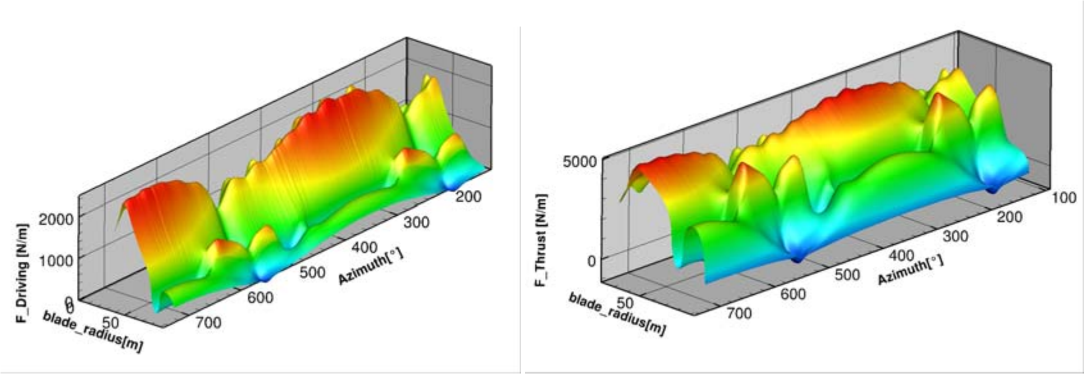

Figure 37: Sectional forcing with flaps blade 1- 19 m/s shear profile

Like in the previous cases the course of the forces at the 75% blade cut was extracted to be able to quantify the effect more adequately. Contrary to the previous cases with harmonic flap deflection the plots show now sectional forces and not line forces (compare page 12). In Figure 38 the results with and without flap deflection are plotted. Without flaps a smooth curve can be seen with a high decrease in front of the tower in both driving and thrust force. The flap deflection opposes the effect very effectively and shifts the curve to higher level. Nevertheless the effect can still be seen. Generally the forces follow the deflection curve well with the expected time lag, which was observed in the harmonic cases.

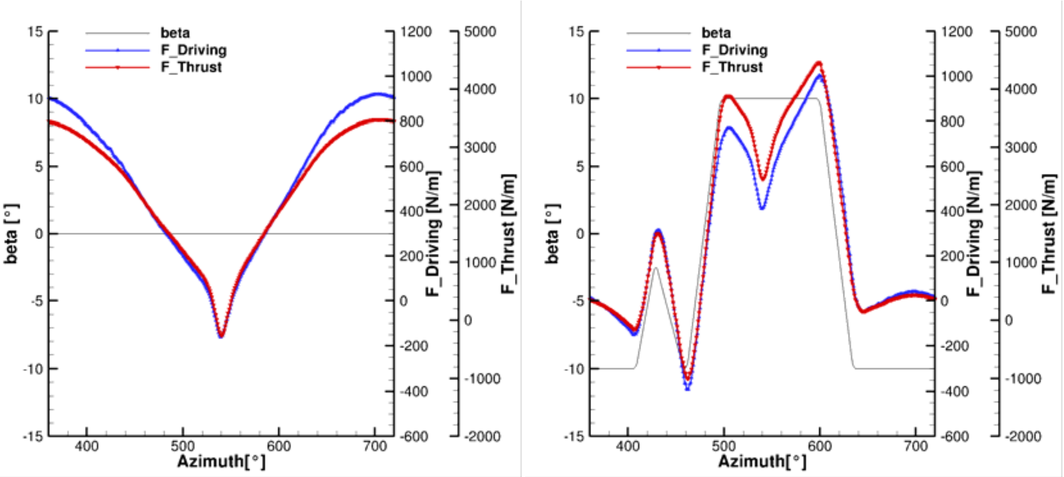

Figure 38: Sectional forces blade 1 75% blade cut without flaps (left) and with flaps (right) - 19 m/s shear profile

2.7 Modifications of the flap signal

Modification of the flap signal as function of azimuth for 19 m/s steady ABL case

Based on the results from the last reference case, the ambition was at first to see the influences of the flap by comparing two signals with each other.

With regard to the signal provided by TU Delft two major changes have been made. The first one concerns the oscillation from approximately 50° to 100° azimuth, where the flap starts to the move downwards but returns to the starting position. No distinct source that could cause this behaviour could be observed in the CFD results and therefore the rise was removed in the modified signal. The second adjustment was made at the transition from 10° to -10° deflection. At this state a high peak in the thrust and driving force was observed caused by a late decrease of the flap angle. This issue might be caused by the time lag of lift observed in the previous cases. To alleviate the load fluctuation at the local blade section the flap movement was started earlier as shown in Figure 39.

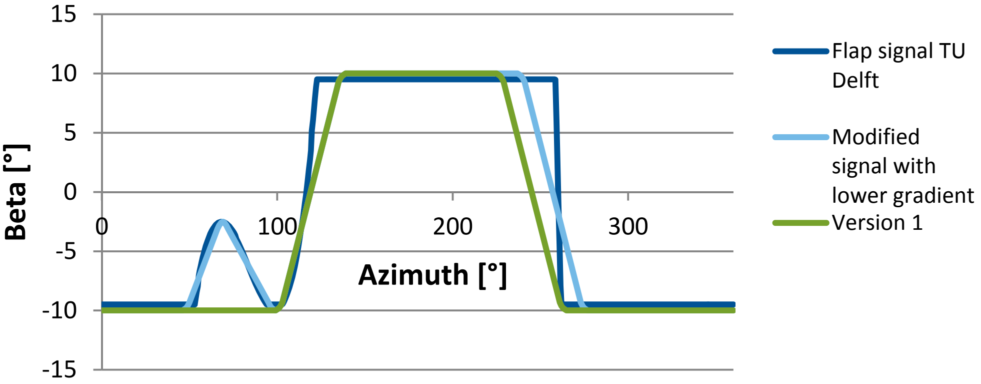

Figure 39: Modified flap signal as function of azimuth

In Figure 40 results obtained with the modified signal are shown for blade 1. The modified signal is marked as version 1. The changes are clearly visible in the curves and the comparison gives a further insight of how the flap signal was generated by the TU Delft controller. Starting from an azimuth angle of 410° the influence of the first modification leads to an earlier decrease of the blade root bending moment. The controller was opposing this effect by moving the flap downwards. In the diagram the curves reunite at approximately 480° azimuth in a minimum at very low loads, not showing any reduce of the variation. It can be presumed that the controller was reducing this decrease in the blade element method, in which it was differently developed. In CFD the effect emerges in another way and lasts longer. Therefore it could not be compensated. An improvement would be to start the deflection already at 410° but without the returning to -10°. The second modification starting from 220° azimuth angle reduced the maxima in loads, which can be ascribed to the time lag between the deflection and loads. The 75 % blade extraction is shown in Figure 41.

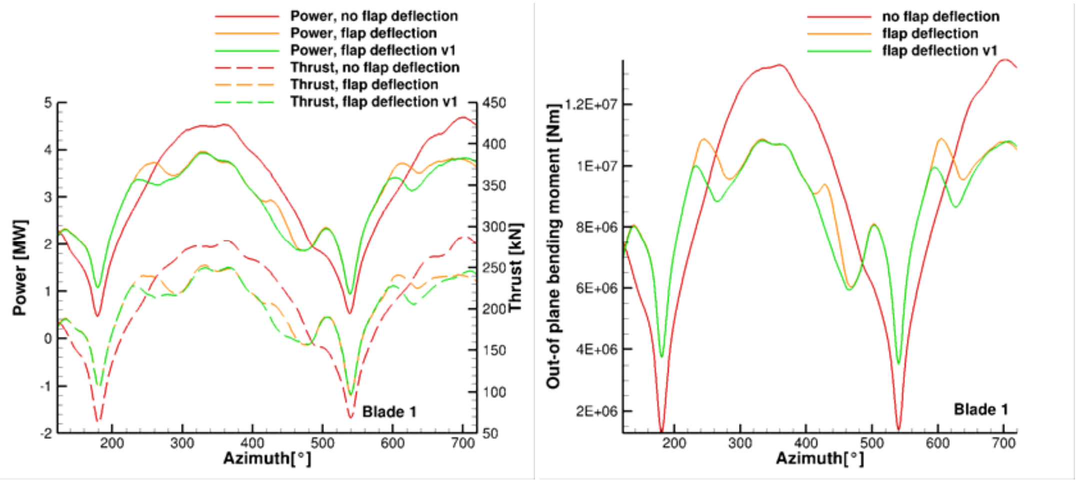

Figure 40: Blade 1 power/thrust(left) and out-of-plane bending moment(right) - 19 m/s shear profile, modified flap signal

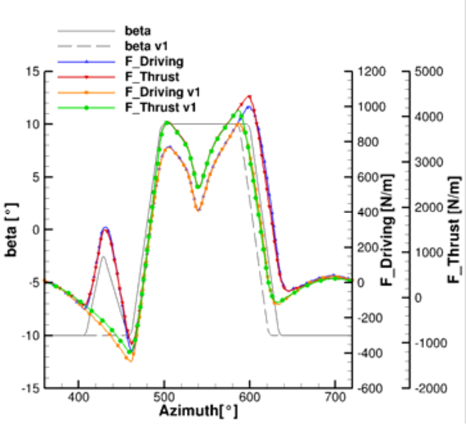

Figure 41: Sectional forces blade 1 75% blade cut - 19 m/s shear profile, modified flap signal

2.8 Conclusions/Outlook

Within the Innwind project extensive studies of the influence of trailing edge flaps on the flow and loads around wind turbines have been performed at the IAG. A morphing flap shape model has been implemented into the CFD code FLOWer to simulate the influence of these devices. 2D and 3D computations have been performed to validate the setup with regard to grid independency and temporal resolution.

The 2D simulations were focussed on identifying transient effects caused by harmonic flap oscillation. Different types of flap shapes have been regarded: a rigid flap, a morphing flap defined by a second order polynomial and a morphing flap defined by a third order polynomial. The third order flap showed the highest lift and drag variation due to the highest outflow angle at the trailing edge. Generally, a time lag of lift with regard to the flap signal could by observed which is caused by the vorticity shed into the wake due to the change of bound circulation. For the 3D simulations the second order polynomial shape was chosen as a conservative approach with regard to reduction of load variations.

The pure rotor was simulated in a 120° model with periodic boundary conditions. Like in the 2D case, the flap was harmonically oscillated with three different frequencies (1p, 3p and 6p) for the rated case of 11.4 m/s wind speed and one frequency (6p) for the over-rated case of 19m/s. The 1p frequency showed no hysteresis effect as expected by a reduced frequency of 0.024. For the 3p and 6p frequency, similar observations like in the 2D cases were made with a phase shift between flap signal and lift response. In the rated case, the phase shift has a very high influence on the driving force due to the orientation of lift and drag vector to driving force and thrust direction in this case. At 19 m/s wind speed, the influence of the phase shift is not that dominant. The simulations with the full turbine model showed the impact of the flap on turbine loads in a realistic situation at 19 m/s wind speed. With the flap signal provided by TU Delft the load variation in the blade root bending moment could be reduced from approximately 80% around the mean value of 6.1e6Nm to approximately 50% around the mean value of 7.2e6Nm with regard to the hub centre and for the given case. On the other side very large gradients appear in the sectional loading of the blade which might cause structural problems.

2.9 References

[1] K. Meister, E. Krämer and T. Lutz, “Development of a process chain for detailed wake simulation of horizontal axis wind turbines,” in *EUROMECH*, Madrid, 2009.

[2] N. Kroll and J. Fassbender, MEGAFLOW – Numerical Flow Simulation for Aircraft Design, Berlin/Heidelberg/New York: Springer Verlag, 2002.

[3] F. Menter, “Two-Equation Eddy-Viscosity Turbulence Models for Engineering Applications,” *AIAA Journal,* vol. 32, pp. 1598-1605, 1994.

[4] J. Benek, J. Steger, F. Dougherty and P. Buni, “Chimera: A Grid-Embedding Technique,” Arnold Engineering Development Center; Arnold AFS TN.;, 1986.

[5] W. Z. Shen, M. O. L. Hansen and J. N. Sorensen, “Determination of Angle of Attack (AOA) for Rotating Blades,” [Online]. Available: http://orbit.dtu.dk/fedora/objects/orbit:46902/datastreams/file_2525365/content. [Accessed 15 July 2015].

[6] H. Leipprand, “Development and validation of evaluation tool for 3D, unsteady CFD simulations,” Institute of Aerodynamics and Gas Dynamics, Stuttgart, 2015.

[7] M. Schuff, P. Kranzinger, M. Keßler and E. Krämer, “Advanced CFD-CSD coupling: Generalized, high performant, radial basis function based volume mesh deformation algorithm for structured, unstructured and overlapping meshes,” in *40th European Rotorcraft Forum*, Southhampton, 2014.

[8] S. Daynes and P. M. Weaver, “A morphing trailing edge device for a wind turbine,” *Journal of Intelligent Material Systems and Structures,* pp. 691-701, 6 March 2012.

[9] H. A. Madsen, P. B. Andersen, T. L. Andersen, C. Bak and T. Buhl, “The potentials of the controllable rubber trailing edge flap (CRTEF),” in *Proceedings of EWEC*, 2010.

[10] B. Lambie, “Aeroelastic Investigation of a Wind Turbine Airfoil with Self-Adaptive Camber-Doctoral thesis,” TU Darmstadt, 2011.

[11] E. Jost, A. Fischer, T. Lutz and E. Krämer, “CFD studies of a 10 MW wind turbine equipped with active trailing edge flaps,” in *10th EAWE PhD seminar on Wind Energy in Europe*, Orleans, 2014.

[12] T. Theodorsen, “General Theory of Aerodynamic Instability and the Mechanism of Flutter,” NACA Report 496, 1935.

[13] J. G. Leishman, “Challenges in Modelling the Unsteady Aerodynamics of Wind Turbines,” *Wind Energy,* pp. 85-132, 5 2002.

[14] N. Sorensen, M. Hansen, N. Garcia, E. Jost, T. Lutz, L. Florentie and K. Boorsma, “AVATAR Deliverable 2.3: Power Curve Predictions,” 1 June 2015. [Online]. Available: http://www.eera-avatar.eu/fileadmin/mexnext/user/report-d2p3.pdf.

[15] K. Meister, T. Lutz and E. Krämer, “Simulation of a 5MW wind turbine in an atmospheric boundary layer,” in *Torque Conference 2012*, Oldenburg, 2012.

3 VALIDATION 2: LOAD ALLEVIATION CAPABILITIES OF AN SMA SHAPE MORPHING CONCEPT (NTUA)

3.1 Aeroelastic load control simulations

The possibility of alleviating wind turbine blades loads using shape morphing techniques is investigated in the present section. The load alleviation is based on the development of wind turbine blade sections capable of drastically varying their curvature with time. Morphing is considered as the ability of a structure to undergo pronounced geometry adaptations to optimally and timely respond to a variety of operational conditions. It is a bio-mimetic approach and has been identified as a disruptive future technology for maximizing efficiency of lightweight structures.

The present work is the extension of the work presented in deliverable D2.3.1 [1] where the preliminary assessment of the performance of **Shape Memory Alloy (SMA) actuators** as shape morphing devices has been performed in the context of a simplified aeroelastic analysis. In the present report shape morphing techniques are assessed in a more complete "high fidelity" modelling environment (hGAST [2]) where the aerodynamics of the full rotor, the structural dynamics and the control system of the complete wind turbine are considered. The analysis concerns the DTU Reference Innwind.eu 10 MW wind turbine (RWT) [Ref] and emphasis is mainly put in testing different trailing edge (TE) shape morphing variations as well as different sensors and control schemes that could fit to the time response characteristics of SMA type actuators.
Various operational conditions including normal operation, occurrence of faults of the flap actuators and parked (idling) conditions (as defined in the standards [3]) are considered in the analysis. The possibility of alleviating both fatigue and extreme loads is investigated.

3.2 Design load cases

A subset of Design Load Cases (DLC) from the IEC 61400-1.3 standard formed the basis of the present study. Different operational conditions including normal operation, occurrence of faults of the flap actuators and parked (idling) conditions are considered in the analysis. In particular, the DLCs 1.2 (NTM), 1.3 (ETM), 2.2 and 6.1 (EWM) of the IEC 61400-1.3 have been simulated.

The list of the DLCs simulated by NTUA is presented in **Table 9**, with the fault conditions described in Chapter 1.

Table 9 – List of DLCs performed by NTUA.

DLC	seeds	wind speeds (m/s)	description
1.2	R1-R6	12, 14, 16, 20	
1.3	R1-R6	12, 14, 16, 20	
2.2	R1-R6	12	FAULT1
2.2	R1-R6	12	FAULT2
2.2	R1-R6	12	FAULT3
6.1	R1	42.5	

3.3 Modelling Environment and Configuration

The DTU 10MW Reference Wind Turbine (RWT) [4] is used for the simulations in the aeroelastic code hGAST [2], as a representative modern multi-MW wind turbine model utilized in the INNWIND project. The unsteady aerodynamics associated with the TE active shape variations is accounted for by using FOILFS. FOILFS is an inviscid aerodynamic model (based on linear aerodynamic theory) that simulates unsteady aerodynamics due to arbitrary camber line variations of a 2D airfoil. FOILFS is enhanced with ONERA model in order to be able to take into account dynamic stall conditions. FOILFS requires as input steady-state lift, drag, and moment characteristics for the various airfoil deflected shapes which in the present analysis has been simulated in FOIL2W [5] (NTUA's viscous-inviscid interaction code), with simulations performed at a Reynold's number of 4.5x10^6 for transitional conditions. FOILFS is integrated into hGAST and provides unsteady, sectional aerodynamic charactersitics of the blade sections installed with shape morphing actuators.

Different TE shape morphing configurations have been considered in the present analysis.

The first configuration (**CONF1**) is chosen based on prior studies [6] performed under WP2 of the UPWIND project by the same partners also involved in Task 2.3 of Innwind.EU project. It was agreed upon the partners that this configuration would consitute the baseline configuration of the INNWIND project (**Table 10**).

Table 10: Baseline flap parameters (CONF1).

Flap configuration CONF1	
Chordwise extension	10%
Deflection angle limits	±10°
Spanwise length	25.9m (30% blade length)
Spanwise location	59.59m-85.50m (from blade root)
Airfoil	FFA-W3-241

The geometry of the deflected TE shape is shown in **Figure 42.** The C_L-α curves of the FFA-W3-241 airfoil for TE flap angles in the range [-10°, +10°] are shown in **Figure 43.**

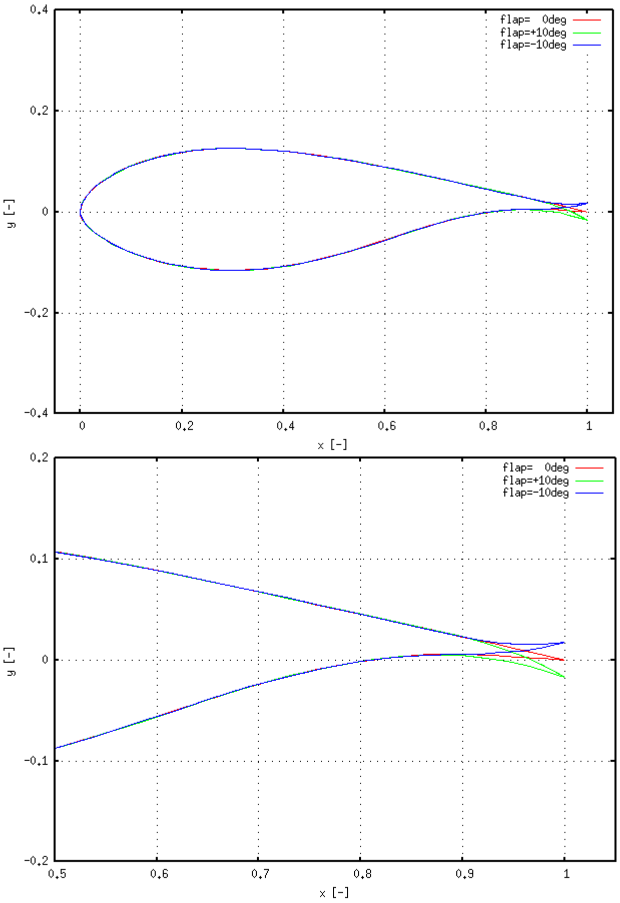

Figure 42: Baseline TE flap deflected geometry of FFA-W3-241 (+/-10° angle).

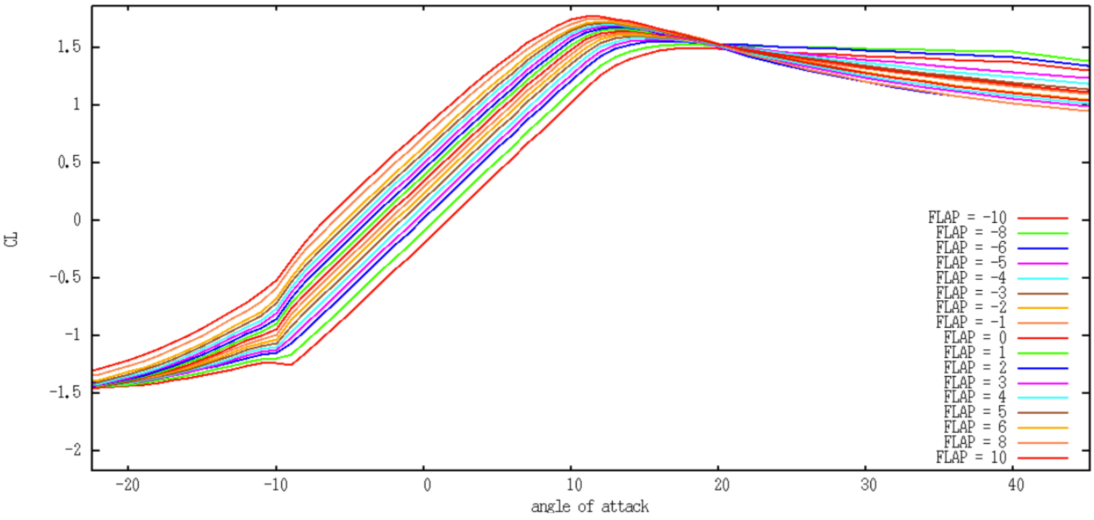

Figure 43: Steady-state C_L-aoa characteristics of Baseline flap geometry (10% extent).

A second TE flap configuration that extends to 30% of the chord was also defined. Morphing capabilities of SMAs are higher than those of other type of actuators and therefore camber line morphing can be extended to a bigger portion of the section chord. Previous studies presented in D2.3.1 [1] (see **Figure 44**) have shown that SMAs actuators can easily support a modular type of shape morphing that allows TE flaps to extend to a higher percentage of the chord. Thus, TE flaps of 30% chordwise extent become feasible.

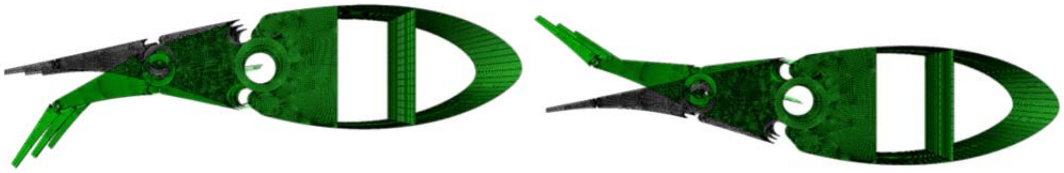

Figure 44: Morphing capabilities by applying a modular flap controlled by SMAs.

The deflected shape of the camber line (in the vicinity of the TE) was chosen to follow a C^1 spline curve where (as shown in **Figure 45**) $y_1 = y_1' = 0$, $y_2 = 0.3 \tan\beta$ where β is the TE flap angle and the only free parameter of the curve is the slope y_2' at the TE point.

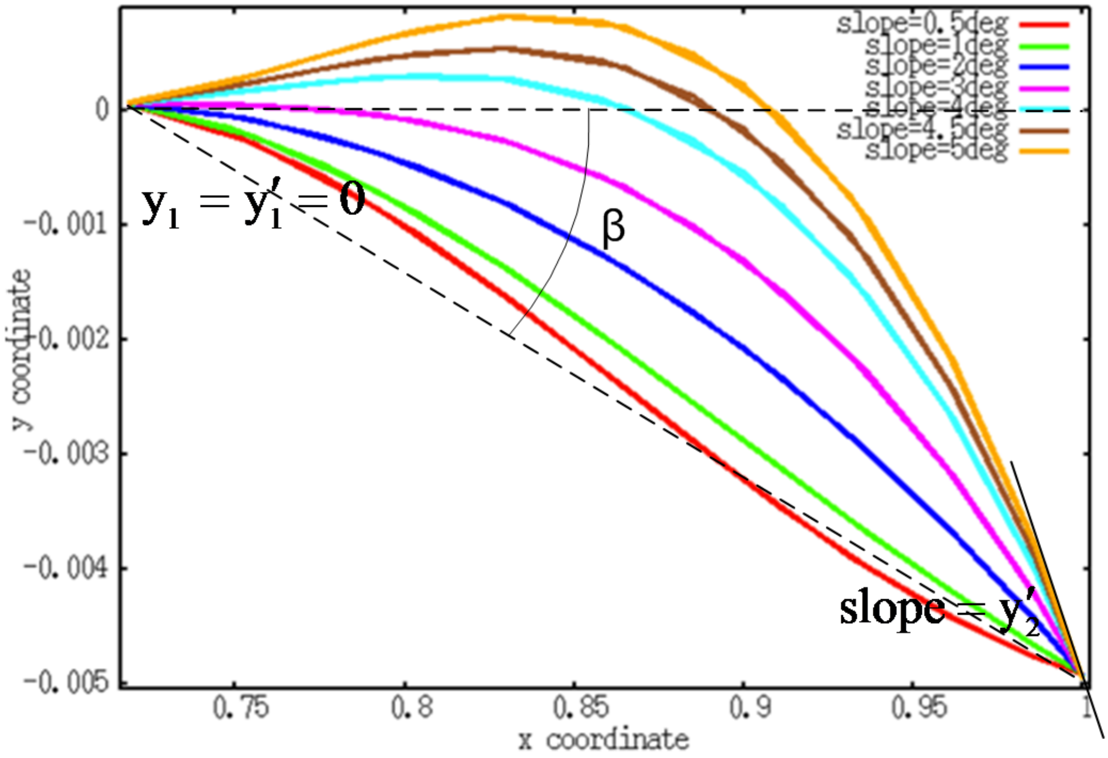

Figure 45: Alternative camber line deflected shapes for 30% TE flap (+1° angle).

The geometry of the FFA-W3-241 airfoil for different slopes at the TE and a deflection angle of +5° is shown in **Figure 46.** Camber lines with higher curvature (and therefore higher slope values) are well suited for the modular type of flap shown in **Figure 44.** The actuation requirements are smaller for the inner (stiffer) part while at the same time a high flap angle can be achieved by moving more the outer part. A direct consequence of the higher curvature is to achieve a higher C_L variation for the same flap angle. This is illustrated in **Figure 47** where the C_L-α curves for slopes of 3°,4°,4.5° are ploted for a flap deflection angle of 2°. It is clear that the higher is the slope the bigger is the ΔC_L due to the deployment of the flap however at a decreasing rate. As a good comprimise of shape deformation and achieved ΔC_L the 4° slope was finally chosen for the analysis that follows. The C_L-α curves of the FFA-W3-241 airfoil for the 30% flap and TE flap angles in the range [-10°, +10°] are shown in **Figure 48.**

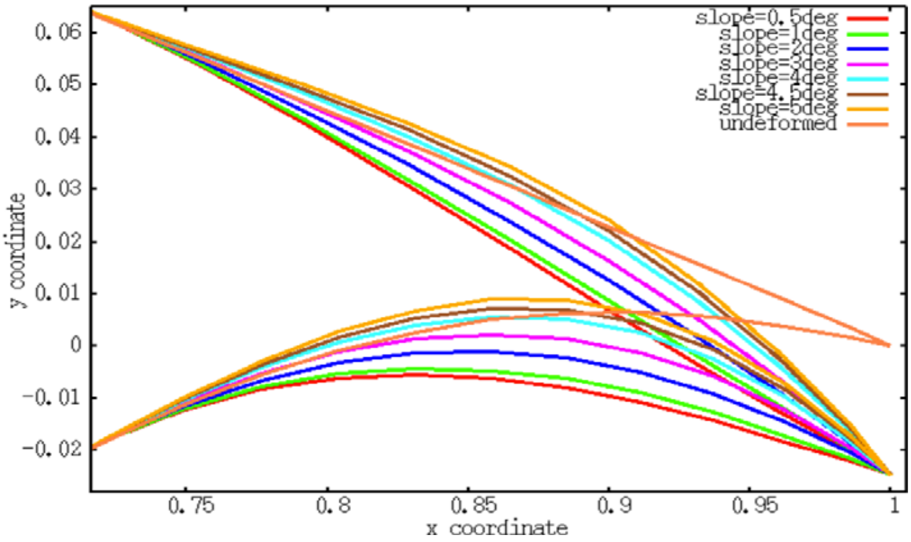

Figure 46: Alternative airfoil deflected shapes for 30% TE flap (+5^o angle).

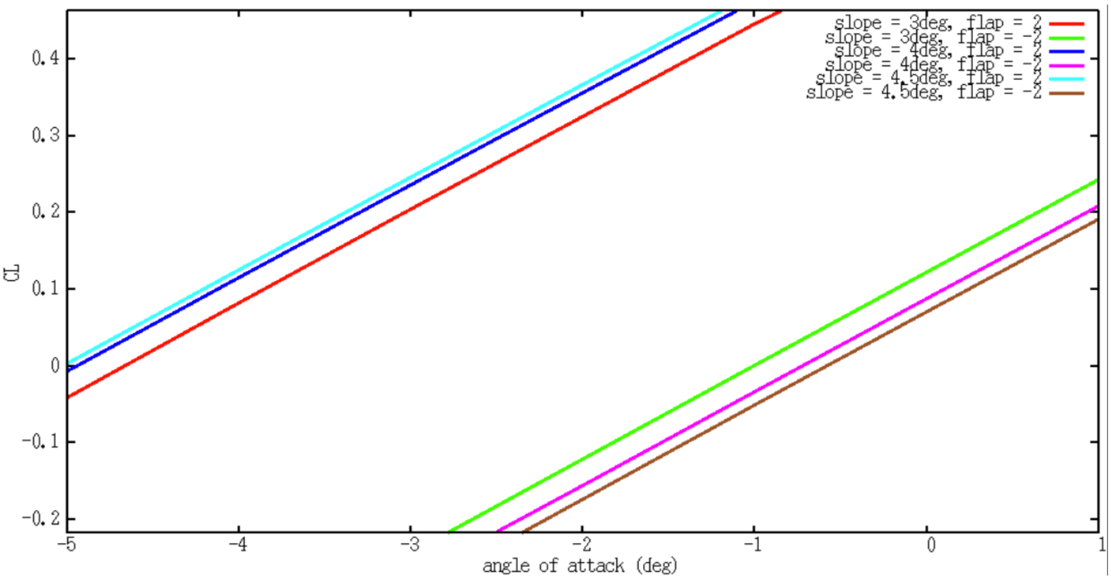

Figure 47: Effect of TE slope on CL-aoa curves.

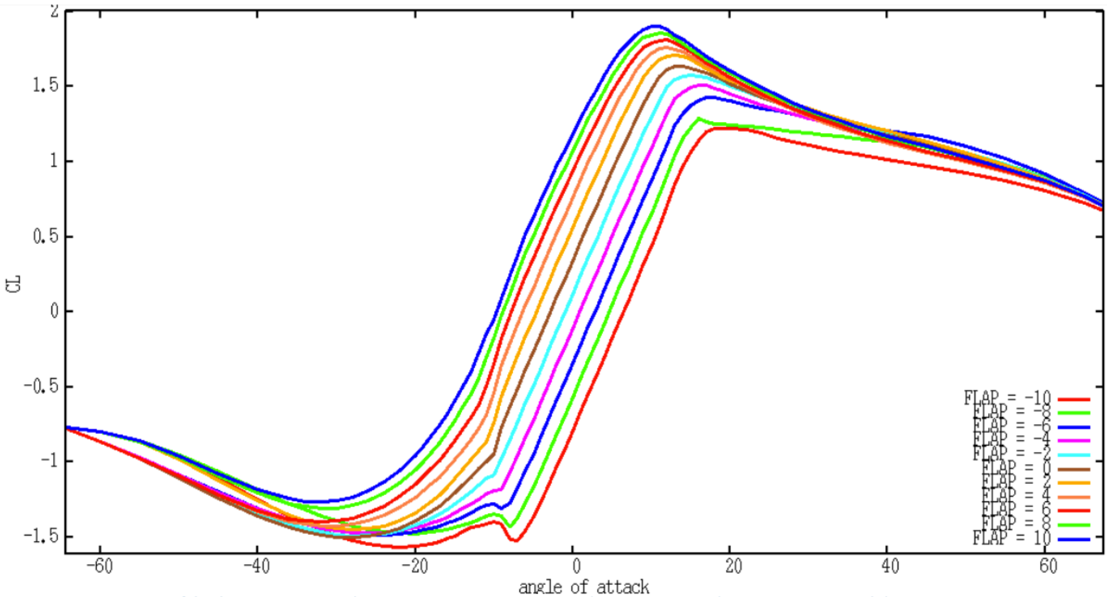

Figure 48: Steady-state C_L-aoa characteristics of Alternative flap geometry (30% extent).

With the 30% flap two additional flap configurations have been defined (see Table 11 and Table 12).

Table 11: Alternative flap parameters (CONF2).

Flap configuration CONF2	
Chordwise extension	30%
Deflection angle limits	±10°
Spanwise length	20m
Spanwise location	60m-80m (from blade root)
Airfoil	FFA-W3-241

Table 12: Alternative flap parameters (CONF3).

Flap configuration CONF3	
Chordwise extension	30%
Deflection angle limits	±10°
Spanwise length	10m
Spanwise location	75m-85m (from blade root)
Airfoil	FFA-W3-241

3.4 Controllers

Two control strategies have been employed in the present analysis.

- A typical cyclic flap control
- An individual flap control similar to the one presented in D2.3.1

The first loop is illustrated in **Figure 49.**

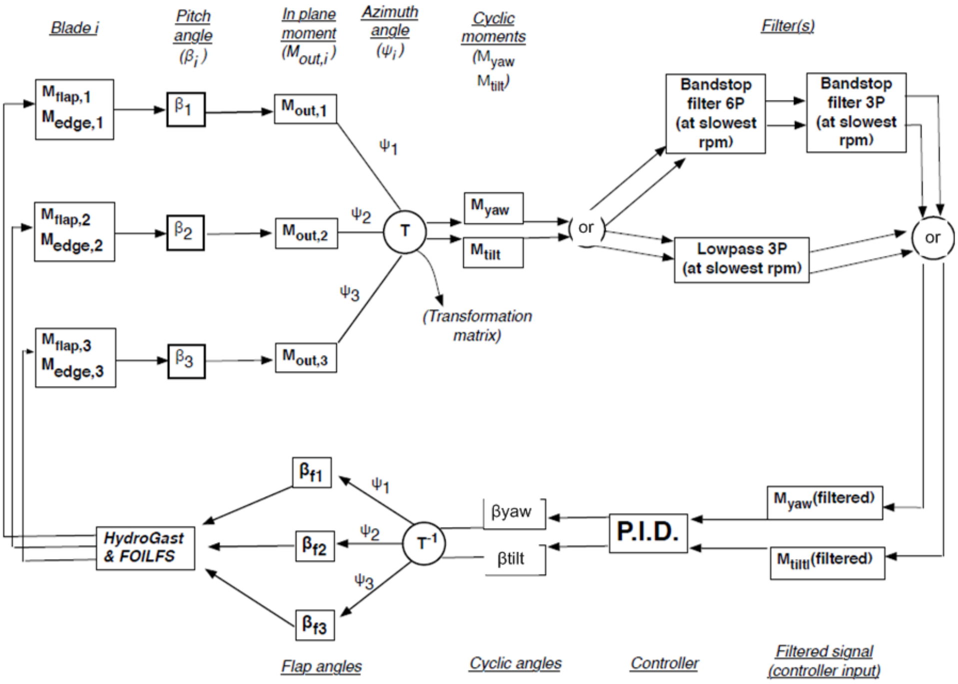

Figure 49: Cyclic flap control loop block diagram.

The blade root bending moment input signals are transformed into yaw and tilt moments M_{yaw} and M_{tilt}. 3P and 6P bandstop filters are applied on M_{yaw} and M_{tilt}. The filtered moments are passed through an integral control element and the β_{yaw} and β_{tilt} angles are obtained which are then transformed into flap angles for the three blades.

The second control loop is illustrated in **Figure 50**.

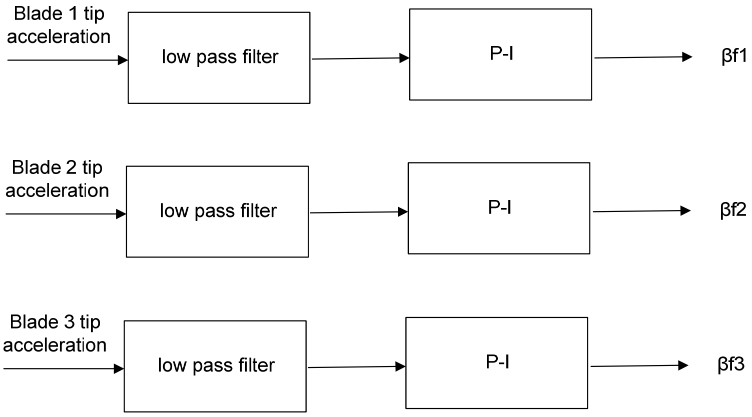

Figure 50: Individual flap control loop block diagram.

The blade tip acceleration input signal is first filtered. A fourth order **elliptic** lowpass filter has been applied in the present analysis to the acceleration input. The main driver for the selection of the filter parameters (edge frequency of the lowpass filters.) is the response speed of the SMA system. This is found to be relatively low especially during the cooling phase. The aim of the filter is to maintain at least the 1P frequency (0.16 Hz in the present case) which mainly drives blade fatigue loads. Other important requirements of the filter are (a) a small phase shift with respect to the input signal at the frequency of 1P (b) the lowest possible attenuation of the 1P variation.

The actuator dynamics are implemented in all controllers as a linear servo model in hGAST, for a first order system with a time constant of 0.1s.

The cyclic control approach is combined with the baseline flap configuration (CONF1) and the first alternative flap configuration (CONF2).

The individual flap control approach is combined with the second alternative flap configuration (CONF3). The basic parameters of the three flap and control configurations are listed below.

Table 13: Flap and control configurations.

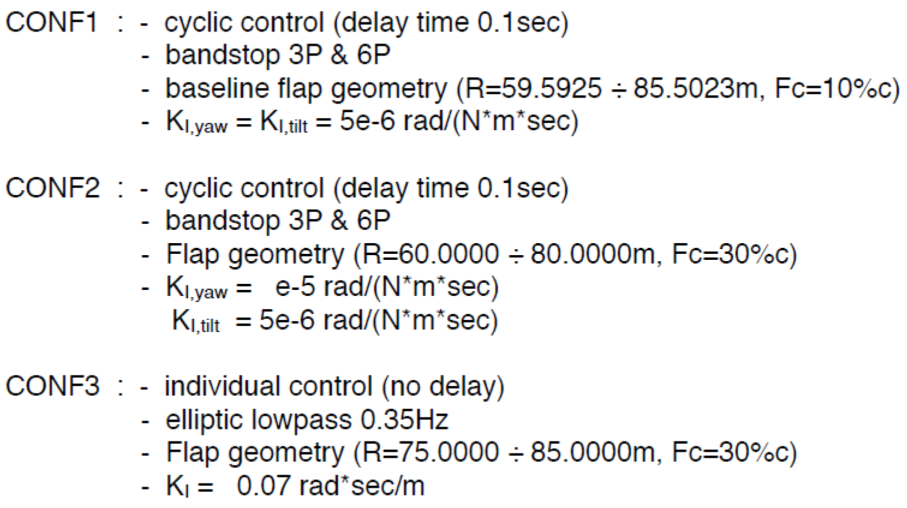

CONF1 : - cyclic control (delay time 0.1sec)
- bandstop 3P & 6P
- baseline flap geometry (R=59.5925 ÷ 85.5023m, Fc=10%c)
- $K_{I,yaw} = K_{I,tilt}$ = 5e-6 rad/(N*m*sec)

CONF2 : - cyclic control (delay time 0.1sec)
- bandstop 3P & 6P
- Flap geometry (R=60.0000 ÷ 80.0000m, Fc=30%c)
- $K_{I,yaw}$ = e-5 rad/(N*m*sec)
  $K_{I,tilt}$ = 5e-6 rad/(N*m*sec)

CONF3 : - individual control (no delay)
- elliptic lowpass 0.35Hz
- Flap geometry (R=75.0000 ÷ 85.0000m, Fc=30%c)
- K_I = 0.07 rad*sec/m

It is noted that cyclic flap approach cannot be combined with a very short flap as the one chosen for CONF3. Basic requirement of the cyclic flap control approach is the zeroing of the mean yaw and tilt moments which cannot be accomplished with a very short flap. Therefore the challenge of individual flap control is the alleviation of the loads with the use of flap that occupies only 10% of the blade span.

3.5 Results Normal Operation

Typical time series results of the blade root flapwise bending moment for the three control configurations described above are shown in **Figure 51** - **Figure 53** for the wind speed of 12 m/s and for normal turbulence conditions (NTM). The corresponding flap angle time series are presented in **Figure 54** - **Figure 56.** It is noted that both for CONF1 and CONF2 (cyclic control) a smooth angle variation is obtained. For CONF1 the variation of the flap angle is very high and the flap angle continuously hits the 10° bound both for positive and negative angles. In CONF3 (individual flap) higher frequency fluctuations are seen in the flap angle response however the overall variation of the flap angle is smaller (smaller range of flap angle variation).
The fatigue load alleviation capabilities of the three control options are presented in **Figure 57-Figure 64** in terms of the (1Hz) equivalent fatigue loads both for NTM and ETM. The results presented in the figures are normalised (with respect to the non-controlled case); average values of the six realisations performed are presented.

The following comments can be made concerning the different load components:

- A substantial reduction of the flapwise moment is achieved at all wind speeds and flap configurations that ranges between 6%-18%
- The reduction of the flapwise moment is higher for NTM conditions
- Slightly higher flapwise moment reduction is obtained at 12m/s wind speed
- A slight reduction of the edgewise moment (1%-2%) is noted at all wind speeds and configurations but CONF3 at 12m/s.
- A slight increase of the tower fore-aft bending moment is seen at all wind speeds for CONF1 and CONF2 while a slight reduction is noted for CONF3.

- A noticeable reduction of the lateral bending moment is seen at all wind speeds and configurations

As regards the three configurations

- Higher load reduction is noted for CONF2. The reduction of the flapwise moment ranges between 15%-18% for NTM
- CONF1 gives a 10%-13% reduction of the flapwise moment
- CONF3 gives 8%-11% reduction of the flapwise moment

Figure 65 - Figure 66 present standard deviations (sdv) of the flap angle for the three control configurations and the two turbulence models. It is seen that the highest sdvs are noted for CONF1 and the lowest for CONF3. As already discussed the difference between cyclic and individual flap control is that in the individual control case high frequency fluctuations are obtained, however, the flap angle excursions are much lower compared to those of CONF1 and CONF2. Also, as the wind speed increases the sdv increases in all configurations.

Extreme (ultimate) loads are presented in Figure 67 and Figure 68. Maximum and minimum loads for ETM are presented in the figures. It seen that the ultimate load increases with cyclic flap control (see 16 m/s wind speed where CONF1 and CONF2 loads are higher than the maximum of the uncontrolled case) but decreases with the individual control. The minimum load is always lower (in absolute value) for all control configurations. A good performance of all three control configurations is noted only at the wind speed of 12 m/s where a significant load reduction is obtained.

In Figure 69 - Figure 71 the time series of the wind velocity, flapwise bending moment and flap angle are presented for CONF2 for the mean wind speed of 12 m/s. It is seen that the extreme load occurs when the wind speed increases from 4 m/s to 12 m/s within approximately 10 s. The flap control responds with negative flap angle values when the peak loads occurs and this leads to a reduction of the extreme load.

In Figure 72 - Figure 75 the time series of the wind velocity, flapwise bending moment and flap angle are presented for CONF2 and CONF3 for the mean wind speed of 16 m/s. It is seen that the extreme load occurs when the wind speed increases from 4 m/s to 12 m/s within approximately 7 s. In this case TE flap moves down (from negative to positive values). When the peak load occurs the direction of the flap motion must change (towards negative angles) in order to limit the load. The response of the flap is not that fast in this case. A small knee appears in the flap angle response at the time instant of the peak load which cannot efficiently limit the peak load. On the contrary a faster response is noted in CONF3. When the peak load appears the flap angle moves fast towards negative angles and the peak load is decreased.
In Figure 76 the maximum and minimum loads due to fault operation of the flap control are compared to normal operation conditions. It is seen that a small increase of the peak loads is obtained only for fault1 and fault2 conditions.

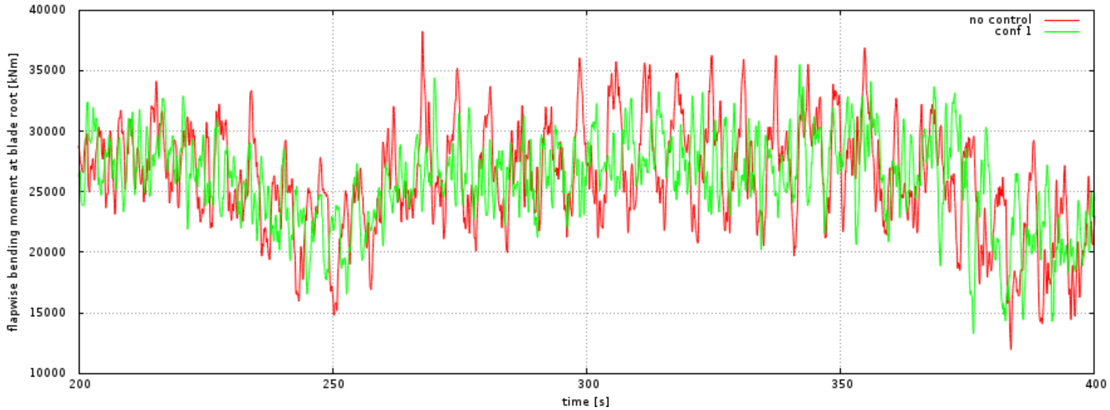

Figure 51: Flapwise bending moment at blade root. Comparison of uncontrolled against CONF1. Wind speed 12m/s, NTM.

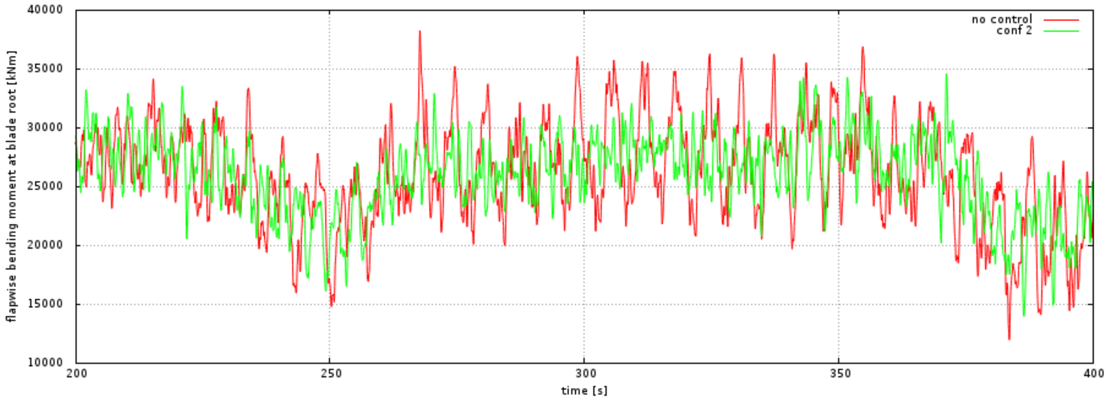

Figure 52: Flapwise bending moment at blade root. Comparison of uncontrolled against CONF2. Wind speed 12m/s, NTM.

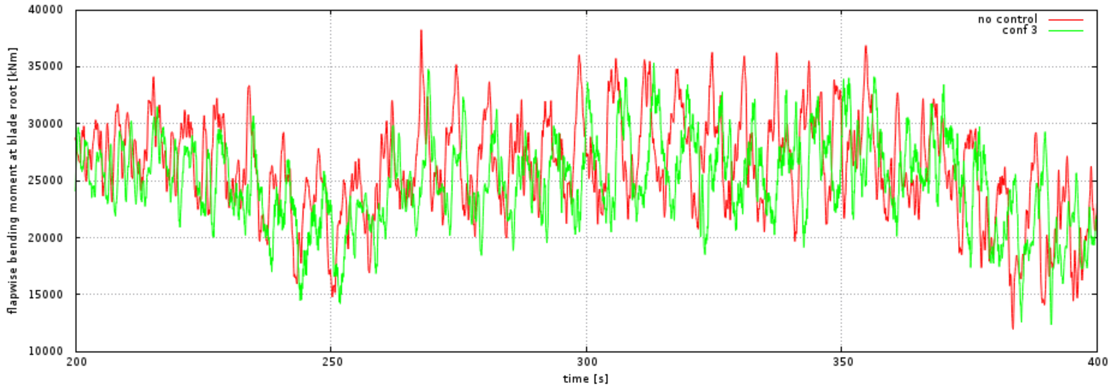

Figure 53: Flapwise bending moment at blade root. Comparison of uncontrolled against CONF3. Wind speed 12m/s, NTM.

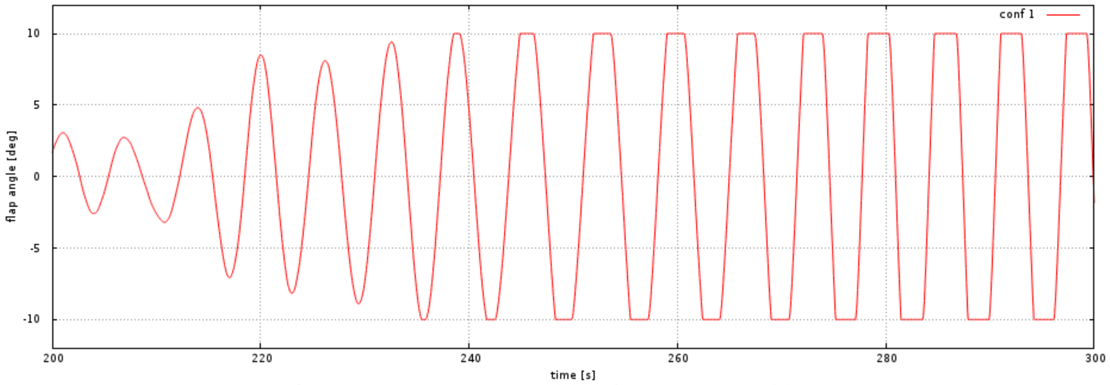

Figure 54: Flap angle time series (CONF1). Wind speed 12m/s, NTM.

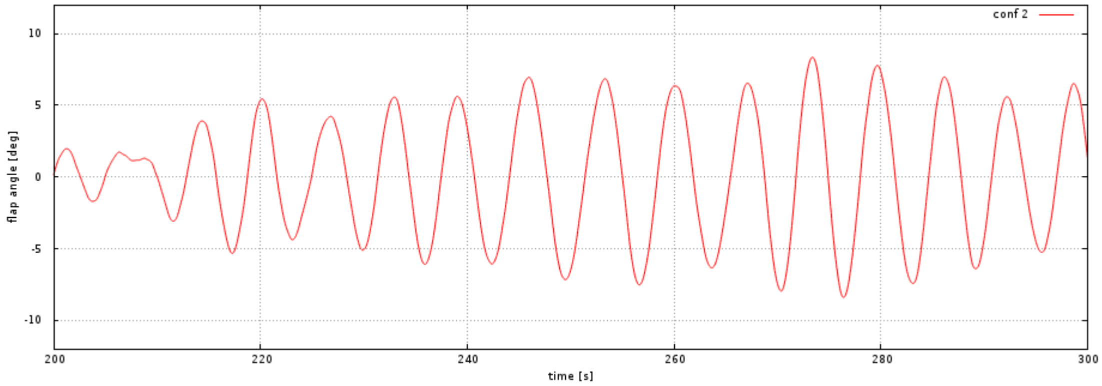

Figure 55: Flap angle time series (CONF2). Wind speed 12m/s, NTM.

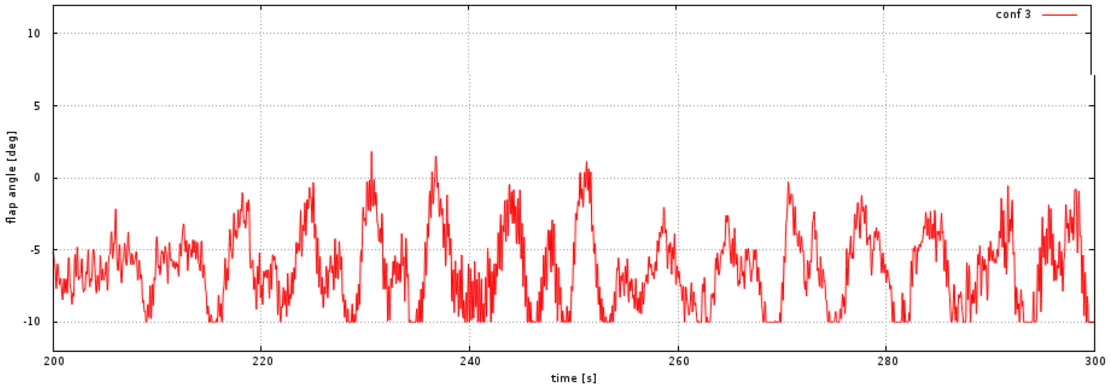

Figure 56: Flap angle time series (CONF3). Wind speed 12m/s, NTM.

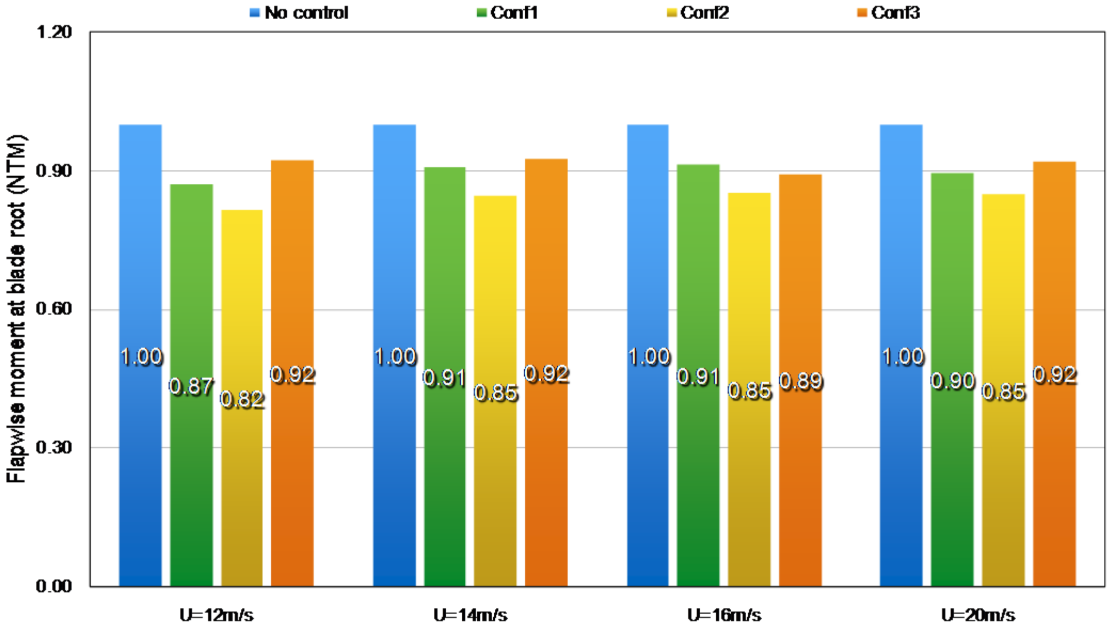

Figure 57: Normalized equivalent flapwise bending moment at blade root (m=12). External conditions NTM.

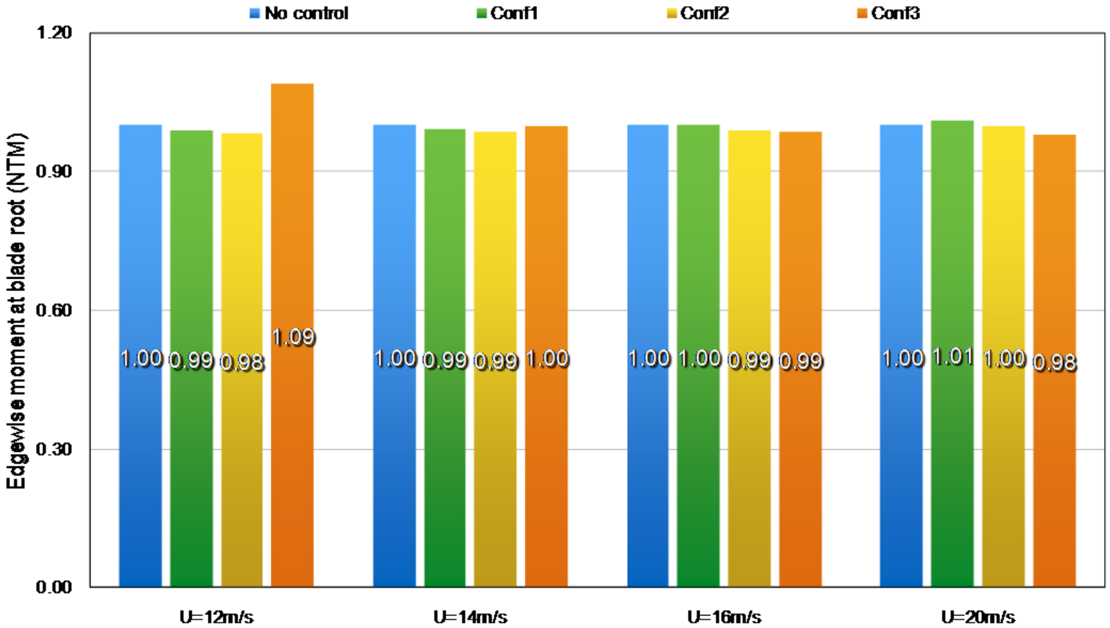

Figure 58: Normalized equivalent edgewise bending moment at blade root (m=12). External conditions NTM.

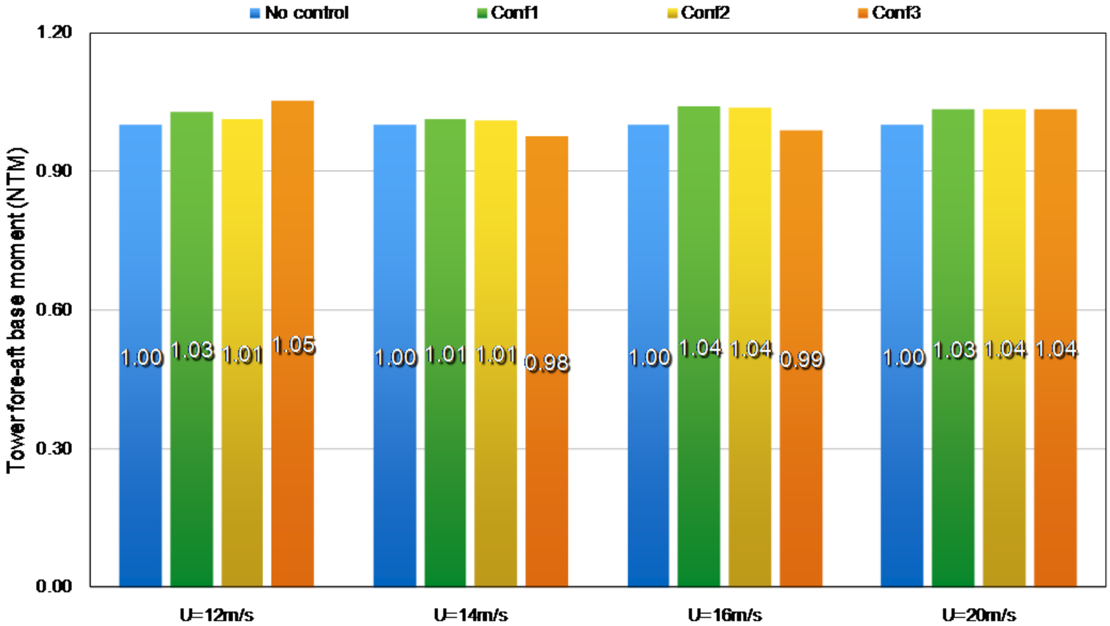

Figure 59: Normalized equivalent tower base fore-aft bending moment (m=4). External conditions NTM.

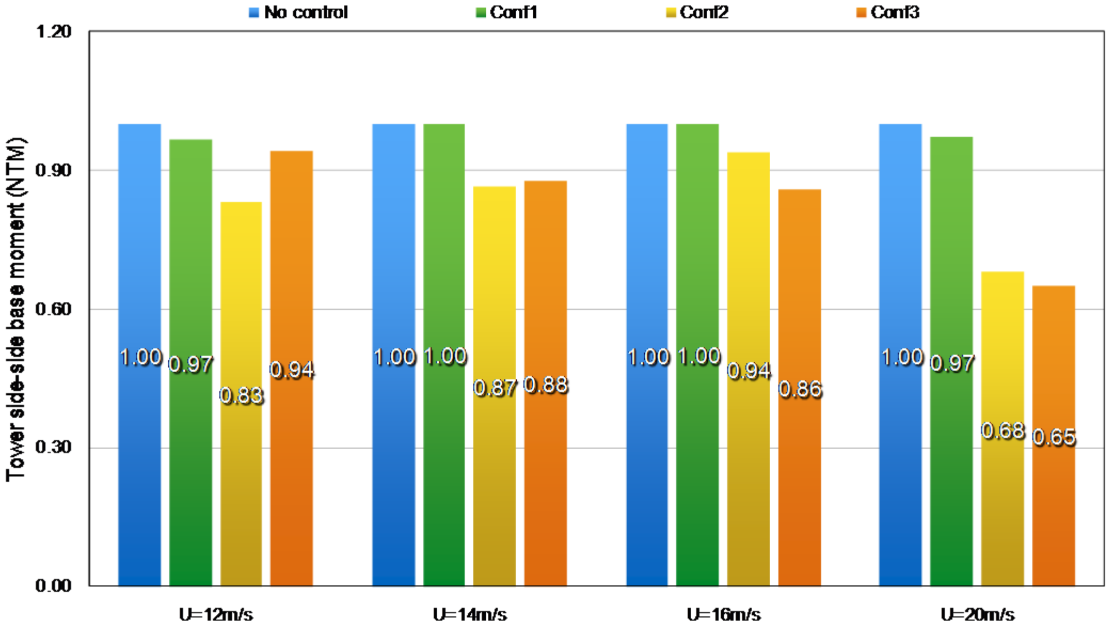

Figure 60: Normalized equivalent tower base lateral bending moment (m=4). External conditions NTM.

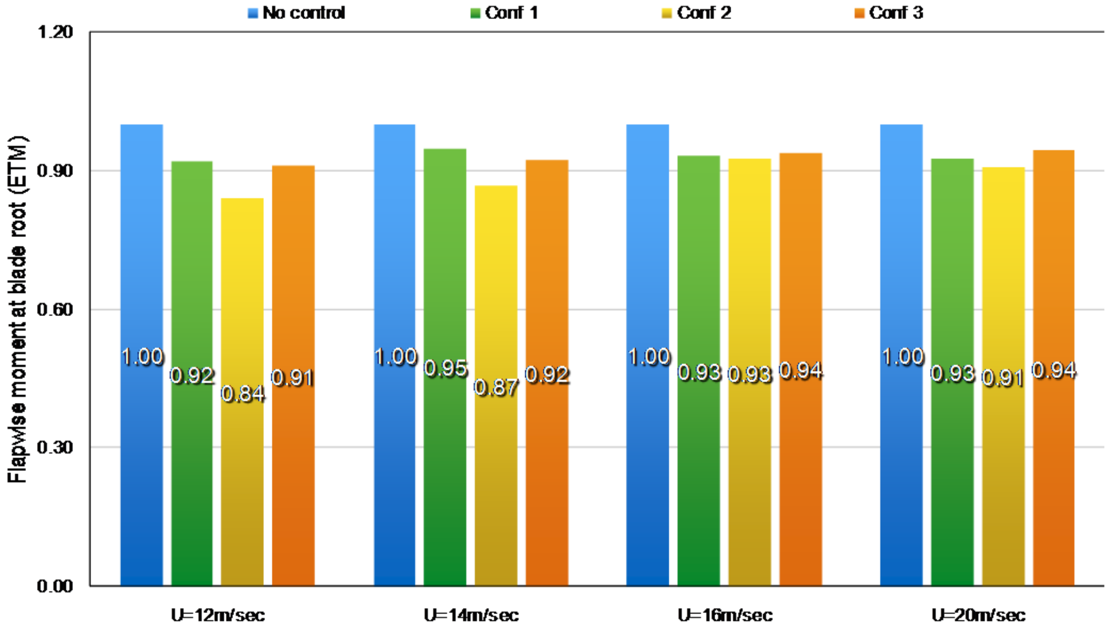

Figure 61: Normalized equivalent flapwise bending moment at blade root (m=12). External conditions ETM.

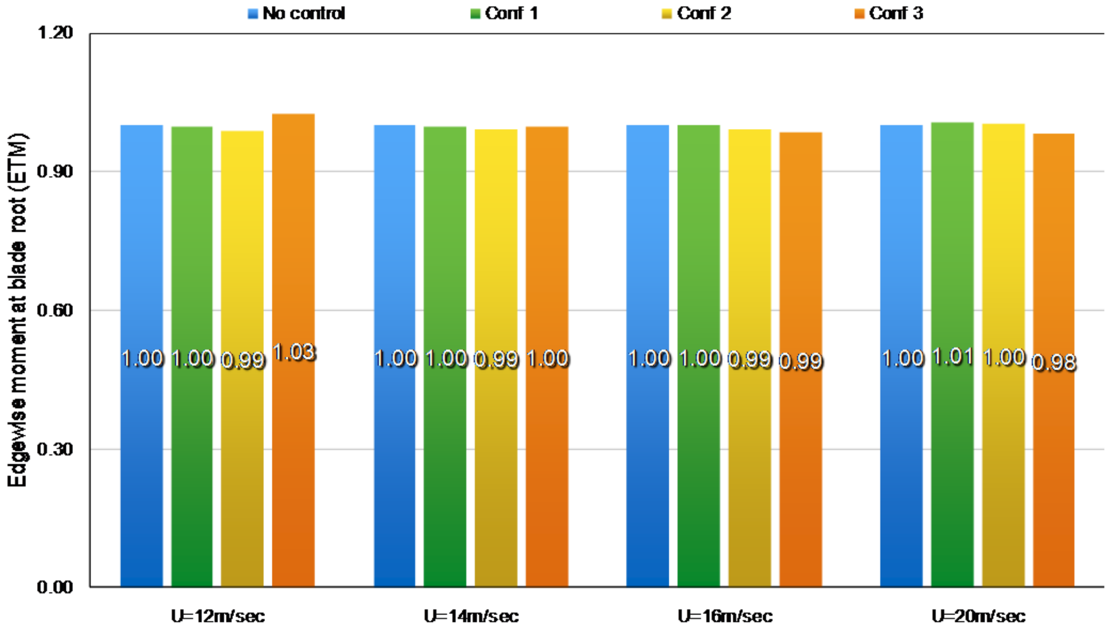

Figure 62: Normalized equivalent edgewise bending moment at blade root (m=12). External conditions ETM.

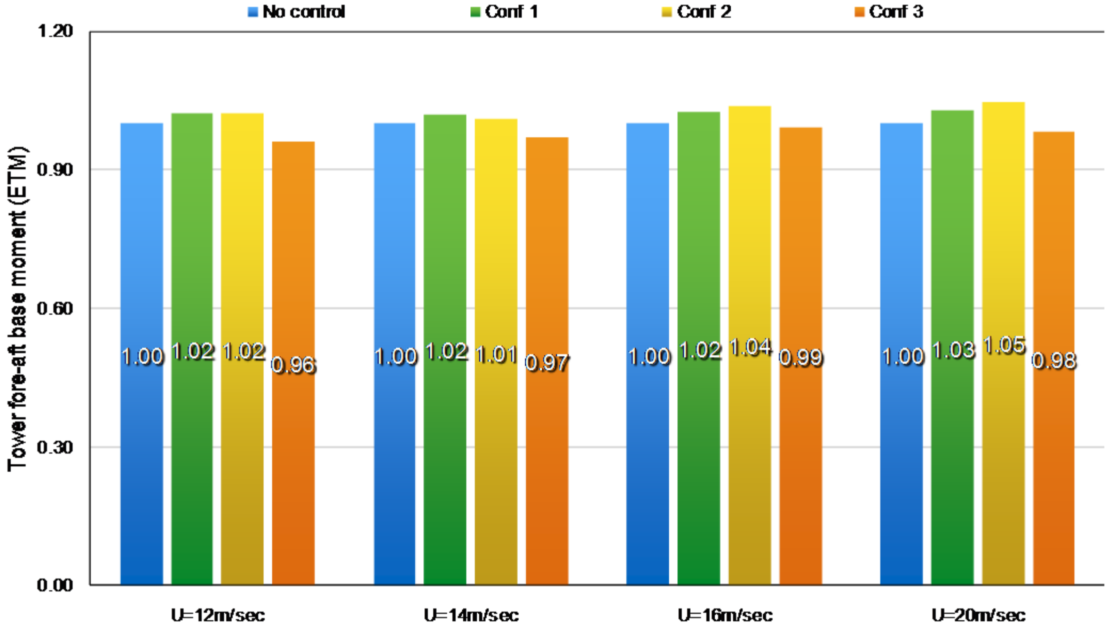

Figure 63: Normalized equivalent tower base fore-aft bending moment (m=4). External conditions ETM.

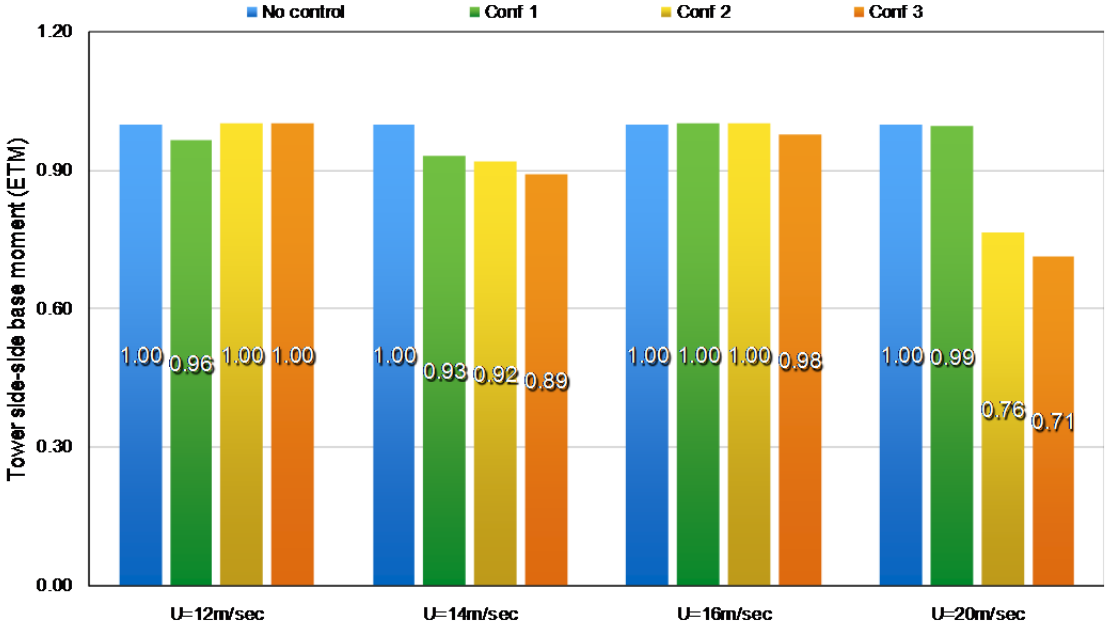

Figure 64: Normalized equivalent tower base lateral bending moment (m=4). External conditions ETM.

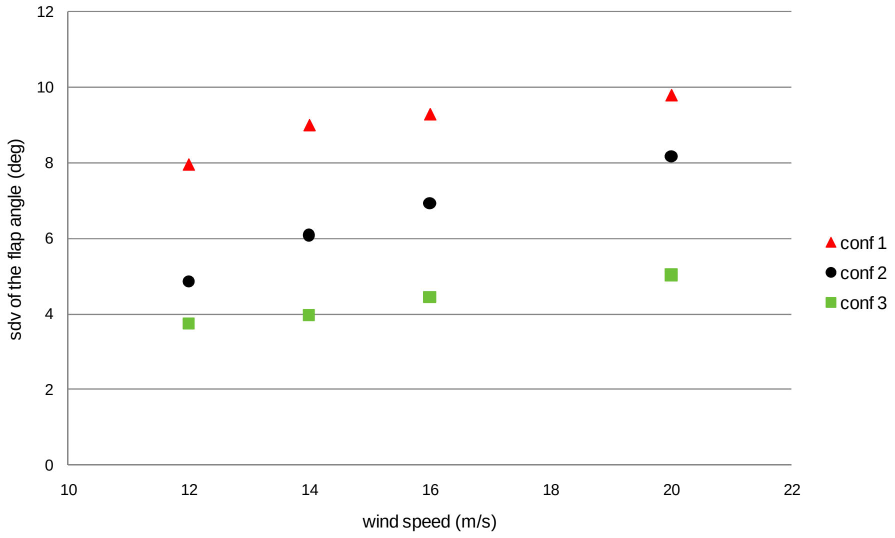

Figure 65: Standard deviation of the flap angle. External conditions NTM.

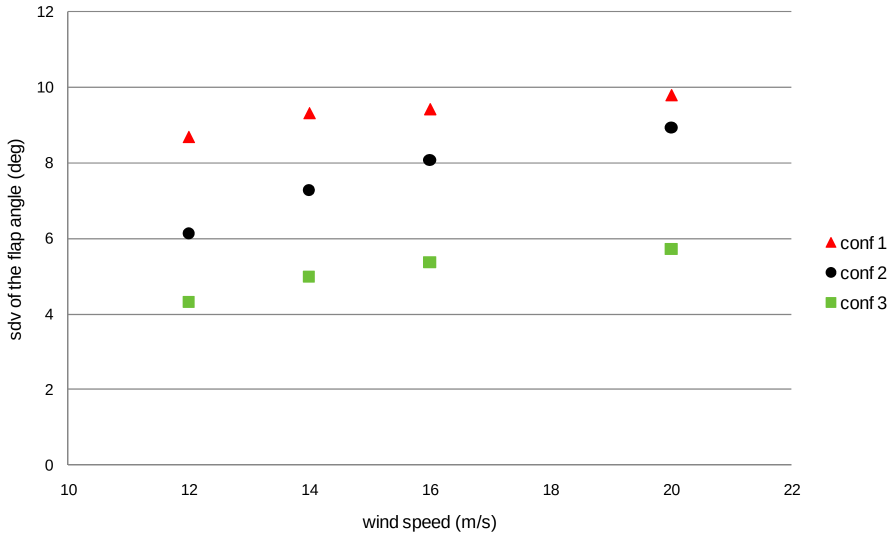

Figure 66: Standard deviation of the flap angle. External conditions ETM.

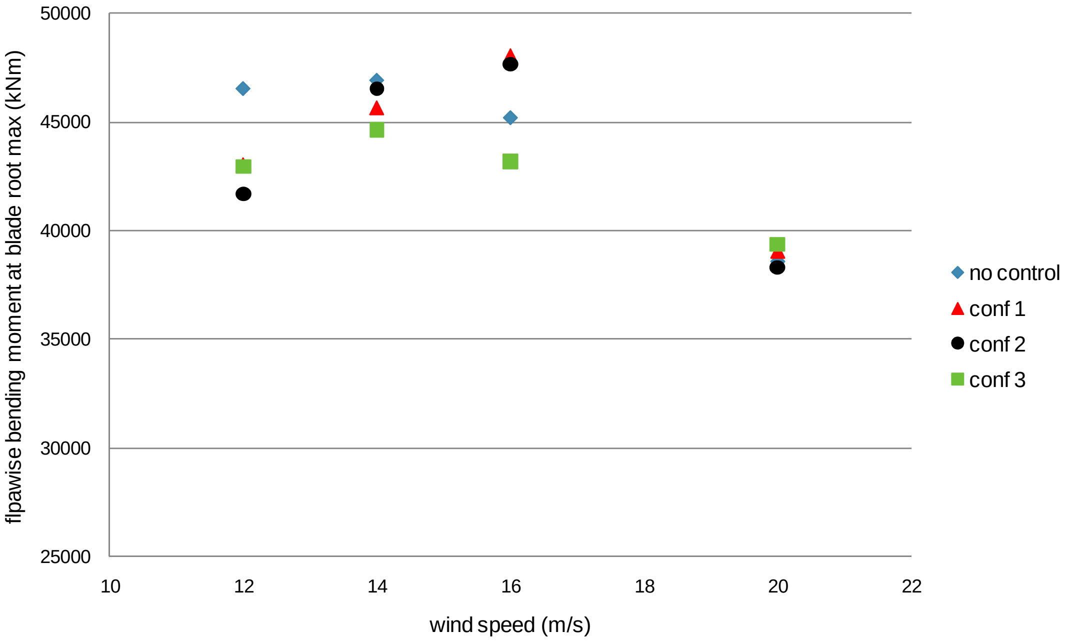

Figure 67: Max. flapwise bending moment at blade root. External conditions ETM.

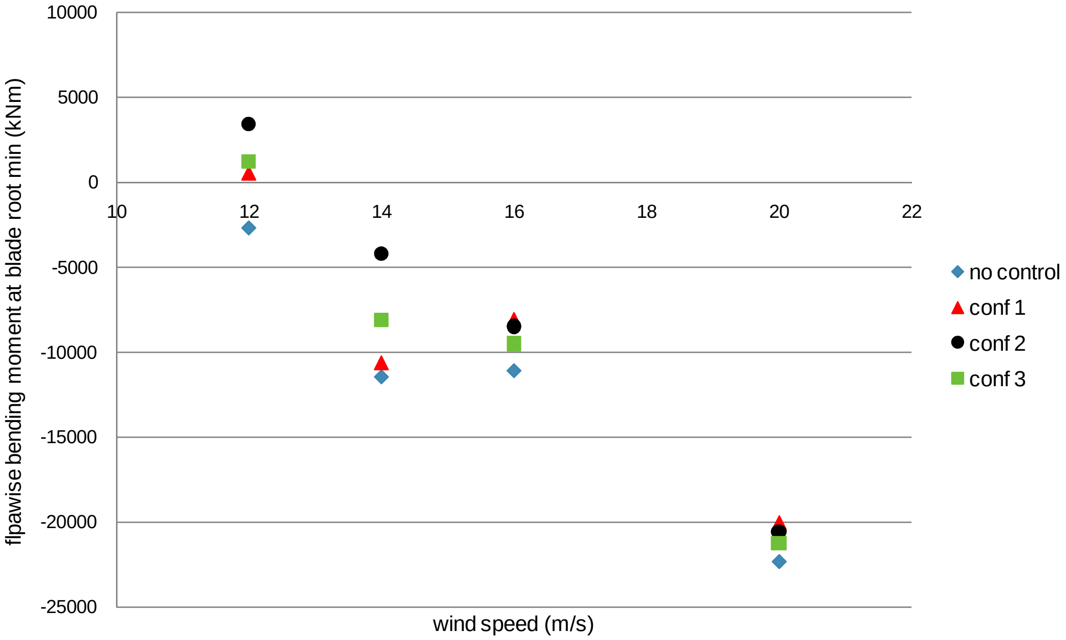

Figure 68: Min. flapwise bending moment at blade root. External conditions ETM.

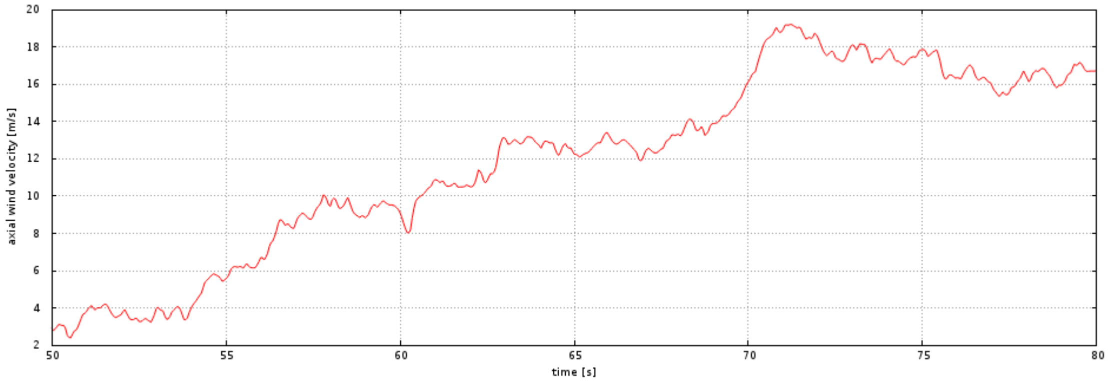

Figure 69: Time series of the wind velocity. Wind speed 12m/s, R5, ETM.

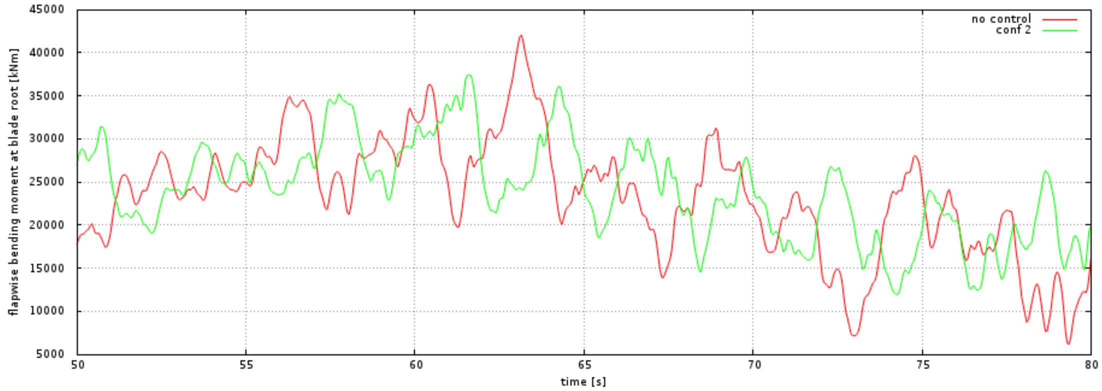

Figure 70: Time series of the flapwise bending moment. Wind speed 12m/s, R5, ETM.

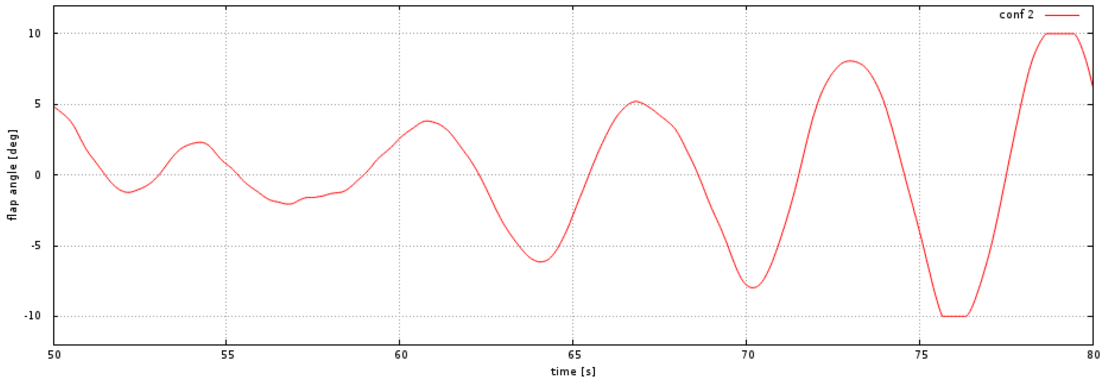

Figure 71: Time series of the flap angle. Wind speed 12m/s, R5, ETM.

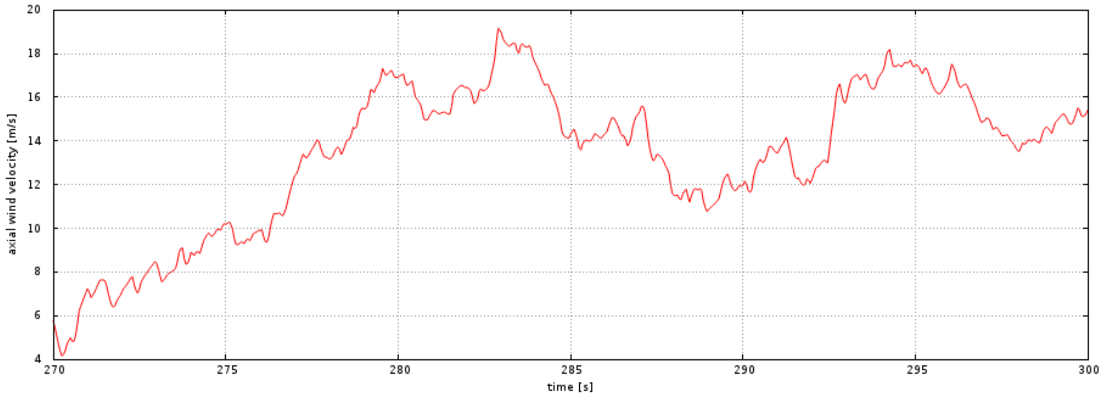

Figure 72: Time series of the wind velocity. Wind speed 16m/s, R5, ETM.

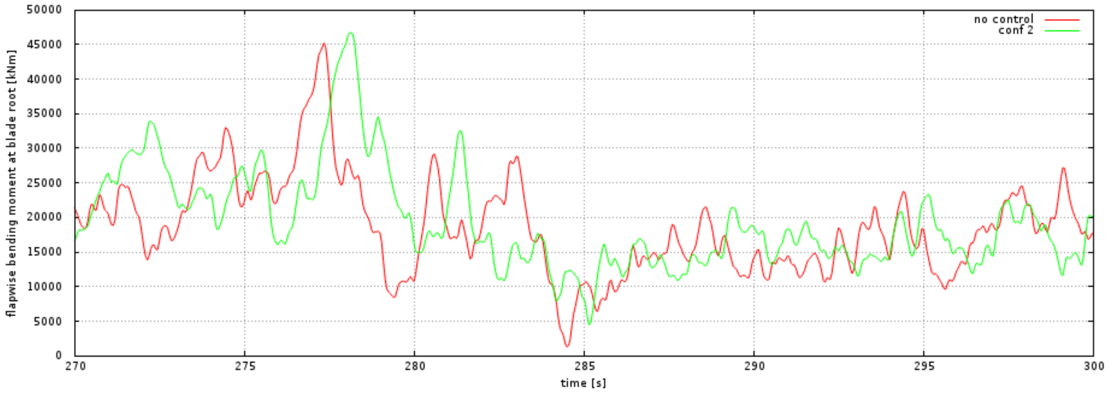

Figure 73: Time series of the flapwise bending moment. Wind speed 16m/s, R5, ETM.

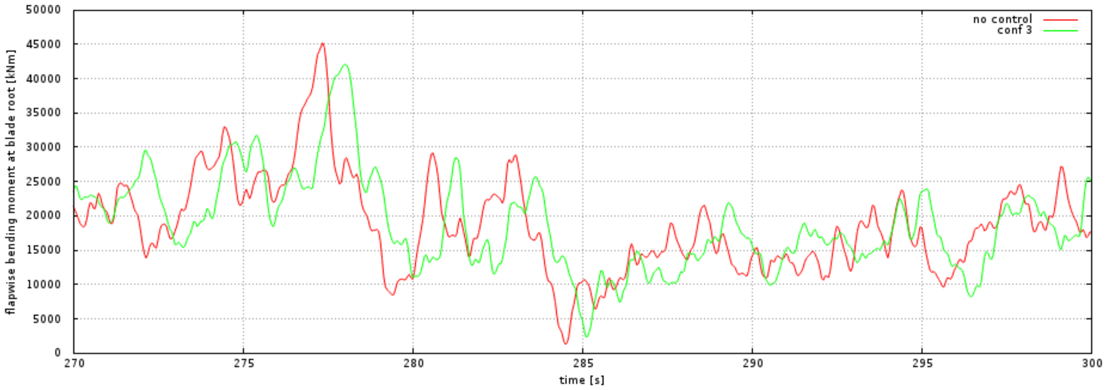

Figure 74: Time series of the flapwise bending moment. Wind speed 16m/s, R5, ETM.

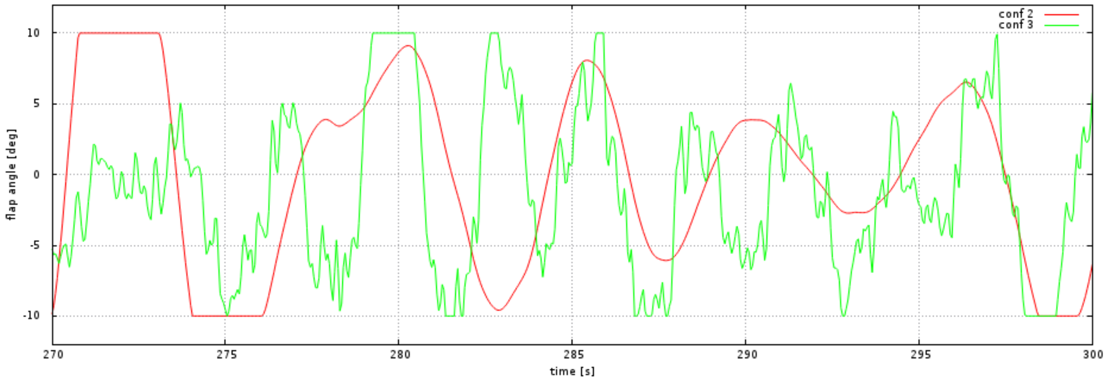

Figure 75: Time series of the flap angle. Wind speed 16m/s, R5, ETM.

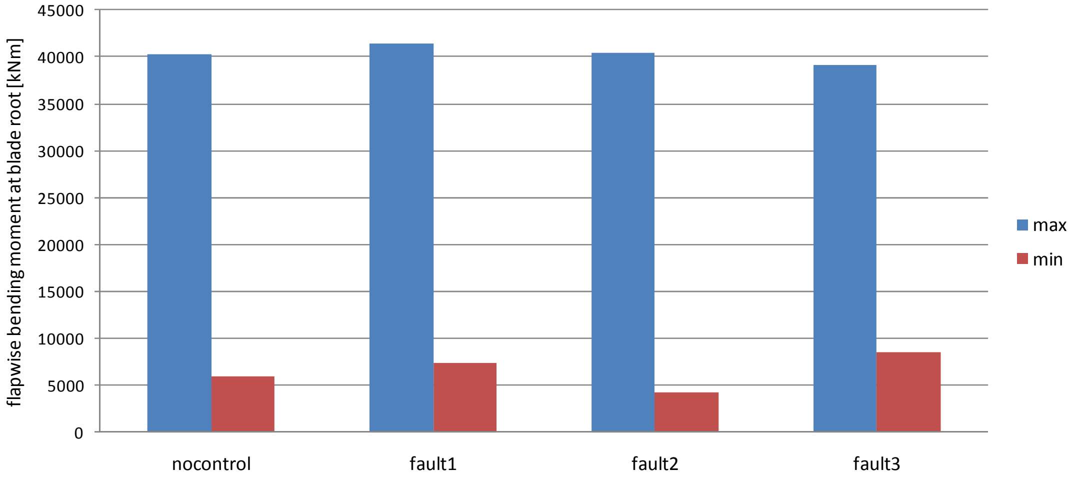

Figure 76: Min-max of flapwise bending moment at fault conditions. Wind speed 12m/s.

3.6 Results Idling Operation

A preliminary assessment of a control strategy for the reduction of fatigue and extreme loads due to parked (idling) operation is performed in the present section. When the wind turbine operates in idling mode the angles of attack seen by the blades vary significantly over the revolution as a result of the turbulence of the wind, the tilt of the nacelle, the inclination of the incoming inflow. The aoa variation significantly increases when the rotor operates even with a small yaw misalignment. It is noted that yaw misalignments of +/-15^o are considered as normal idling conditions for wind turbine manufactures. Even at moderate yaw angles aoa variations can be such that the rotor enters stall both at the positive and negative aoa regimes and thereby stall induced vibrations can occur.

A control system based on the reading of the local flow incidence by means of a pitot tube (eg. at 75% radial position) can deploy the flap whenever the rotor approaches post stall conditions and switch to a different C_L polar with a lower C_{Lmax} value, higher stall angle and a smoother post stall behaviour (lower post stall ΔC_L).

In the present implementation of the control scheme, as shown in **Figure 77**, the flap moves upwards from $\beta f=+10^o$ to $\beta f=-10^o$ when the aoa exceeds the angle that C_L becomes 0.9 (on the $\beta f=+10^o$ steady curve) and moves downwards from $\beta f=-10^o$ to $\beta f=+10^o$ when the aoa becomes lower than the angle that C_L becomes -0.5 (on the $\beta f=-10^o$ steady curve). Ramp type change of the flap angle is applied within 2 s.

The flap configuration considered in the present study was that of CONF3 (short flap extending to 30% of the chord).

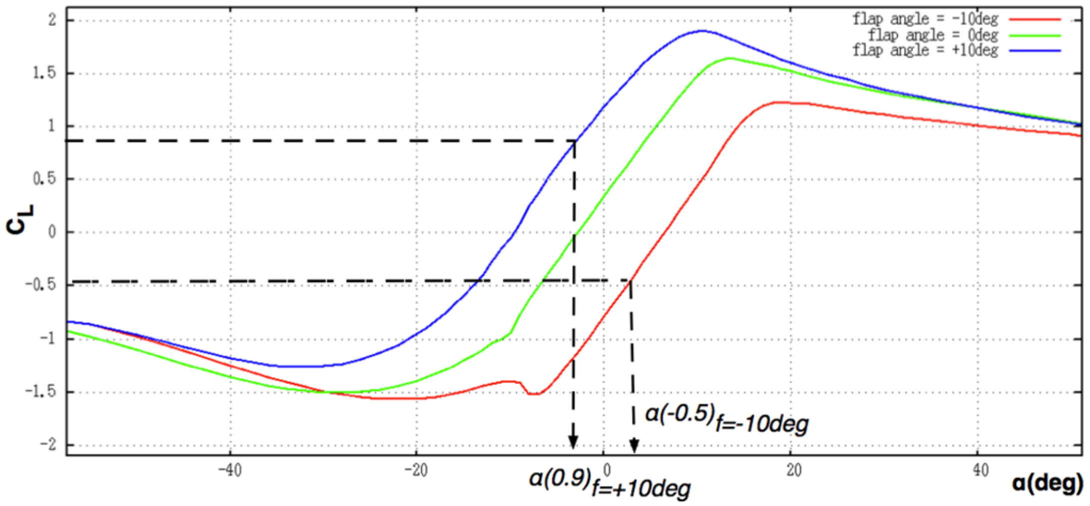

Figure 77: Control scheme for standstill load alleviation.

The time series of the flapwise and the edgewise bending moments of the controlled and the uncontrolled cases are shown in **Figure 78** and **Figure 79** for the wind speed of 42.5 m/s and a yaw misalignment of 15°. A significant reduction of the min/max loads as well as the fatigue loads is noted on both moments. The equivalent load reduction is of the order of 25% on the flapwise moment and 12% on the edgewise moment. The reduction of the peak load is of the order of 35% on the flapwise moment and 25% on the edgewise moment.

Figure 80 presents the C_L-α loops for the controlled and the uncontrolled cases. It is seen that if no control takes place the blade goes into the post stall region at the positive angles of attack regime. On the other hand in the controlled case the blades always operate in the linear C_L regime at positive aoa.

In **Figure 81** it is seen that the flap control has a minor effect on the idling speed.

Figure 78: Time series of the flapwise bending moment at the blade root at standstill. Wind speed 42.5m/s, yaw 15°.

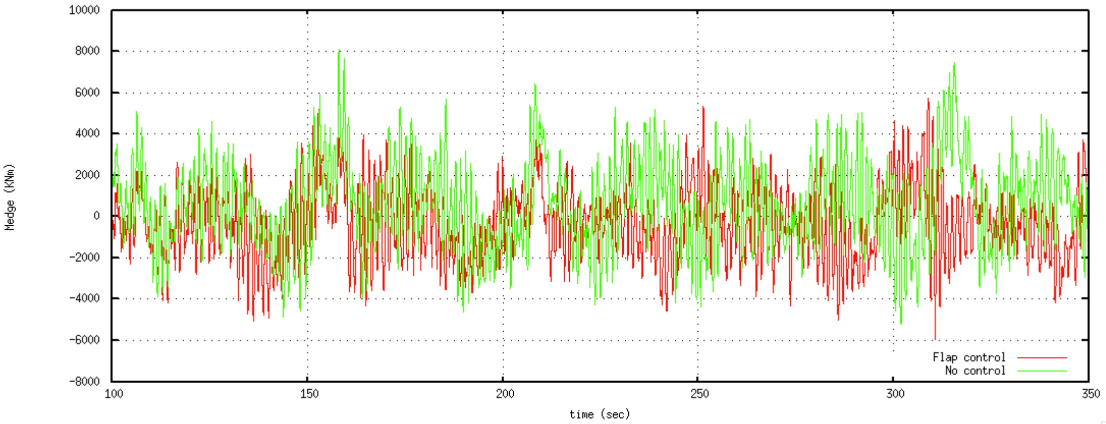

Figure 79: Time series of the edgewise bending moment at the blade root at standstill. Wind speed 42.5m/s, yaw 15⁰.

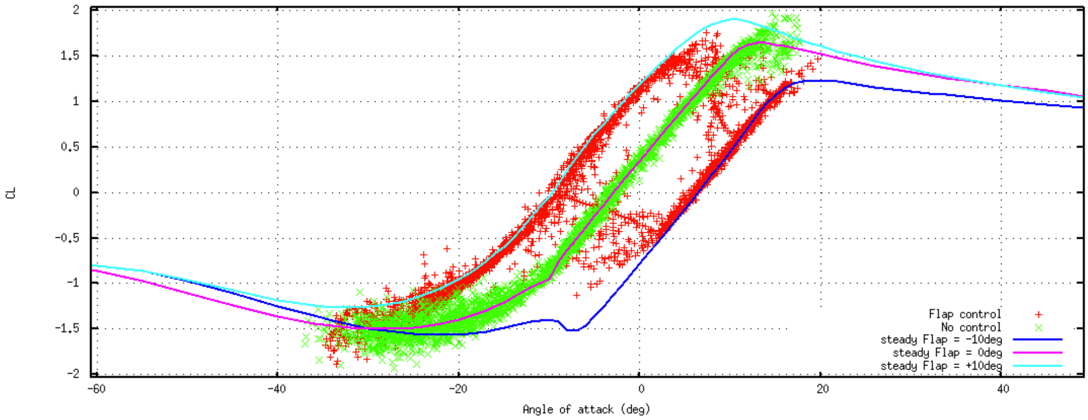

Figure 80: CL-α loop. Wind speed 42.5m/s, yaw 15⁰.

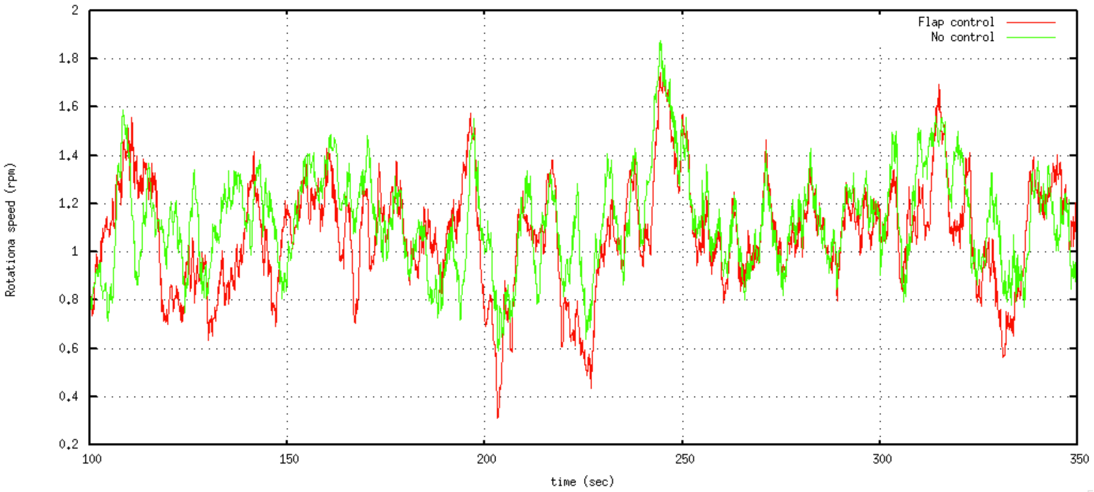

Figure 81: Time series of the idling speed. Wind speed 42.5m/s, yaw 15⁰.

3.7 Conclusions

The assessment of different TE flap geometries and control schemes has been performed for various operational conditions including normal operation, idling operation and occurrence of faults. Both fatigue and extreme loads are considered in the analysis.

A noticeable reduction of the blade fatigue loads is obtained for all flap configurations tested ranging from 10% to 18%. This is not accompanied by a reduction of the tower loads. Predominant fore-aft tower bending moment was slightly increased for cyclic flap control while it is marginally decreased when individual flap control was applied.

An overall increase of the extreme flapwise moment was obtained for cyclic flap (due to the slow response of the controller at higher wind speeds) while individual flap control slightly decreases ultimate loads.

The effect on extreme loads due to malfunctioning/failure of the flap control system was found to be minor.

A control scheme for the reduction of the extreme loads at idling operation conditions was proposed and tested. A preliminary assessment of the abovementioned control approach indicated a significant potential for reducing both flapwise and edgewise blade moments.

3.8 References

[1] Bottasso, C.L., Croce,A., Gualdoni, F., Montinari,P., Kloepfer,J., Riziotis,V.A. Voutsinas,S.G., Karakalas, A., Saravanos, D., Pavese, C., Rasmussen, F., Jan-Willem van Wingerden, “New concepts to control the load along the span of the blade, passive, active or mixed”, Innwind.EU project deliverable D 2.3.1

[2] Manolas D.I., Riziotis, V.A., Voutsinas, S.G, (2015) “Assessing the importance of geometric non-linear effects in the prediction of wind turbine blade loads”, Computational and Nonlinear Dynamics Journal, Vol. 10, 041008, July 2015.

[3] IEC. IEC 61400-1. Wind turbines – Part 1: Design Requirements, 2005.

[4] Bak, C. et al Description of the DTU 10 MW Reference Wind Turbine, Technical report, DTU Vindenergi-I-0092, 2013.

[5] Riziotis, V.A., Voutsinas, S.G. (2008) “Dynamic stall modeling on airfoils based on strong viscous-inviscid interaction coupling,” J. Numerical Methods in Fluids, 2008, 56, pp 185-208.

[6] Bergami, L., Riziotis, V.A., Gaunaa, M., (2014) “Aerodynamic response of an airfoil section undergoing pitch motion and trailing edge flap deflection: a comparison of simulation methods”, published online in Wind Energy Journal 2014.

4 VALIDATION 3: ENGINEERING MODEL SIMULATIONS WITH COMBINED ACTIVE FLAP AND INDIVIDUAL PITCH CONTROL, EXTENSIONS FOR ADAPTIVITY (TUD)

4.1 Introduction

The morphing trailing edge flap is implemented in an engineering model of Innwind 10 MW reference turbine, and its control authority with respect to the reduction of wind turbine lifetime dynamic loads is explored.

The simultaneous use of individual pitch control and active flap control is investigated in this section, with a focus on evaluating the trade-offs involved in load reduction potential and control actuator effort. Further, a new algorithm is proposed that can increase the adaptivity of the turbine towards uncertain dynamics and environmental conditions.

The simulation environment used is GH Bladed™, a commercial software developed by DNV GL, used widely in the industry for the load assessment and certification of wind turbines. The turbine model and the simulation environment are discussed in further detail in the next section.

4.1.1 Turbine Model and Simulation Environment

The turbine with the flap is modelled in GH Bladed™, version 4.4. This is a commercial software that has been validated with experimental data and used for evaluating the performance of turbines with trailing edge flap actuators [3]. The software represents the turbine in a multi-body framework, with flexible tower, blades and drive train. The comparison of the structural realisation of the reference turbine model in Bladed and in HAWC2 [1] is shown via the comparison of turbine eigenmodes in Table 14.

Table 14: Comparison of turbine modes

Comparison of Turbine Modes; HAWC2 v/s Bladed		
Mode Description	**HAWC2**	**Bladed**
1st Tower Fore-Aft Mode	0.249425 Hz	0.254 Hz
1st Tower Side-Side Mode	0.252219 Hz	0.256 Hz
1st Drive Train Torsional Mode	0.510692 Hz	N/A
1st Blade Flapwise Mode	0.601467 Hz	0.612 Hz
1st Blade Edgewise Mode	0.949380 Hz	0.946 Hz
2nd Blade Flapwise Mode	1.591313 Hz	1.739 Hz
2nd Tower Fore-Aft Mode	2.025250 Hz	3.188 Hz

Bladed is also capable of simulating the aeroelastic interaction of the turbine with trailing edge flaps with a full 3D turbulent wind field that can be generated using TurbSim, for instance. The aeroelastic interaction is modelled using the Blade Element Momentum theory [4], which has further corrections for tip effects and three-dimensional flow.

The location of the trailing edge flap can be indicated in Bladed by its spanwise position along the blade. Further, Bladed requires as an input the change in the aerodynamic lift, drag and moment curves caused by a change in trailing edge flap deployment angle. This information is obtained from the 2D lift/drag/moment polars obtained from the work of NTUA in the previous chapter.
It is to be noted that Bladed does not consider the effect of unsteady aerodynamics. The assumption made here is that the reduced frequency is too low for unsteady aerodynamics to dominate. Further, the actuator dynamics can be defined by the user, and it is expected that the residual effect of unsteady aerodynamics can be captured by modifying the actuator dynamics suitably. In this case, the actuator dynamics are considered to be first order with a time constant of 0.1.

The reference turbine described here is implemented in Bladed in closed loop with a controller compiled in the Matlab-Simulink environment, as described next.

4.1.2 Design Load Cases

In order to evaluate the efficiency of the controllers that will be investigated in the sequel, a sampling of design load cases is collated from the IEC-61400 Wind Turbine Design standard [5]. The design load cases cover both fatigue loads and extreme loads. The focus in this chapter will be on the evaluation of controller behavior in normal power production runs, which are typically the largest contributors to wind turbine fatigue. Six different turbulent realisations are considered for each wind speed, and the main features of the normal power production load case are given in Table 3.

To explore the effect on the overall reliability, fault cases related to flaps were also investigated to understand the response of the turbine to flap malfunctions. These test cases are described in Table 4.

For all cases, the following turbine loads are tracked to understand the attenuation or enhancement of turbine loading caused by different control strategies:

1. Tower My and Mx: Tower bottom fore-aft and side-side bending moments respectively.
2. Nacelle x and y: Nacelle fore-aft and side-side vibrations respectively.
3. Blade My and Mx: Blade out-of-plane and in-plane bending moments respectively.
4. Power: Generated electrical power.
5. Speed: Generator speed.
6. Pitch activity: Pitch travel and pitch rate.
7. Flap activity: Flap rate.

4.1.3 Turbine Controller Design

The description of the baseline turbine [1] also includes a description of the baseline controller. Fundamentally, this consists of two major parts: the torque controller that is active below the rated wind speed, and the collective pitch controller that is active above the rated wind speed. The torque controller uses generator speed measurements to regulate the generator power for maximising energy capture. On the other hand, the collective pitch controller manipulates the turbine pitch angle to limit the aerodynamic power captured above the rated wind speed, and thereby maintain stable constant power operation. Further, nacelle accelerations are also measured to implement a controller that adds damping to various structural modes.

The baseline controller is not capable of reducing the periodic loads on the turbine blades and other components that occur at frequencies of 1P (rotor speed), and its harmonics: 2P, 3P, and so on. These loads arise out of wind shear, tower shadow effects and the rotational sampling of turbulence and form a dominant component of the turbine load spectrum. As described in [6], these loads can be alleviated by pitching the three blades individually, a schema also known as Individual Pitch Control (IPC). The conventional implementation of individual pitch control is shown in Figure 82.

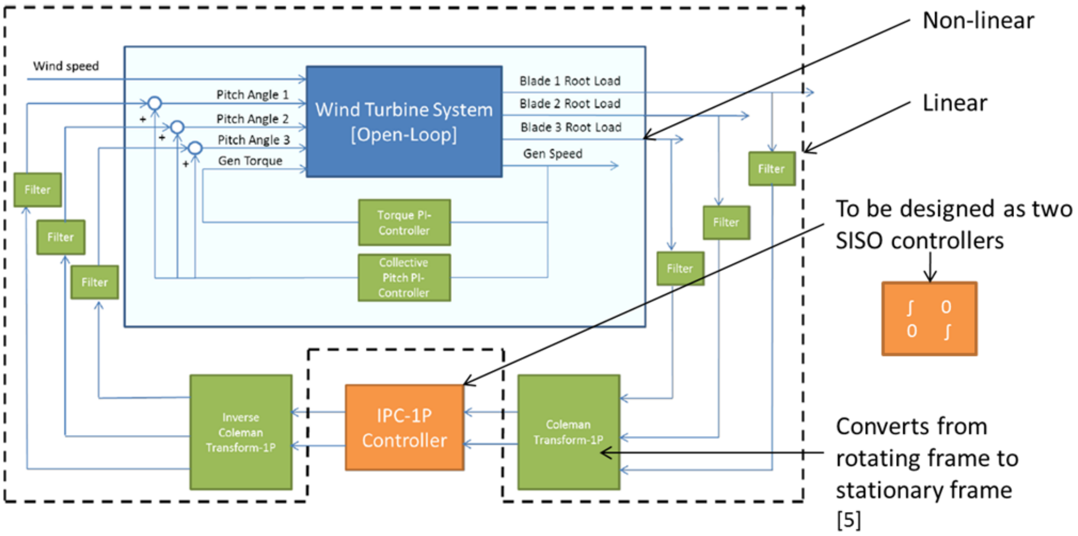

Figure 82: Individual Pitch Control [5]

Fundamentally, the objective of the IPC controller is to minimise the measured blade root bending moments by issuing the correct individual pitch commands to the three blades. However, since the transfer from blade pitch angle to blade root load is non-linear, the “Coleman transform” is used to linearise the transfer and to be able to design a linear controller in the new domain. This transform decomposes the three measured rotating blade loads into two orthogonal loads in the fixed frame of reference, which may be physically interpreted as the yaw and tilt loads on the hub of the turbine. Depending on the load peak to be attenuated (i.e., 1P, 2P and so on), the corresponding Coleman transform is used, which shifts the load peak to a simple DC offset that can be reduced using a simple diagonal integral controller, as shown in the figure. This controller is designed using PI tuning rules, and the generated pitch control actions are shifted back into the rotating frame of reference using the corresponding inverse Coleman transform. The Coleman transforms are shown in Figure 83.

The IPC controller is not active below the rated wind speed, in order to limit pitch activity.

Coleman transform:

$$\begin{bmatrix} L_{tilt} \\ L_{yaw} \end{bmatrix}_{1P} = \frac{2}{3} \begin{bmatrix} \cos\phi & \cos\left(\phi + \frac{2\pi}{3}\right) & \cos\left(\phi + \frac{4\pi}{3}\right) \\ \sin\phi & \sin\left(\phi + \frac{2\pi}{3}\right) & \sin\left(\phi + \frac{4\pi}{3}\right) \end{bmatrix} \begin{bmatrix} L_1 \\ L_2 \\ L_3 \end{bmatrix}$$

Inverse Coleman transform:

$$\begin{bmatrix} \theta_1 \\ \theta_2 \\ \theta_3 \end{bmatrix} = \begin{bmatrix} \cos\phi' & \sin\phi' \\ \cos\left(\phi' + \frac{2\pi}{3}\right) & \sin\left(\phi' + \frac{2\pi}{3}\right) \\ \cos\left(\phi' + \frac{4\pi}{3}\right) & \sin\left(\phi' + \frac{4\pi}{3}\right) \end{bmatrix} \begin{bmatrix} \theta_{tilt} \\ \theta_{yaw} \end{bmatrix}_{1P}$$

Figure 83: Coleman transforms

The IPC controller is designed following the methodology shown above. The controller parameters are given in

Table 15. The pitch rate is constrained to remain within 10 °/s.

Table 15: IPC Controller Parameters

Controller Parameters – 1P	Value
Prefilter Frequency/Damping Ratio	1P/0.5
Integrator gain	0.004
Lead Angle	45°
Controller Parameters – 2P	**Value**
Prefilter Frequency/Damping Ratio	2P/0.5
Integrator gain	0.02
Lead Angle	24°

Individual Flap Control (IFC) is the use of the trailing edge flaps to reduce the peaks 1P, 2P and so on, using flap activity to replace the pitch control of IPC. The basic implementation of IFC follows the same controller logic as IPC, described in Figure 82. Essentially, as in IPC, the blade root bending moments measured from the three blades are transformed to two load signals in the stationary frame of reference. These signals are fed to an IFC controller, which is typically also a diagonalised integral controller, and the commanded control inputs are then inverse-transformed and used to actuate the three trailing-edge flaps located on each blade. The IFC controller operates both below and above the rated wind speed in order to maximise the load reduction possible.

The IFC output is saturated to the maximum and minimum possible flap deployment angle, +/- 10° in this case. Also, the flap rate is physically constrained to remain within 100 °/s, an order of magnitude higher than the pitch rate, taking into account the significantly lower inertia associated with flap action. Pitch actuator dynamics and unsteady aerodynamics are modelled as a first order system with time constant 0.1.

Like the IPC controller, the PI gains for the IFC controller are tuned by linearising the model around different operating points, and loop-shaping the controller behaviour for the desired closed-loop behaviour of minimal fluctuations in the blade root loads. The parameters of the designed IFC controller are shown in Table 16.

For the case where both the IFC and IPC controllers are active, the parameters are left unaltered. Both the controllers described above are allowed to run in parallel and attempt to minimise the blade root loads simultaneously by commanding two different sets of actuators.

Table 16: IFC Controller Parameters

Controller Parameters – 1P	Value
Prefilter Frequency/Damping Ratio	1P/0.5
Integrator gain	0.1
Lead Angle	0°
Controller Parameters – 2P	**Value**
Prefilter Frequency/Damping Ratio	2P/0.5
Integrator gain	0.5
Lead Angle	6°

4.1.3 Results

The reference turbine was simulated in Bladed, using different combinations of the IPC and IFC controllers in order to determine the load attenuation effect of the controllers. Four different control cases are compared in the following results:

- Baseline control without IPC or IFC controllers
- Baseline control with IPC controller active
- Baseline control with IFC controller active
- Baseline control with both IPC and IFC controllers active.

In this section, the fatigue and extreme values of different load signals will be compared for all four cases, and for each DLC. The fatigue and extreme loads for the baseline case at 12 m/s are shown in Table 17 and Table 18.

Table 17: Baseline Lifetime Fatigue Loads

Measurement	Life time equivalent load	Wöhler Exponent M
Tower Bottom Fore-Aft Bending Moment	$1.135\text{x}10^5$ kNm	4
Tower Bottom Side-Side Bending Moment	$3.244\text{x}10^4$ kNm	4
Nacelle Fore-Aft Displacement	0.4576 m	4
Nacelle Side-Side Displacement	0.1224 m	4
Blade Root Out-of-plane Bending Moment	$2.649\text{x}10^4$ kNm	10
Blade Root In-plane Bending Moment	$8.775\text{x}10^3$ kNm	10
Pitch Angle	0.1773°	1
Flap Angle	0°	1

Table 18: Baseline Extreme Loads

Measurement	Minimum	Maximum	Case for minimum	Case for maximum
Tower Bottom Fore-Aft Bending Moment	$-1.005\text{x}10^5$ kNm	$2.873\text{x}10^5$ kNm	24 m/s, Seed 2	12 m/s, Seed 2
Tower Bottom Side-Side Bending Moment	$-9.192\text{x}10^4$ kNm	$1.462\text{x}10^5$ kNm	24 m/s, Seed 4	24 m/s, Seed 4
Nacelle Fore-Aft Displacement	-0.3735 m	1.16 m	24 m/s, Seed 2	12 m/s, Seed 2
Nacelle Side-Side Displacement	-0.6017 m	0.3099 m	24 m/s, Seed 4	24 m/s, Seed 4
Blade Root Out-of-plane Bending Moment	$-2.011\text{x}10^4$ kNm	$5.131\text{x}10^4$ kNm	24 m/s, Seed 1	12 m/s, Seed 1
Blade Root In-plane Bending Moment	$-1.902\text{x}10^4$ kNm	$2.424\text{x}10^4$ kNm	24 m/s, Seed 5	24 m/s, Seed 5

The fatigue and extreme loads for the case where only the Individual Pitch Controller is active, are shown in

Table 19 and Table 20.

Table 19: Fatigue Loads with IPC Control only

Measurement	Life time equivalent load	Wöhler Exponent M
Tower Bottom Fore-Aft Bending Moment	1.128x10^5 kNm	4
Tower Bottom Side-Side Bending Moment	3.273x10^4 kNm	4
Nacelle Fore-Aft Displacement	0.4433 m	4
Nacelle Side-Side Displacement	0.1234 m	4
Blade Root Out-of-plane Bending Moment	2.562x10^4 kNm	10
Blade Root In-plane Bending Moment	8.979x10^3 kNm	10
Pitch Angle	0.5689 °	1
Flap Angle	0 °	1

Table 20: Extreme Loads with IPC Control only

Measurement	Minimum	Maximum	Case for minimum	Case for maximum
Tower Bottom Fore-Aft Bending Moment	-1.081x10^5 kNm	2.680x10^5 kNm	24 m/s, Seed 2	12 m/s, Seed 2
Tower Bottom Side-Side Bending Moment	-1.009x10^5 kNm	1.429x10^5 kNm	24 m/s, Seed 3	24 m/s, Seed 4
Nacelle Fore-Aft Displacement	-0.4358 m	1.061 m	24 m/s, Seed 2	12 m/s, Seed 5
Nacelle Side-Side Displacement	-0.5853 m	0.3471 m	24 m/s, Seed 4	24 m/s, Seed 3
Blade Root Out-of-plane Bending Moment	-1.786x10^4 kNm	5.042x10^4 kNm	24 m/s, Seed 6	12 m/s, Seed 6
Blade Root In-plane Bending Moment	-1.918x10^4 kNm	2.617x10^4 kNm	24 m/s, Seed 5	24 m/s, Seed 5

The fatigue and extreme loads for the case where only the Individual Flap Controller is active, are shown in Table 21 and
Table 22.

Table 21: Fatigue Loads with IFC Control only

Measurement	Life time equivalent load	Wöhler Exponent M
Tower Bottom Fore-Aft Bending Moment	1.187x10^5 kNm	4
Tower Bottom Side-Side Bending Moment	3.370x10^4 kNm	4
Nacelle Fore-Aft Displacement	0.4587 m	4
Nacelle Side-Side Displacement	0.1254 m	4
Blade Root Out-of-plane Bending Moment	2.481x10^4 kNm	10
Blade Root In-plane Bending Moment	8.775x10^3 kNm	10

Pitch Angle	0.2566°	1
Flap Angle	3.785°	1

Table 22: Extreme loads with IFC Control only

Measurement	Minimum	Maximum	Case for minimum	Case for maximum
Tower Bottom Fore-Aft Bending Moment	-1.027×10^{5} kNm	2.839×10^{5} kNm	24 m/s, Seed 2	12 m/s, Seed 2
Tower Bottom Side-Side Bending Moment	-1.006×10^{5} kNm	1.491×10^{5} kNm	24 m/s, Seed 4	24 m/s, Seed 4
Nacelle Fore-Aft Displacement	-0.3997 m	1.136 m	24 m/s, Seed 2	12 m/s, Seed 2
Nacelle Side-Side Displacement	-0.6052 m	0.3290 m	24 m/s, Seed 4	24 m/s, Seed 4
Blade Root Out-of-plane Bending Moment	-1.723×10^{4} kNm	5.055×10^{4} kNm	24 m/s, Seed 2	12 m/s, Seed 1
Blade Root In-plane Bending Moment	-1.978×10^{4} kNm	2.551×10^{4} kNm	24 m/s, Seed 5	24 m/s, Seed 5

Finally, the fatigue and extreme loads for the case where both the IPC and the IFC controllers are active, are shown in Table 23 and Table 24.

Table 23: Fatigue Loads with IPC and IFC Control

Measurement	Life time equivalent load	Wöhler Exponent M
Tower Bottom Fore-Aft Bending Moment	1.187×10^{5} kNm	4
Tower Bottom Side-Side Bending Moment	3.314×10^{4} kNm	4
Nacelle Fore-Aft Displacement	0.4683 m	4
Nacelle Side-Side Displacement	0.1248 m	4
Blade Root Out-of-plane Bending Moment	2.407×10^{4} kNm	10
Blade Root In-plane Bending Moment	8.775×10^{3} kNm	10
Pitch Angle	0.4756°	1
Flap Angle	2.917°	1

Table 24: Extreme Loads with IPC and IFC Control

Measurement	Minimum	Maximum	Case for minimum	Case for maximum
Tower Bottom Fore-Aft Bending Moment	-1.011×10^{5} kNm	2.869×10^{5} kNm	24 m/s, Seed 2	12 m/s, Seed 2
Tower Bottom Side-Side Bending Moment	-1.027×10^{5} kNm	1.460×10^{5} kNm	24 m/s, Seed 4	24 m/s, Seed 4
Nacelle Fore-Aft Displacement	-0.4105 m	1.151 m	24 m/s, Seed 2	12 m/s, Seed 1
Nacelle Side-Side Displacement	-0.5939 m	0.3459 m	24 m/s, Seed 4	24 m/s, Seed 3
Blade Root Out-of-plane Bending Moment	-1.873×10^{4} kNm	5.131×10^{4} kNm	24 m/s, Seed 6	12 m/s, Seed 1

Blade Root In-plane Bending Moment	-2.002x10⁴ kNm	2.684x10⁴ kNm	24 m/s, Seed 5	24 m/s, Seed 5

For the case of pure flap control, and combined IFC and IPC control, the blade root loads and the control activity can be seen in Figure 84, Figure 85 and Figure 86.

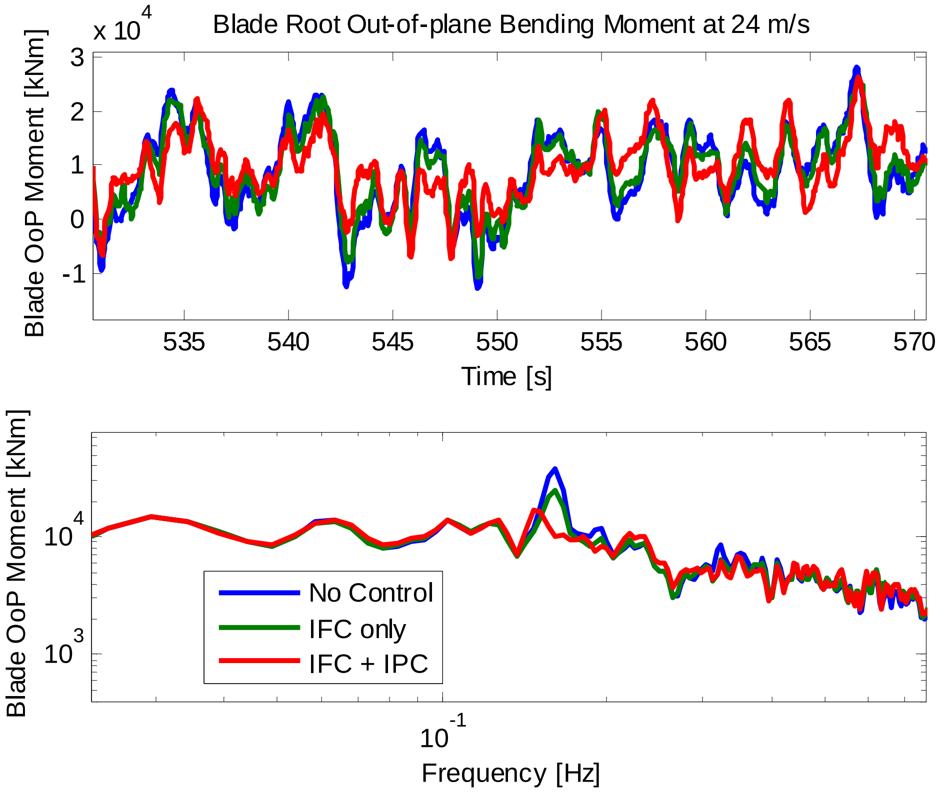

Figure 84: Blade Root Loads at 24 m/s

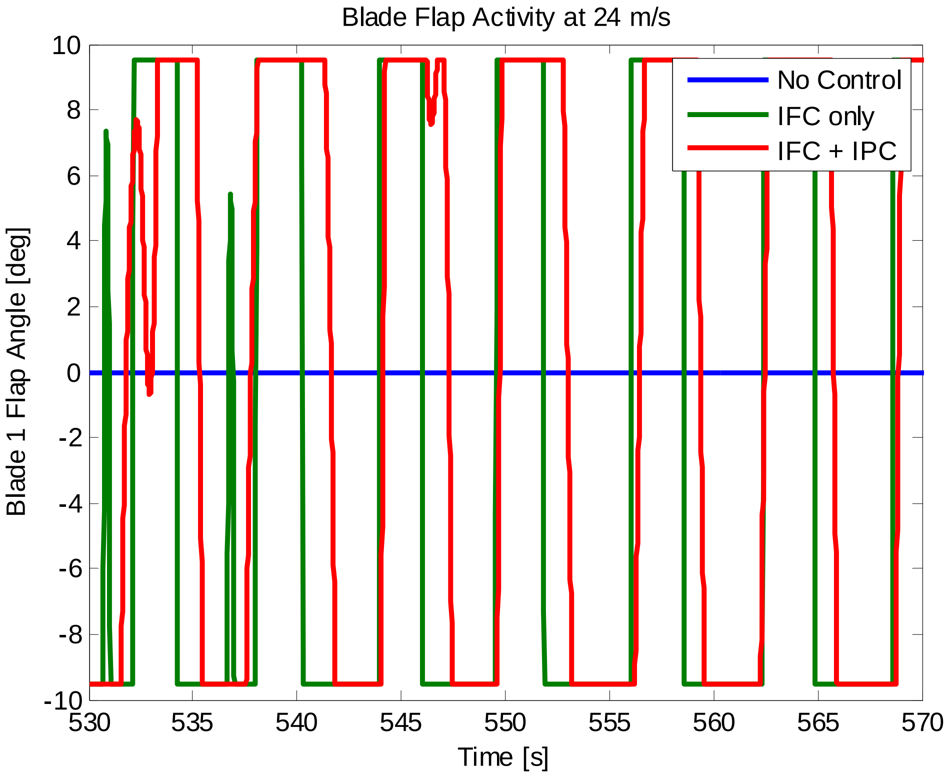

Figure 85: Blade Flap Activity at 24 m/s

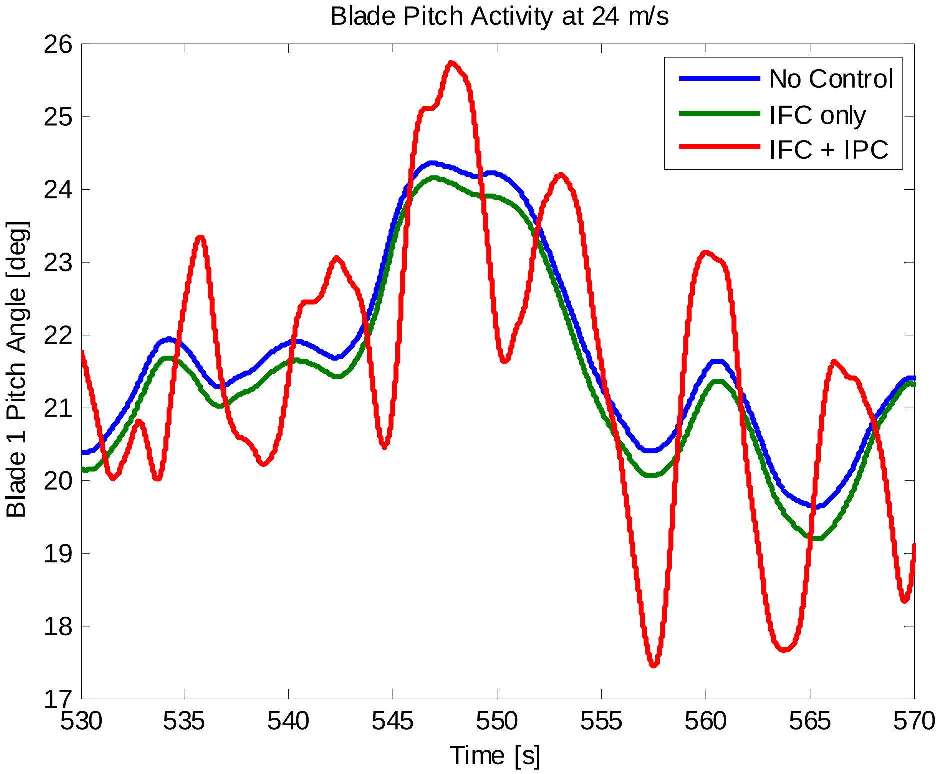

Figure 86: Blade Pitch Activity at 24 m/s

All lifetime fatigue loads are compared in Figure 87, while the extreme maximum loads are compared in Figure 88, and the extreme minimum loads are compared in Figure 89.

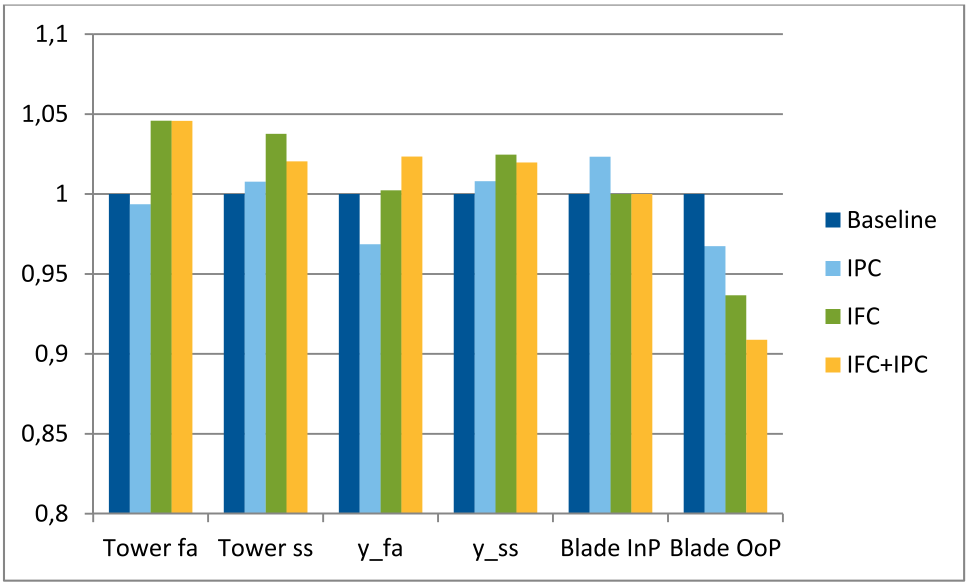

Figure 87: Comparison of normalised fatigue loads for different controllers

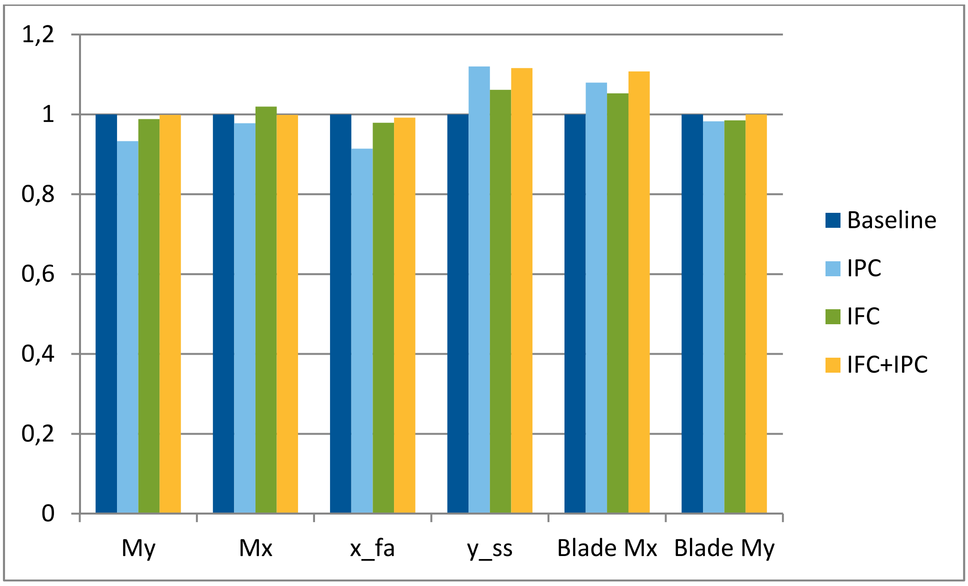

Figure 88: Comparison of normalised extreme maximum loads for different controllers

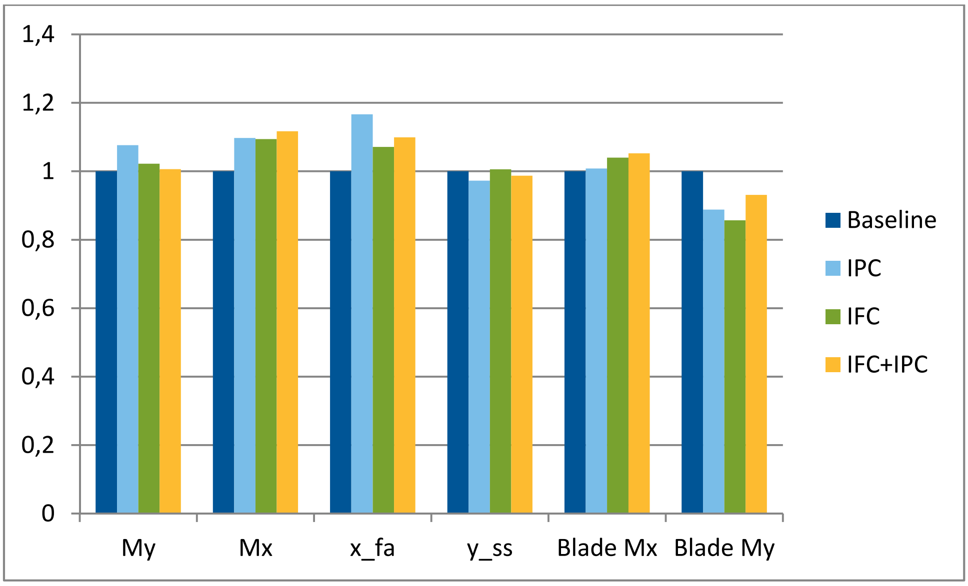

Figure 89: Comparison of normalised extreme minimum loads for different controllers

As compared to the case with the larger flap size, as considered in Chapter 7, the focus here is on maintaining pitch activity and tower loads to within acceptable limits. Accordingly, the controllers used are less aggressive and the load reductions are more moderate. The IPC controller shows load reductions of 3.5%, with the IFC controller showing load reductions of 6.5%. The combined controller shows increased load reduction of 9.8%. The IPC controller increases pitch activity by a factor of 3, while the IFC controller only causes a pitch activity increase by 45%. The combined IPC-IFC controller shows an increase in pitch activity by a factor of 2.5. The flap controller leads to an increase in tower loads, and a smaller increase in nacelle motion. The pitch controller reduces fore-aft loads, but leads to a slight increase in tower side-side loads and blade in-plane loads.

The controllers tested also have a beneficial effect on blade out-of-plane extreme loads, with an upto 10% reduction in the extreme minimum blade loads. The controllers also increase the minimum tower loads and reduce the maximum tower loads, since the overall effect of the IPC and IFC controllers is to reduce the mean tower load.
The averaged statistics over the different load cases are shown in Table 25. The normalised changes in the loads are shown in Table 26. A negative sign indicates a reduction in the loads.

Table 25: Comparison of averaged statistics

	Blade Root Out-of-plane Bending Moment Min [kNm]	Blade Root Out-of-plane Bending Moment Max [kNm]	Blade Root Out-of-plane Bending Moment Std [kNm]	Tower Bottom Fore-Aft Bending Moment Min [kNm]	Tower Bottom Fore-Aft Bending Moment Max [kNm]	Tower Bottom Fore-Aft Bending Moment Std [kNm]	Pitch Angle Std [deg]	Flap Angle Std [deg]
baseline	-7.502x10^3	3.753x10^4	6.856x10^3	-2.037x10^4	2.227x10^5	4.038x10^4	2.4434	0.0000
IPC	-6.057x10^3	3.752x10^4	6.491x10^3	-1.977x10^4	2.194x10^5	3.941x10^4	2.6163	0.0000
IFC	-5.847x10^3	3.661x10^4	6.336x10^3	-2.341x10^4	2.194x10^5	4.035x10^4	2.4325	9.1560
IPC+IFC	-4.992x10^3	3.676x10^4	6.271x10^3	-2.559x10^4	2.202x10^5	4.071x10^4	2.6364	8.3026

Table 26: Normalised change in loads compared to baseline [%]

	Blade Root Out-of-plane	Blade Root Out-of-plane	Blade Root Out-of-plane	Tower Bottom Fore-Aft	Tower Bottom Fore-Aft	Tower Bottom Fore-Aft	Pitch Angle Std [%]	Flap Angle Std [%]

	Bending Moment Min [%]	Bending Moment Max [%]	Bending Moment Std [%]	Bending Moment Min [%]	Bending Moment Max [%]	Bending Moment Std [%]		
IPC	-19.26	-0.0266	-5.324	-2.946	-1.482	-2.402	7.076	-
IFC	-22.06	-2.4514	-7.585	14.92	-1.482	-0.074	-0.446	-
IPC+IFC	-33.46	-2.0517	-8.533	25.63	-1.123	0.8172	7.899	-9.321

The above tables show that the IPC controller keeps the increase in pitch activity moderate, while still achieving load reductions. The IFC controller is able to achieve the same objective by replacing pitch activity by flap activity. With both controllers used simultaneously, the blade load reduction is increased, while reducing the demands on the flap actuation.

The blade load reductions at different wind speeds are shown in Figure 90. It can be seen that moderate reductions in loads are observed at all wind speeds, with the largest reductions observed when both the IPC and IFC controllers are active. Similarly, Figure 91 shows the pitch activity in all load cases. It can be seen that the IPC controller requires significantly more pitch activity than the IFC and baseline control cases (which have virtually identical pitch activity requirements). On the other hand, the combined IPC and IFC controller requires moderately increased pitch activity, lower than that required by the IPC-only controller. Finally, Figure 92 compares the flap activity for the case with only IFC control and the case with IPC + IFC control. It can be seen that for the most part, the flap activity is similar. This is due to the reduced spanwise size of the flap, which requires full flap deflection in all cases to maximise load reduction.

None of the load control concepts show any influence on power production.

Next, the DLC 1.2 fault cases are simulated, as described in Table 4. For the symmetric fault case, the blade extreme loads increase by 3-4%. On the other hand, for the asymmetric fault case, the blade extreme loads increase by 14-17%.

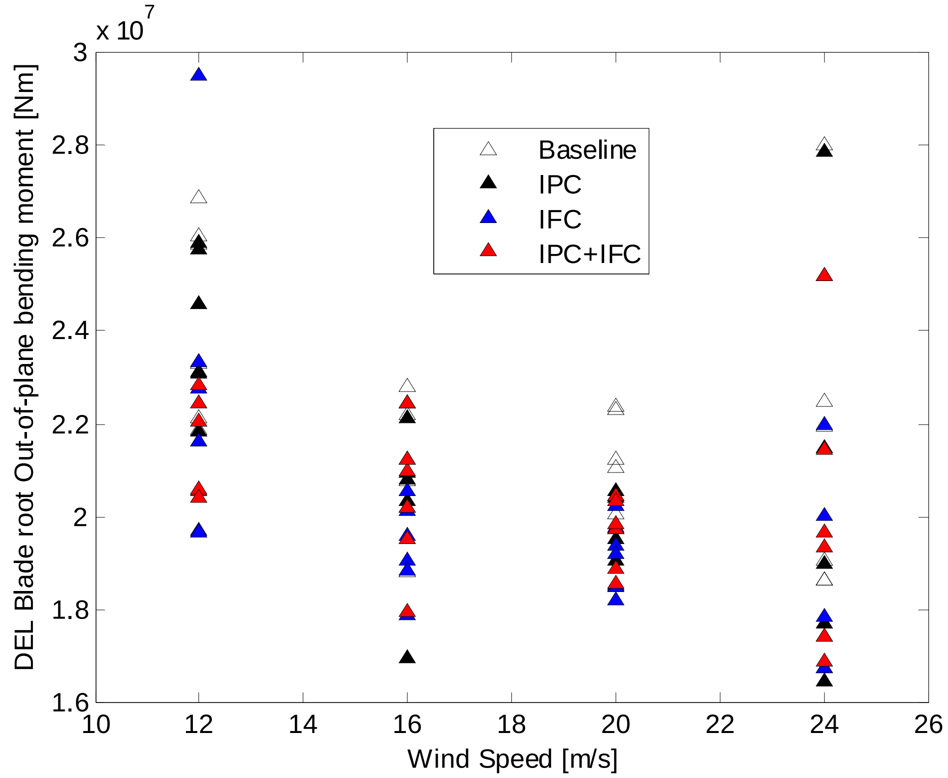

Figure 90: Comparison of Blade Load DELs for all load cases

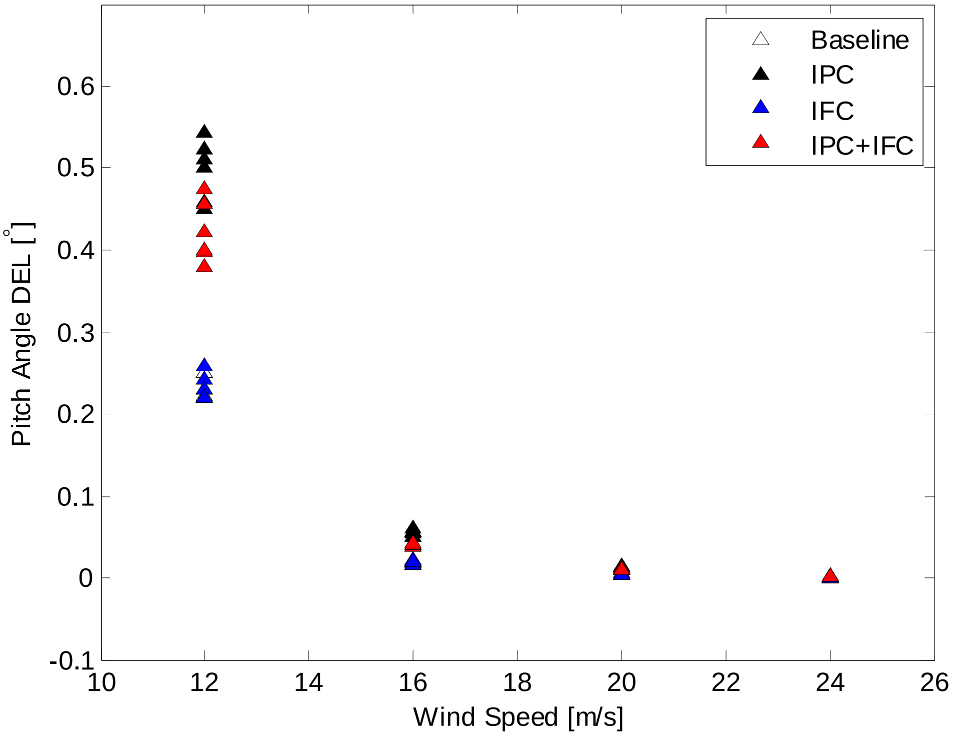

Figure 91: Comparison of Pitch Activity for all load cases

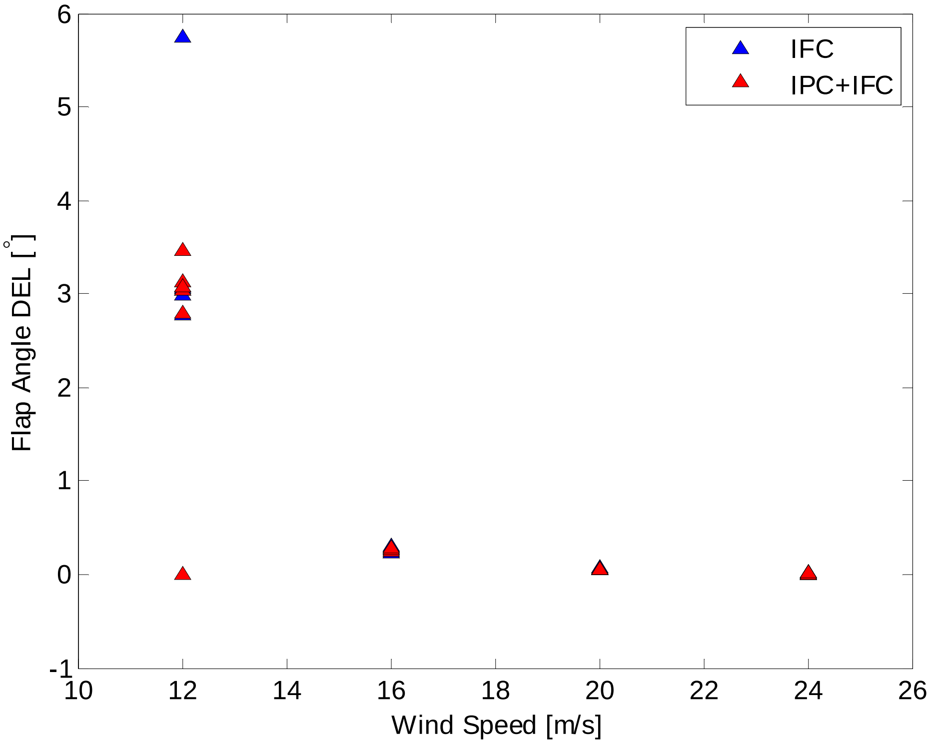

Figure 92: Comparison of Flap Activity for all load cases

4.2 Frequency Separation of Pitch and Flap Control

4.2.1 Introduction and Control Architecture

From the previous section, it is clear that a combined control strategy that includes both pitch and flap control shows better load reduction characteristics with moderate control effort, as compared to pitch-only and flap-only controllers. In the previous section, the flap and pitch controllers were designed independently for maximum load reduction, and were then implemented simultaneously to explore their interaction. However, one can expect better load control performance when the two controllers are tailored to maximally exploit their individual advantages and limitations.

While pitch control has high control authority, this is limited to the low frequency region of the load spectrum: pitch controller bandwidth is limited by the large inertia of the three blades about their pitch axes. It is therefore preferable to use the pitch controller to target low frequency load peaks, such as the 1P peak.

On the other hand, trailing edge flap mechanisms can respond fast to a control input, but they are limited to small angular deflections leading to limited control authority. As such, it may be preferable to use the flap controller to target the low amplitude high frequency peaks in the blade load spectrum.

As such, this sections explores the design of a controller where the IPC controller targets only the 1P peak in the blade load spectrum, while the IFC controller targets only the 2P peak in the blade load spectrum, thereby separating the frequency ranges of the two load controllers.

The control architecture is identical to the one explained in Figure 82. The primary difference is that the 1P Coleman and inverse-Coleman transformations are used for the IPC controller, while for the IFC controller, the 2P Coleman and inverse-Coleman transformations are used. The results of implementing this frequency-separated IPC-IFC controller are discussed in the next section.

4.2.2 Results

In this section, the frequency-separated IPC-IFC controller, as described above, is implemented on the same reference turbine model described in Chapter 1, using GH Bladed. In this case, for understanding the behaviour of the controllers, simulations are done at an above-rated wind speed of 19 m/s, with 0% turbulence. Three test cases are discussed below:

- Baseline control without IPC or IFC controllers
- Baseline control with both independently designed IPC and IFC controllers
- Baseline control with frequency-separated IPC and IFC controllers active.

The load reduction achieved and the control effort demanded for all three controller cases will be hereinunder discussed. The blade load reductions achieved can be seen in Figure 93. It can be seen that in both cases, load reductions are achieved. The frequency-separated controller behaves slightly better in that loads are reduced to an extent 2% better than the independently designed controller, as it avoids IPC and IFC controller interaction.

Similarly, Figure 94 shows the reduction in tower bottom loads. It can be clearly seen that the mean tower load is reduced by both controllers, with the frequency separated controller showing slightly better performance. Finally, Figure 95 shows that the cyclic loading of the yaw bearing reduces significantly with frequency-separated IPC and IFC control.

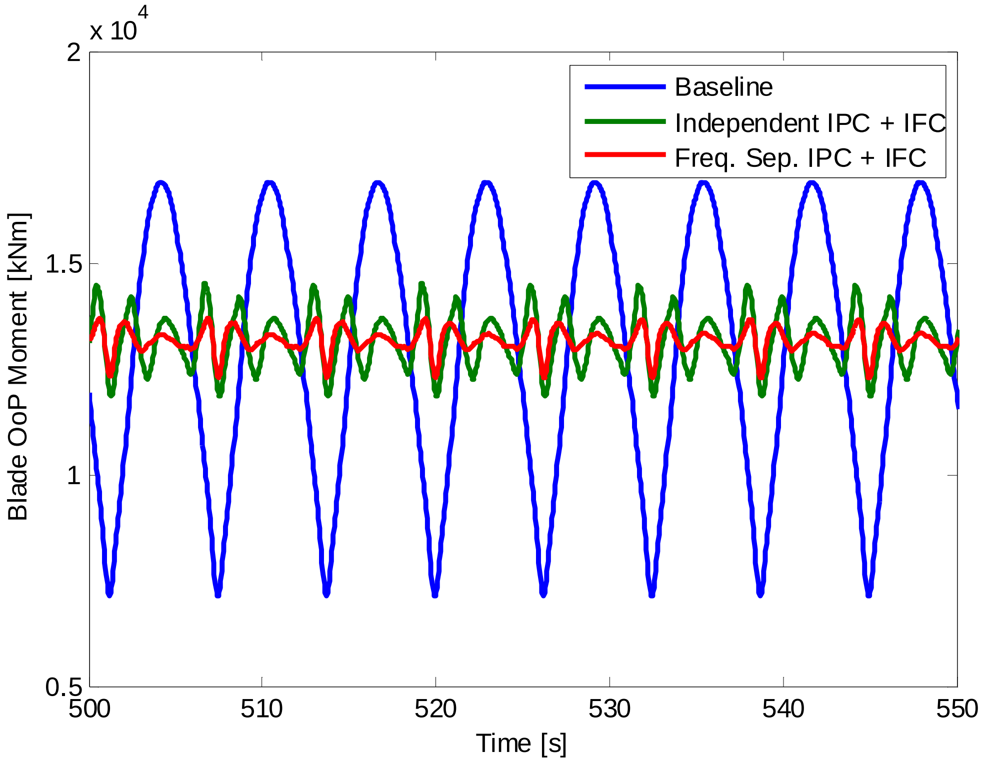

Figure 93: Blade Root Load Reduction, Wind Speed 19 m/s

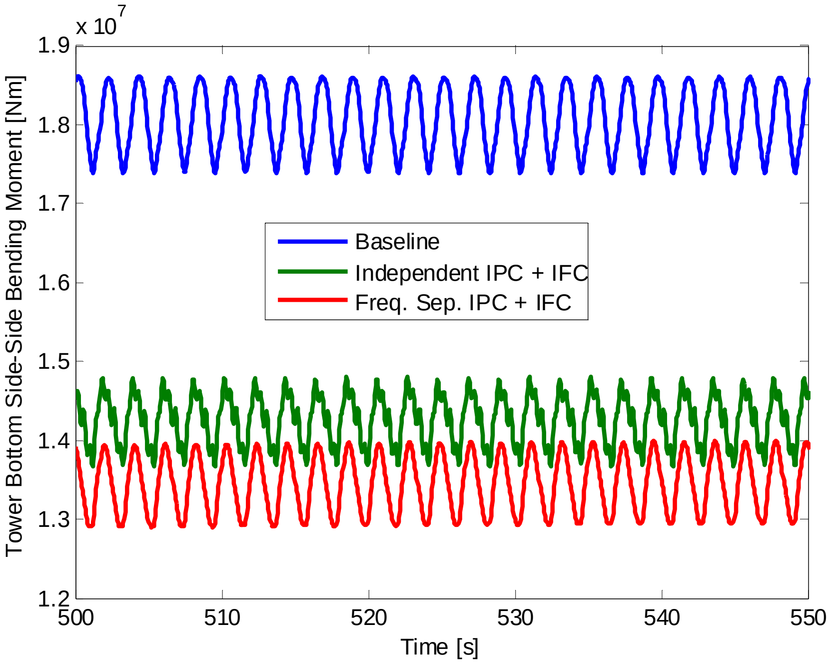

Figure 94: Tower Bottom Load Reduction, Wind Speed 19 m/s

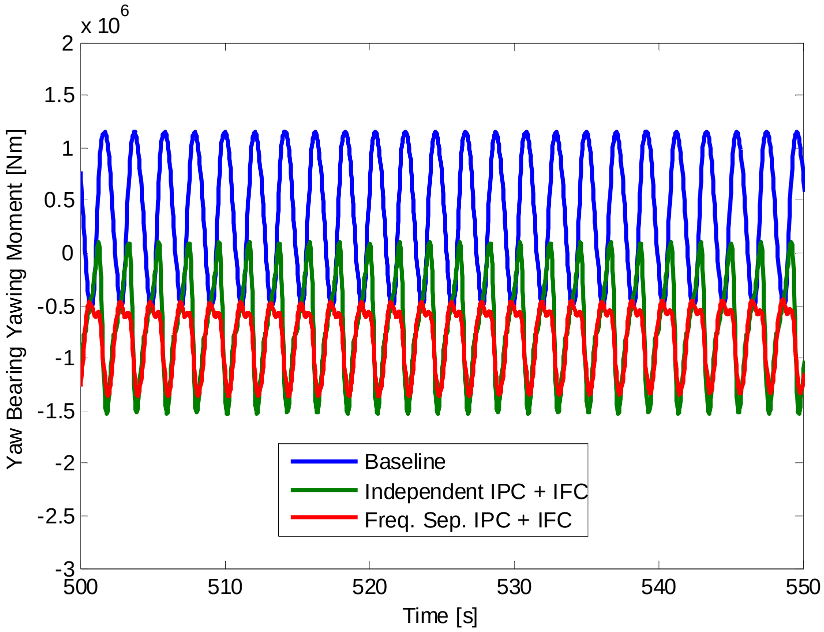

Figure 95: Yaw Bearing Load Reduction, Wind Speed 19 m/s

The change in the control effort required when moving to frequency-separated IPC-IFC control is shown in the next few figures. As can be seen in Figure 96, the frequency-separated controller demands slightly higher pitch activity, but only at low frequencies. Apart from 1P (and a small amount of 3P), there is no other frequency content in the pitch rate spectrum, which is beneficial for the pitch bearing life.

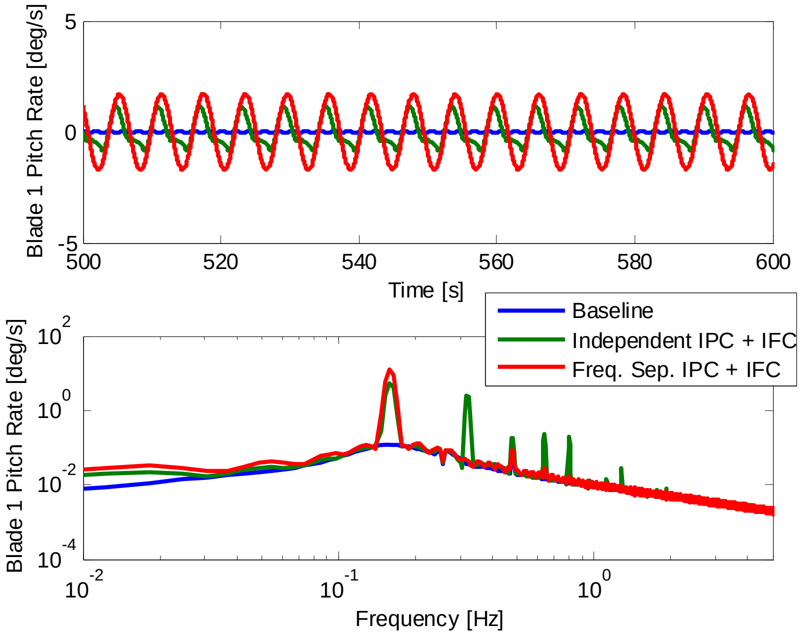

Figure 96: Blade Pitch Rate, Wind Speed 19 m/s

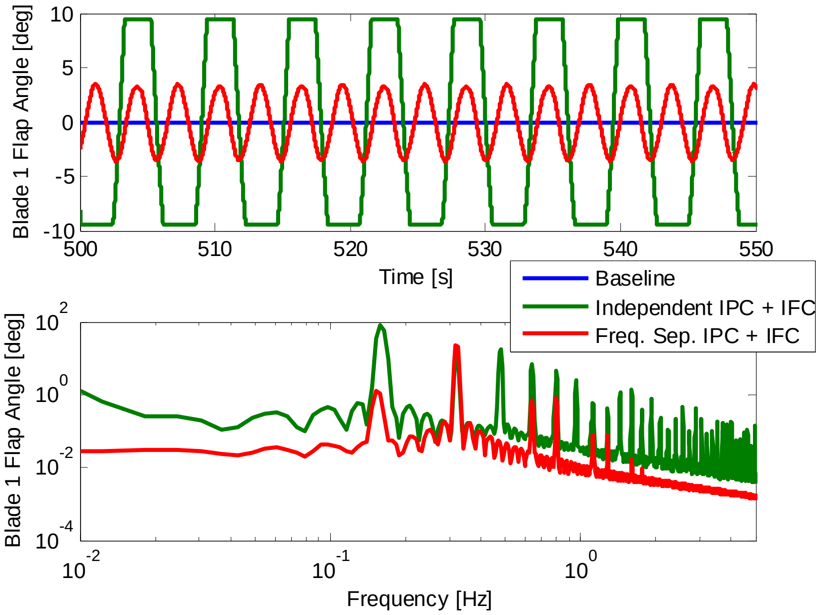

Figure 97: Flap Angle, Wind Speed 19 m/s

Finally, in Figure 97, the flap actuation demand for all three cases can be seen in the time and frequency domain. It can be immediately appreciated that the amplitude of the flap actuation signal is significantly reduced, such that it no longer hits the saturation limits. IFC in the frequency-separated case focusses primarily on 2P load reduction, while also adding limited control effort at higher frequencies. Thus, within the low control authority limits afforded by the physical flap actuator, the frequency-separated IFC controller is still able to perform efficient high-frequency load reduction.

From this section, it can be concluded that frequency-separated combined IPC and IFC control is able to compensate for the limitations of both controllers, and is an interesting field for further research.

4.3 Subspace Predictive Repetitive Control for IFC

One of the drawbacks of the IFC control design technique as delineated above, is that it is necessary to have an approximate model of the wind turbine system to be able to ensure that the designed controller will be stable and near-optimal in the closed loop. However, wind turbines show significantly non-linear characteristics that vary not just with ambient wind conditions, but also from turbine to turbine depending on manufacturing discrepancies and site conditions. Further, the aerodynamic response of a flap may vary depending upon local flow characteristics as well as actuator aging.

Finally, as has been seen before, a wind turbine load controller is often expected to suppress discrete peaks in the wind turbine spectrum, so for optimal control effort expenditure it would be desirable to be able to control precisely the frequency content in the control signal to be concentrated at 1P, 2P, as required.

For these reasons, the new methodology of Subspace Predictive Repetitive Control (SPRC) for IFC has been developed and explained in [7]. In this method, the first step involves the identification of the wind turbine system using input-output data . In the second step, the identified system parameters are directly used to synthesise an optimal load reduction controller, and the corresponding control input is used to command the flap actuators. Finally, the optimum control input is constrained to a basis function subspace so that the control action occurs at exactly the desired frequency.

A short theoretical background of the method will be given next, followed by the results of the implementation on the GH Bladed turbine.

4.3.1 Theoretical Basis for SPRC

4.3.1.1. System Description

Initially, as in conventional predictive control methodologies, it is required to be able to predict the load signal over the future horizon. As such, an innovation-type state-space formulation is assumed for the wind turbine system:

$$\begin{aligned} x_{k+1} &= Ax_k + Bu_k + Ed_k + Ke_k \\ y_k &= Cx_k + Fd_k + e_k, \end{aligned}$$

which has the following predictor form:

$$\begin{aligned} x_{k+1} &= \tilde{A}x_k + Bu_k + \tilde{E}d_k + Ky_k \\ y_k &= Cx_k + Fd_k + e_k. \end{aligned}$$

Here, $x_k \in \mathbb{R}^n$ is the state vector of unknown dimension, $u_k \in \mathbb{R}^3$ are the three blade flap angles, and $y_k \in \mathbb{R}^3$ are the three blade load signals used for feedback. The wind disturbance on each blade to be suppressed is taken to be periodic with period P, and is denoted here by $d_k \in \mathbb{R}^3$, while $e_k \in \mathbb{R}^3$ is the aperiodic component of wind disturbance. The objective of the controller is to minimise the periodic component of loading as this is the dominant blade design driver. Finally, the matrices $A, B, C, E, F, K, \tilde{A}, \tilde{E}$ are unknown system matrices of the appropriate dimensions. In order to avoid estimating the disturbance dynamics, the difference operator δ is defined such that

$$\delta u_k = u_k - u_{k-P}, \qquad \delta y_k = y_k - y_{k-P}, \qquad \delta d_k = 0.$$

Such that the dynamics of the wind turbine system can be rewritten as

$$\begin{aligned} \delta x_{k+1} &= \tilde{A}\delta x_k + B\delta u_k + K\delta y_k \\ \delta y_k &= C\delta x_k + \delta e_k. \end{aligned}$$

4.3.1.2. Lifted System Description

The objective of the controller is to minimised the loads over the entire future horizon, i.e. over a large number of periods into the future. Hence, as done in predictive control, the system described above is lifted, in this case, over the period of rotation P of the turbine, which forms the smallest possible size of the prediction horizon. The input vector stacked over this horizon is given by

$$\delta U_k^{(P)} = \begin{bmatrix} u_k - u_{k-P} \\ u_{k+1} - u_{k+1-P} \\ \vdots \\ u_{k+P-1} - u_{k-1} \end{bmatrix},$$

with the stacked output vector given in the same way. The unknown lifted system matrices are described below. The extended controllability matrix is given as:

$$\mathcal{K}^{(P)} = [\tilde{A}^{P-1}B \quad \tilde{A}^{P-2}B \quad \cdots \quad B \quad \tilde{A}^{P-1}K \quad \tilde{A}^{P-2}K \quad \cdots \quad K].$$

The Toeplitz matrix of the system is described as:

$$\widetilde{H}^{(P)} = \begin{bmatrix} 0 & 0 & 0 & 0 \\ CB & 0 & 0 & 0 \\ \vdots & \vdots & \ddots & 0 \\ C\tilde{A}^{P-2}B & C\tilde{A}^{P-3}B & \cdots & 0 \end{bmatrix},$$

with a similar definition for the innovation form Toeplitz $H^{(P)}$, where $\tilde{A}$ is replaced by A, and for the Toeplitz matrices $\tilde{G}^{(P)}$ and $G^{(P)}$, where the matrix B is replaced by K. Finally, the innovation and predictor form extended controllability matrices are given as:

$$\tilde{\Gamma}^{(P)} = \begin{bmatrix} C \\ C\tilde{A} \\ \vdots \\ C\tilde{A}^{P-1} \end{bmatrix}, \qquad \Gamma^{(\mathrm{P})} = \begin{bmatrix} C \\ CA \\ \vdots \\ CA^{P-1} \end{bmatrix}.$$

The system description using the stacked input-output vectors is then given as:

$$\begin{aligned} \delta x_{k+P} &= \tilde{A}^P \delta x_k + \mathcal{K}^{(P)} \begin{bmatrix} \delta U_k^{(P)} \\ \delta Y_k^{(P)} \end{bmatrix} \\ \delta y_{k+P} &= C\delta x_{k+P} + \delta e_{k+P}. \end{aligned}$$

4.3.1.3. Predictor Formulation

With this lifted system, it is possible to predict the value of the output over a future horizon. At this point, the assumption is made that $\tilde{A}^P \approx 0$, which is true for a reasonably large value of P, for a K gain that stabilises $\tilde{A}$. Hence, the state and output predictions are given, from the last equation, as

$$\delta x_{k+P} \approx \mathcal{K}^{(P)} \begin{bmatrix} \delta U_k^{(P)} \\ \delta Y_k^{(P)} \end{bmatrix}$$

$$\delta y_{k+P} = C\mathcal{K}^{(P)} \begin{bmatrix} \delta U_k^{(P)} \\ \delta Y_k^{(P)} \end{bmatrix} + \delta e_{k+P}.$$

The output prediction over a future horizon equal to one period, is given as

$$\delta Y_{k+P}^{(P)} = \tilde{\Gamma}^{(P)}\mathcal{K}^{(P)} \begin{bmatrix} \delta U_k^{(P)} \\ \delta Y_k^{(P)} \end{bmatrix} + \begin{bmatrix} \tilde{H}^{(P)} & \tilde{G}^{(P)} \end{bmatrix} \begin{bmatrix} \delta U_{k+P}^{(P)} \\ \delta Y_{k+P}^{(P)} \end{bmatrix}.$$

Here, the prediction of δe_{k+P} over the horizon is identically taken to be zero, as no further knowledge is assumed available of this disturbance sequence. Rearranging the above equation, the output predictor is given by:

$$\delta Y_{k+P}^{(P)} = \Gamma^{(P)}\mathcal{K}^{(P)} \begin{bmatrix} \delta U_k^{(P)} \\ \delta Y_k^{(P)} \end{bmatrix} + H^{(P)} \delta U_{k+P}^{(P)}.$$

4.3.1.4. System Identification

The output equation for a single time step from the previous section is repeated here:

$$\delta y_{k+P} = C\mathcal{K}^{(P)} \begin{bmatrix} \delta U_k^{(P)} \\ \delta Y_k^{(P)} \end{bmatrix} + \delta e_{k+P}.$$

It is to be noted that in this relation, the terms $C\mathcal{K}^{(P)}$ are functions of the system matrices and are hence unknown. On the other hand, as input-output data becomes available, the terms δy_{k+P} and $\begin{bmatrix} \delta U_k^{(P)} \\ \delta Y_k^{(P)} \end{bmatrix}$ can be measured at each time step $(k+P)$. As such, using a common estimation technique such as recursive least squares, it is possible to obtain an estimate of $C\mathcal{K}^{(P)}$ online at every time step. This estimate can now be used in the predictor equation above to formulate a control law.

4.3.1.5. Optimal Control Law

Based on the identified $C\mathcal{K}^{(P)}$ parameters, it is possible to build the $\Gamma^{(P)}\mathcal{K}^{(P)}$ and $H^{(P)}$ matrices in the predictor equation

$$\delta Y_{k+P}^{(P)} = \Gamma^{(P)}\mathcal{K}^{(P)} \begin{bmatrix} \delta U_k^{(P)} \\ \delta Y_k^{(P)} \end{bmatrix} + H^{(P)} \delta U_{k+P}^{(P)}.$$

Now, since the absolute value of the loads is to be penalised instead of the differenced value, the equation above is rewritten as:

$$Y_{k+P}^{(P)} = \begin{bmatrix} \Gamma^{(P)}\mathcal{K}^{(P)} & I \end{bmatrix} \begin{bmatrix} \begin{bmatrix} \delta U_k^{(P)} \\ \delta Y_k^{(P)} \end{bmatrix} \\ Y_k^{(P)} \end{bmatrix} + H^{(P)} \delta U_{k+P}^{(P)}.$$

The predicted loads over an infinite horizon are to be penalised, hence the cost function under consideration is given as:

$$J = \sum_{k=1}^{\infty} ||(Y_{k+P}^{(P)})^T Q Y_{k+P} + \left(\delta U_{k+P}^{(P)}\right)^T R \delta U_{k+P}^{(P)}||_2^2.$$

Since the system parameters in the predictor have been identified, this cost function can be optimised only, for instance, by solving the corresponding Riccati equations, to find the closed-loop feedback gain that maximises load reduction and yields a stable closed loop in the case where the identified system parameters are close to the exact parameters.

4.3.1.6. The Use of Basis Functions

It is desirable to focus on load reduction at specific frequencies in the blade load spectrum, primarily 1P and its harmonics. In this case, both the identification and control law formulation can be simplified by projecting the input and output into a lower-dimensional subspace. For instance, if the controller is to target only the 1P load in the spectrum, the projection matrix U_f is given by:

$$U_f = \begin{bmatrix} \sin\frac{2\pi}{P} & \sin\frac{4\pi}{P} & \cdots & \sin 2\pi \\ \cos\frac{2\pi}{P} & \cos\frac{4\pi}{P} & \cdots & \cos 2\pi \end{bmatrix}.$$

Then, the projected (stacked) input and output vectors are given by

$$\theta_k = U_f U_k^{(P)}, \qquad \bar{Y}_k = U_f Y_k^{(P)},$$

And the cost function to be minimised becomes

$$J = \sum_{k=1}^{\infty} ||(\bar{Y}_{k+P}^{(P)})^T Q \bar{Y}_{k+P} + \left(\delta\theta_{k+P}^{(P)}\right)^T R \delta\theta_{k+P}^{(P)}||_2^2.$$

With the use of basis functions, the control effort is directed only along the basis vector directions and when sinusoidal basis functions are used, precise control is achieved over the frequencies in the control input.

In the next section, the SPRC controller for IFC will be tested on the reference turbine in GH Bladed.

4.3.2 Results

In this section, the controller developed above will be tested and compared against the conventional IFC controller from Section 4.1. In total, three controller cases are considered:

- Baseline control without IPC or IFC controllers
- Baseline control with the conventional IFC controller from Section 4.1
- Baseline control with an SPRC-IFC controller designed above.

In order to understand the behaviour of the SPRC controller, an above-rated wind speed of 19 m/s will be considered, with 0% turbulence intensity.

In Figure 98, it can be seen that after an initial period of identification, the SPRC controller smoothly learns the optimal control input, and synthesises a controller signal that is very close to the manually designed conventional controller command, in phase and amplitude. It is to be noted that SPRC is able to reach this signal without any prior information about the wind turbine itself.

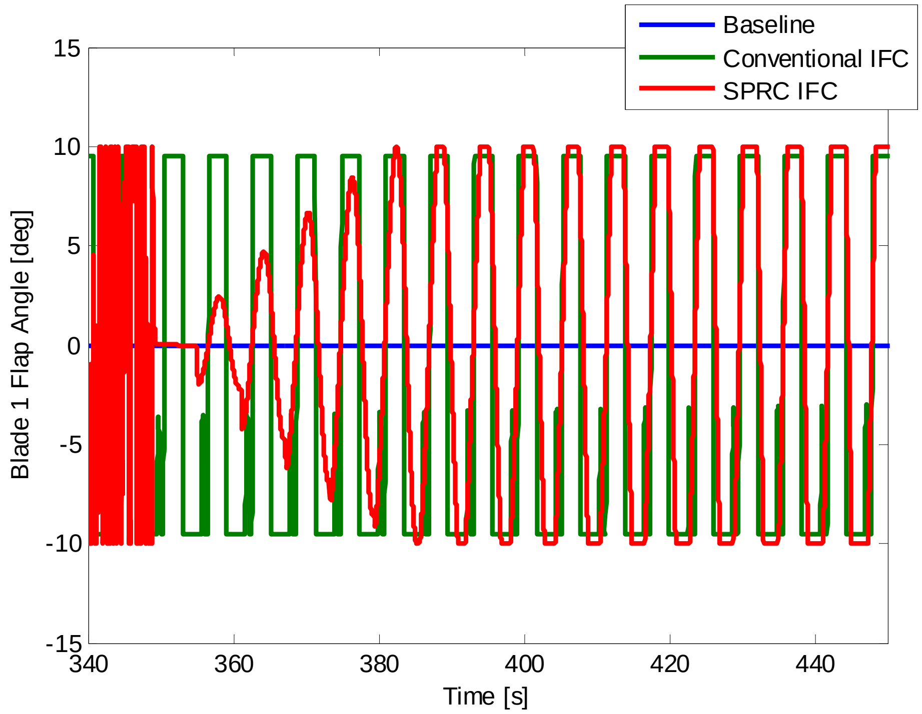

Figure 98: Flap Angle Command SPRC v/s Conventional

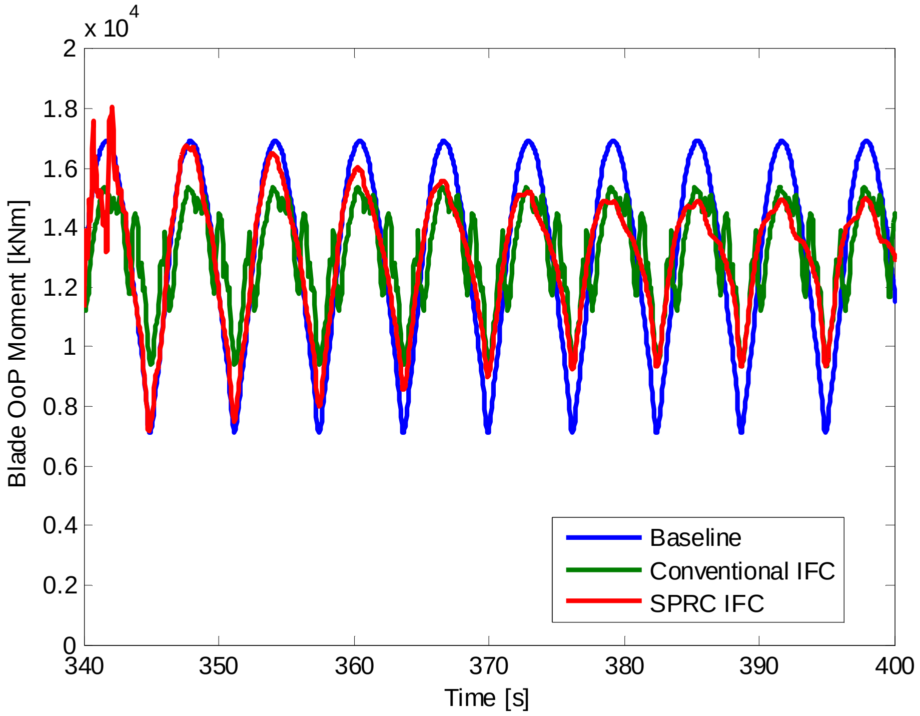

Figure 99: Blade Root Load Reduction SPRC v/s Conventional

Figure 99 shows the reduction in the blade root loads achieved by SPRC as compared to that with conventional IFC. It can be directly seen that after an initial learning phase, SPRC achieves the same load reductions as conventional IFC. Further, the loads have less high frequency content than the loads with conventional control, this is due to the strict control over frequency content achieved by using basis functions in SPRC.

Next, the response of the novel SPRC controller is validated in the case of an uncertain plant. For the validation, a phase uncertainty in the measured blade loads is simulated. An extreme case of 180° phase mismatch (sign uncertainty) is considered. The response of the SPRC controller is compared with that of the conventional IFC controller. The flap angle command after the learning phase of the SPRC controller can be seen in Figure 100. It can be seen that the flap angle command synthesised by SPRCis no longer in phase with that generated by conventional IFC.

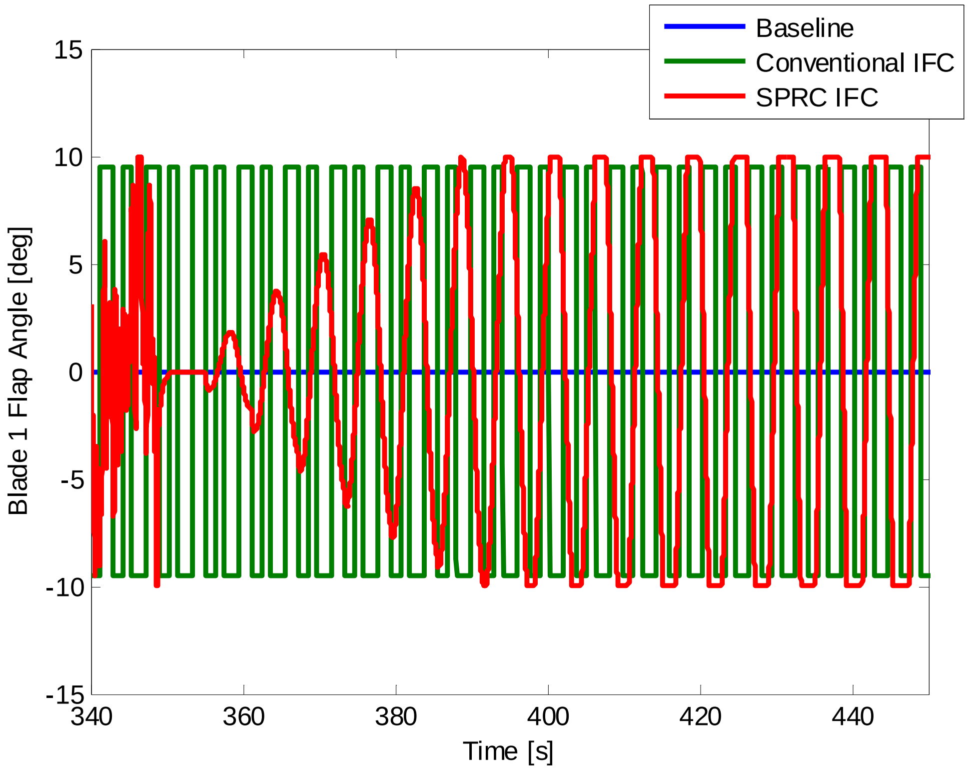

Figure 100: Flap Angle Command, Plant Mismatch Conventional IFC v/s SPRC

The load reductions achieved in the presence of plant-model mismatch can be seen in Figure 101. It can be directly seen that as a result of an uncertain plant, conventional IFC increases the loads instead of reducing them. On the other hand, since SPRC is able to identify the model, it is able to estimate the correct phase of the measurements, and it is also able to reduce loads to the same extent as in the previous case.

Thus, the advantage of using an adaptive algorithm for load reduction using trailing edge flaps is clearly demonstrated.

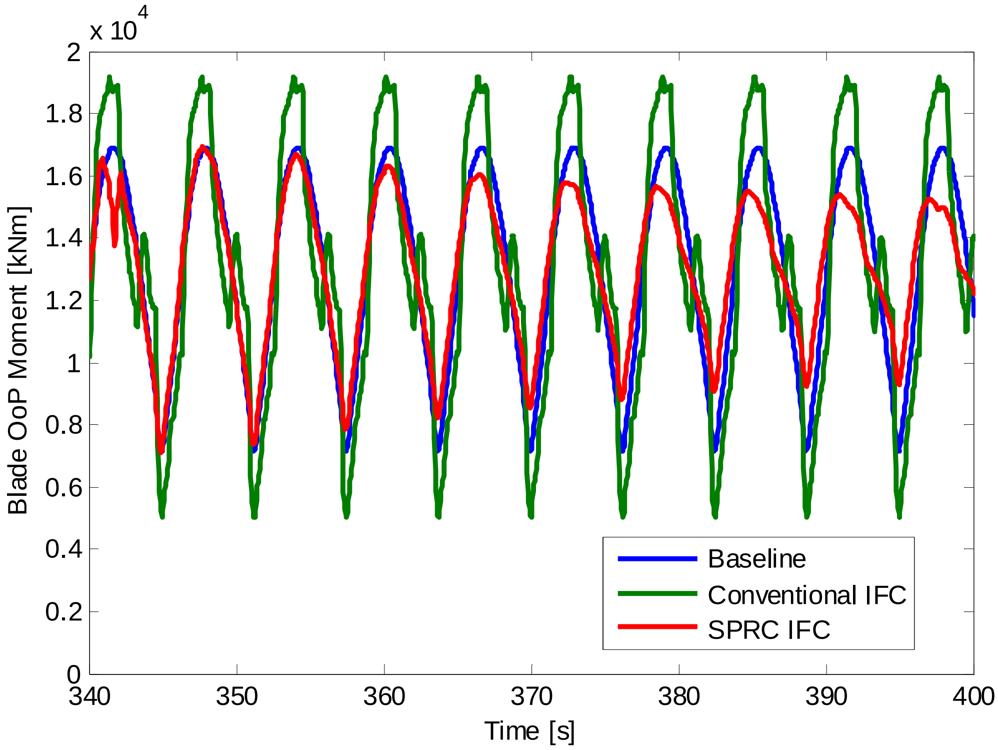

Figure 101: Blade root Load Reduction, Plant mismatch, Conventional IFC v/s SPRC

4.4 Conclusions

The trailing edge flap system was modelled in the software GH Bladed, and its effectivity in reducing turbine loads, especially alongside the pitch controller, has been explored. It was seen that with a relatively small spanwise length of 10%, the flap controller is able to achieve load reductions, especially at the blade root to the order of 6.5%. Combined with IPC, the load reductions can be increased to 10%, with a moderate increase in pitch activity as compared to the IPC-only controller. It is seen that typical extreme loads increase minimally with the addition of the flaps. The only case where extreme loads increase by upto 17% is the flap fault case where the three flaps saturate to asymmetric positions, causing an aerodynamic imbalance at the rotor.

Frequency-separation of the IPC and IFC controller was also tested, where IPC works only on the 1P loads, while IFC works on 2P and higher loads. It is seen that frequency content of the pitch actuator command reduces significantly, alleviating pitch bearing damage. On the other hand, in spite of its small spanwise size, the flap has adequate control authority to attenuate 2P and higher loads without hitting flap deployment angle limits.

Finally, the adaptive algorithm SPRC, for the model-free tuning of the flap controller was developed and tested. For no plant-model mismatch, it was shown to perform as well as the conventional IFC controller. On the other hand, with an extreme phase uncertainty of 180° in the feedback signal measurements, the conventional IFC controller showed an increase in blade loads, however, the SPRC controller was able to tune the flap actuator command to achieve the same load reductions as seen before. Hence, SPRC is shown as a promising candidate for an on-the-fly tuning of the flap controller for maximal load reduction.

Hereby, a combination of IPC and IFC controllers have been validated for load reduction on the reference turbine in the industrial GH Bladed™ simulation environment, with extensions for exploiting the unique features of both the pitch and flap actuators, and tuning the flap command adaptively in real-time.

4.5 References

[1] Bak, C. et al., Description of the DTU 10 MW Reference Turbine, Technical Report, DTU Vindenergi-I-0092, 2013.

[2] Bergami, L., Adaptive Trailing Edge Flaps for Active Load Alleviation in a Smart Rotor Configuration, PhD Thesis, DTU Wind Energy, 2013.

[3] Lackner, A. L. and Van Kuik, G. A. M., A Comparison of Wind Turbine Smart Rotor Control Approaches using Trailing Edge Flaps and Individual Pitch Control, Wind Energy 2010, 13:117-134.

[4] Manwell J. F., McGowan, J. G. and Rogers A. L., Wind Energy Explained: Theory, Design and Application. John Wiley and Sons Ltd., Chichester 2002.

[5] IEC 61400-1. Wind Turbines – Part 1: Design Requirements, 2005.

[6] Bossanyi, E. A., Further Load Reductions with Individual Pitch Control, Wind Energy, 8 (4):481-485.

[7] Navalkar, S. T., Van Wingerden, J. W., Van Solingen, E., Oomen, T. and Van Kuik, G. A. M., Subspace Predictive Repetitive Control for Wind Turbine Load Alleviation using Trailing Edge Flaps.

5 VALIDATION 4: DESIGN LOAD BASIS AEROELASTIC SIMULATIONS WITH INDIVIDUAL FLAP/PITCH CONTROL (DTU)

5.1 Aeroelastic load control simulations

The load alleviation potential of the Controllable Rubber Trailing Edge Flap (CRTEF) [1, 2] is verified on a reduced Design Load Base (DLB) setup using the aeroelastic code HAWC2, and by investigating a flap configuration for the DTU 10MW Reference Wind Turbine (RWT) model. The performance of the CRTEF configuration is first compared against the one obtained with individual pitch control; a third configuration is also investigated, where CRTEF and individual pitch controller are combined. The CRTEF allows for a significant reduction of the lifetime fatigue on various load channels; the reduction for some of the extreme loads is also noticeable.

5.2 Modelling Environment and Configuration

The DTU 10MW Reference Wind Turbine (RWT) [7] is used for the simulations in the aeroelastic code HAWC2 [8], as a representative modern multi-MW wind turbine model utilized in the INNWIND project. The simulated flap configuration is chosen based on prior studies [9], and the configuration for the INNWIND project (**Table 27**).

Table 27: Main flap parameters.

Flap configuration	
Chordwise extension	10%
Deflection angle limits	±10°
Spanwise length	25.9m (30% blade length)
Spanwise location	59.59m-85.50m (from blade root)
Airfoil	FFA-W3-241
Max ΔC_l	0.4
Deflection rate limit	100°/s
Actuator time constant	100ms

The unsteady aerodynamics associated with the active flaps is accounted for by using the ATEFlap dynamic stall model in HAWC2 [9, 10]. The variation of steady lift, drag, and moment coefficients introduced by the flap deflection in based on 2D CFD simulations performed with the code Ellipsys2D [11], for a Reynold's number of 6-12x10^6 for free transition with turbulence intensity 10%. Further, 3D corrections using Bak's models are applied. The geometry of the flap on the blade is shown in **Figure 102**. The flap structural dynamics are not accounted for in HAWC2, assuming a small flap and actuator size and weight, and not coupling with the rest of the blade structure. The actuator dynamics are implemented as a linear servo model in HAWC2, for a first order system with a time constant of 0.1s. This corresponds to the characteristics of a Controllable Rubber Trailing Edge Flap (CRTEF) actuator.

5.3 Post-processing and Sensors

The standard DTU Wind Energy Design Load Case post-processing method for the DLB has been utilized. The pre-processing tools are available in [5].This procedure and algorithms applied are described in detail in [6]. This includes the process of extraction of the defined load sensors statistics, the ultimate (extreme value) analysis including the prescribed safety factor, and the fatigue analysis. Representative load sensors on the main components of the wind turbine aeroelastic model are chosen, with the corresponding parameters for fatigue analysis shown in **Table 28**. The pitch bearing damage is also calculated, together with the pitch and flap activity.

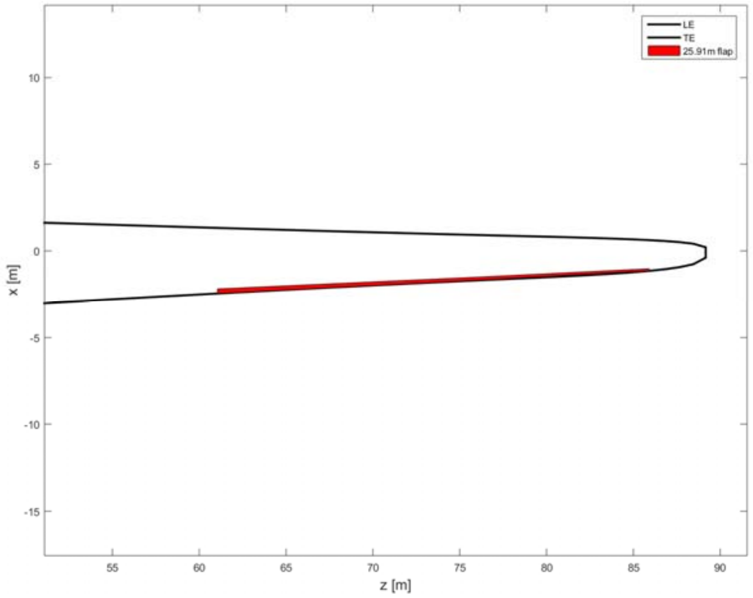

Figure 102: Flap geometry implemented on the 86.3m blade of the DTU 10MW RWT.

Table 28: Load sensor channel parameters.

Name	Description	Unit	Statistic	Ultimate	Fatigue	M	NeqL
MxTB	Tower bottom fore-aft	kNm		x	x	4	1E+07
MyTB	Tower bottom side-side	kNm		x	x	4	1E+07
MxTT	Tower top tilt	kNm		x	x	4	1E+07
MyTT	Tower top roll	kNm		x	x	4	1E+07
MzTT	Tower top yaw	kNm		x	x	4	1E+07
MxMB	Main bearing tilt	kNm		x	x	4	1E+07
MyMB	Main bearing yaw	kNm		x	x	4	1E+07
MzMB	Main bearing torsion	kNm		x	x	4	1E+07
MxBR	Blade root flap	kNm		x	x	10	1E+07
MyBR	Blade root edge	kNm		x	x	10	1E+07
MzBR	Blade root torsion	kNm		x	x	10	1E+07
Power	Electrical power	W	x				
RPM	Rotational speed	rpm	x				
Pitch	Pitch angle	deg	x				
Flap	Flap angle	deg	x				
PitchActiv	Pitch Bearing Activity	deg				1	3E+06
PitchBearing	Pitch Bearing Damage					3	1E+07
FlapActiv	Flap Activity	deg				1	3E+06
TTDist	Distance from blade tips to tow	m					

5.4 Controllers

The baseline controller of the DTU 10MW RWT is originally described in [7]. Due to the fact that the original controller is not designed to handle operation in the full IEC DLCs, the basic DTU wind energy controller is used as described in [12]. The controller features both partial and full load operation as well as switching mechanisms between modes of operation, utilizing measurements of rotor speed, tower accelerations and pitch angles as inputs and the generator torque and collective pitch angle as outputs. Gain scheduling is employed for the pitch angle in full load operation. Furthermore, the controller includes procedures for cut-in, cut-out, overspeed and tower acceleration. A servo model for the pitch actuator is also included, as described in [12]. Finally, fault procedures for handling the relevant IEC fault cases are included.

The individual pitch control (IPC) is added on top of the baseline controller based on [13]. It utilizes flapwise blade root bending moment signals and azimuth position to control the individual pitch angles. The details of the controller are shown in the schematic in [13]. The root moments are transformed to the fixed reference frame resulting in two signals representing the rotor yaw and tilt moments; the rotor tilt and yaw signals are filtered with a low pass and a notch filter that excludes the 3P frequency; two PI loops are then applied to the filtered moment signals. The resulting pitch control signals are then transformed back to the rotating frame by adding a lead angle to the azimuthal position of each of the three blades; the pitch variation from the individual control is superimposed to the collective blade pitch angle. The individual pitch controller is tuned using a similar Ziegler-Nichols based scheme. The tuning procedure is repeated with linear models obtained at different operating wind speeds above rated. Quadratic gain scheduling is employed for wind speeds above rated, based on the average collective pitch angle. The controller parameters are shown in **Table 29**.

Table 29: Individual pitch controller parameters.

Pitch controller parameters	
LPF frequency/damping ratio	0.2 [Hz], 0.7 [-]
Reference pitch angle	0 [deg]
Reference PI gains	0.72 [deg/MNm] 0.26 [deg/MNm*s]
Gain scheduling coefficients	10.1 [deg], 435.2 [deg^2]
Lead angle	38.1 [deg]

Prior studies have explored advanced flap controllers together with various design configurations. In this study a simple individual flap controller (IFC) close to industry standards is chosen, which can also operate at the full DLB, in a realistic setup. The flap control algorithm is implemented similarily to the individual pitch control as described in [14]. It utilizes flapwise blade root bending moment signals and azimuth position to control the individual flap angles. The details of the controller are shown in the schematic in **Figure 103**. The root moments are transformed to the fixed reference frame resulting in two signals representing the rotor yaw and tilt moments; the rotor tilt and yaw signals are filtered with a low pass filter; two PI loops are then applied to the filtered moment signals. The resulting flap control signals are then transformed back to the rotating frame by adding a lead angle to the azimuthal position of each of the three blades. The gains are scheduled as quadratic functions of the average colelctive pitch angle, and an additional gain scheduling is introduced to limit the flap activity below rated power. To account for the actuator physical limitations, the reference flap signal is saturated within the range of allowed deflection, and for the maximum deflection rate. The actuators dynamics are then modelled as a first order low pass filter. The flap controller is not active in partial load operation or normal fault cases.

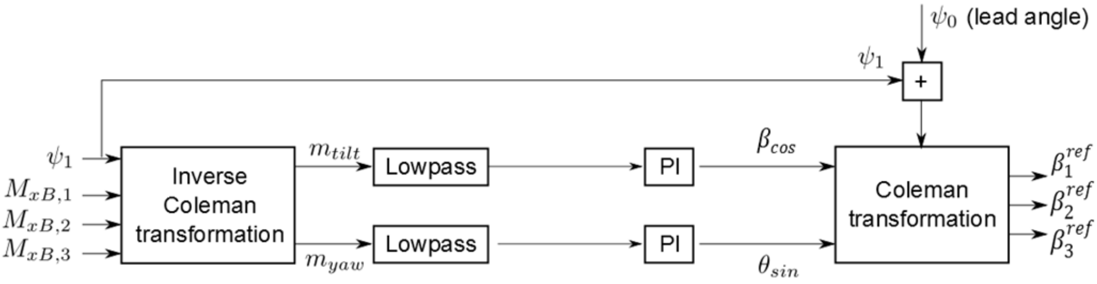

Figure 103: Details of the flap controller.

The PI flap controller gains are tuned based on the response of a high-fidelity linear aero-servo-elastic model of the turbine and its controllers, obtained with HAWCStab2 [15]. HAWCStab2 returns a linearized high order state-space description of the turbine in an open-loop configuration at different operating points, as well as state-space matrices for the linearized collective power control. The individual flap controller in closed loop with the linear plant model is utilized to tune the controller parameters. A closed loop description that includes both power and flap control, returns an indication of the stability for the complete aero-servo-elastic linear system. The gains for the PI flap controllers are found with a Ziegler-Nichols tuning method. The tuning procedure is repeated with linear models obtained at different operating wind speeds above rated. The gains and the frequency at which instability occur while increasing the gains slightly increase with wind speed. To account for the increase, a gain scheduling is introduced as a quadratic function of the mean pitch angle. The controller parameters are shown in Table 30.

Table 30: Individual flap controller parameters.

Flap controller parameters	
LPF frequency/damping ratio	0.1 [Hz], 0.7 [-]
Reference pitch angle	4.58 [deg]
Reference PI gains	4.2452E-03 [deg/kNm] 9.7916E-04 [deg/kNm*s]
Gain scheduling coefficients	3.0562E+01 [deg], -6.1023E+01 [deg^2]
Lead angle	2.3679E+01 [deg]

In the case of the combined controller (IPC+IFC), the flap controller is added on top of the individual pitch controller. Both controllers operate on the rotor level (tilt and yaw moments) with no excplicit frequency separation, but with an added resulting action as a result of difference filter settings. The top level schematic of the combined controller is shown in Figure 104.

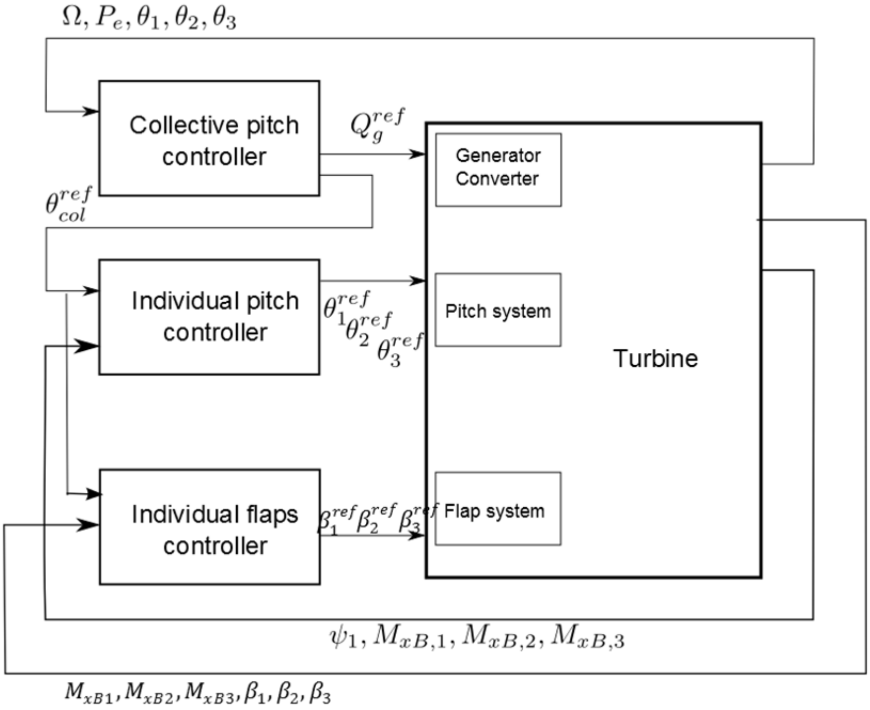

Figure 104: Schematic of the combined pitch and flap controller.

5.5 Results

The results of all cases are analysed according to the post-processing procedure [6] and compared. The following configurations are considered and compared:

- Baseline
- Individual pitch control
- Individual flap control
- Combined individual pitch and flap controls

The analysis is focusing on comparison of lifetime fatigue loads from the DLB, overall extreme loads (including partial safety factors (psf)), as well as comparison of short-term statistics of load and actuator activity channels. The load channels of interest and their associated parameters are shown in **Table 28**.

For the baseline case, the lifetime fatigue loads are shown in **Table 31**, and the overall extreme loads in **Table 32** (sensor names explained in **Table 28**).

Table 31: Fatigue loads for the baseline case.

Sensor	Life time equivalent load	m	neq
MxTB	9.59E+04	4	1E+07
MyTB	6.02E+04	4	1E+07
MxTT	3.23E+04	4	1E+07
MyTT	3.40E+03	4	1E+07
MzTT	3.35E+04	4	1E+07
MxMB	3.96E+04	4	1E+07
MyMB	3.96E+04	4	1E+07
MzMB	1.68E+03	4	1E+07
MxBR	3.05E+04	10	1E+07
MyBR	2.26E+04	10	1E+07
MzBR	5.00E+02	10	1E+07
Pitch activity	1.73E+07	1	3E+06
Pitch bearing damage	8.10E+19	3	1E+07
Flap activity	0.00E+00	1	3E+06

Table 32: Extreme loads for the baseline case.

Sensor	Min incl. psf	Max incl. psf	DLC min	DLC max
MxTB	-2.91E+04	2.80E+05	12_wsp26_wdir000_s1012	12_wsp14_wdir000_s2006
MyTB	-7.84E+04	1.36E+05	12_wsp26_wdir000_s3012	12_wsp26_wdir000_s3012
MxTT	-4.15E+04	5.06E+04	12_wsp26_wdir000_s3012	12_wsp26_wdir000_s1012
MyTT	7.56E+03	1.88E+04	12_wsp12_wdir000_s3005	12_wsp24_wdir000_s4011
MzTT	-4.72E+04	4.55E+04	12_wsp26_wdir000_s2012	12_wsp26_wdir000_s4012
MxMB	-4.48E+04	4.51E+04	12_wsp24_wdir000_s5011	12_wsp26_wdir000_s4012
MyMB	-4.46E+04	4.32E+04	12_wsp22_wdir000_s5010	12_wsp26_wdir000_s3012
MzMB	-1.51E+04	-9.56E+03	12_wsp26_wdir000_s2012	12_wsp12_wdir000_s4005
MxBR	-5.29E+04	2.89E+04	12_wsp12_wdir000_s3005	12_wsp24_wdir000_s4011
MyBR	-2.00E+04	2.00E+04	12_wsp26_wdir000_s3012	12_wsp20_wdir000_s3009
MzBR	-7.34E+02	7.26E+02	12_wsp24_wdir000_s6011	12_wsp24_wdir000_s1011
TTDist	8.45E+00	-	12_wsp12_wdir000_s5005	-

For the individual pitch control case, the lifetime fatigue loads are shown in Table 33, and the overall extreme loads in Table 34 (sensor names explained in Table 28).

Table 33: Fatigue loads for the individual pitch control (IPC) case.

Sensor	Life time equivalent load	m	neq
MxTB	9.49E+04	4	1E+07
MyTB	6.52E+04	4	1E+07
MxTT	3.11E+04	4	1E+07
MyTT	3.25E+03	4	1E+07
MzTT	3.14E+04	4	1E+07
MxMB	3.95E+04	4	1E+07
MyMB	3.94E+04	4	1E+07
MzMB	1.61E+03	4	1E+07
MxBR	2.34E+04	10	1E+07
MyBR	2.20E+04	10	1E+07
MzBR	4.30E+02	10	1E+07
Pitch activity	7.19E+07	1	3E+06
Pitch bearing damage	2.21E+20	3	1E+07
Flap activity	0.00E+00	1	3E+06

Table 34: Extreme loads for the individual pitch control (IPC) case.

Sensor	Min incl. psf	Max incl. psf	DLC min	DLC max
MxTB	-3.79E+04	2.76E+05	12_wsp26_wdir000_s3012	12_wsp12_wdir000_s3005
MyTB	-9.02E+04	1.23E+05	12_wsp26_wdir000_s2012	12_wsp24_wdir000_s5011
MxTT	-4.68E+04	2.95E+04	12_wsp22_wdir000_s3010	12_wsp16_wdir000_s2007
MyTT	7.58E+03	1.73E+04	12_wsp12_wdir000_s3005	12_wsp22_wdir000_s5010
MzTT	-3.72E+04	4.68E+04	12_wsp26_wdir000_s2012	12_wsp26_wdir000_s2012
MxMB	-4.56E+04	4.72E+04	12_wsp24_wdir000_s6011	12_wsp26_wdir000_s4012
MyMB	-4.66E+04	4.80E+04	12_wsp24_wdir000_s1011	12_wsp26_wdir000_s2012
MzMB	-1.48E+04	-9.54E+03	12_wsp26_wdir000_s4012	12_wsp12_wdir000_s4005
MxBR	-5.27E+04	1.69E+04	12_wsp12_wdir000_s3005	12_wsp26_wdir000_s4012
MyBR	-1.95E+04	2.11E+04	12_wsp26_wdir000_s4012	12_wsp20_wdir000_s5009
MzBR	-6.15E+02	6.41E+02	12_wsp26_wdir000_s4012	12_wsp26_wdir000_s2012
TTSDist	8.21E+00	-	12_wsp12_wdir000_s5005	-

For the individual flap control case, the lifetime fatigue loads are shown in Table 35, and the overall extreme loads in Table 36 (sensor names explained in Table 28).

Table 35: Fatigue loads for the individual flap control (IFC) case.

Sensor	Life time equivalent load	m	neq
MxTB	9.60E+04	4	1E+07
MyTB	6.08E+04	4	1E+07
MxTT	3.14E+04	4	1E+07
MyTT	3.26E+03	4	1E+07
MzTT	3.18E+04	4	1E+07
MxMB	3.71E+04	4	1E+07
MyMB	3.68E+04	4	1E+07
MzMB	1.69E+03	4	1E+07
MxBR	2.51E+04	10	1E+07
MyBR	2.25E+04	10	1E+07
MzBR	5.17E+02	10	1E+07
Pitch activity	1.74E+07	1	3E+06
Pitch bearing damage	7.64E+19	3	1E+07
Flap activity	4.50E+08	1	3E+06

Table 36: Extreme loads for the individual flap control (IFC) case.

Sensor	Min incl. psf	Max incl. psf	DLC min	DLC max
MxTB	-3.95E+04	2.79E+05	12_wsp26_wdir000_s1012	12_wsp14_wdir000_s2006
MyTB	-9.23E+04	1.27E+05	12_wsp26_wdir000_s2012	12_wsp26_wdir000_s2012
MxTT	-3.82E+04	4.09E+04	12_wsp22_wdir000_s3010	12_wsp22_wdir000_s3010
MyTT	7.44E+03	1.80E+04	12_wsp12_wdir000_s3005	12_wsp24_wdir000_s4011
MzTT	-3.87E+04	4.30E+04	12_wsp26_wdir000_s2012	12_wsp26_wdir000_s4012
MxMB	-3.78E+04	3.91E+04	12_wsp22_wdir000_s1010	12_wsp22_wdir000_s3010
MyMB	-3.68E+04	4.10E+04	12_wsp22_wdir000_s1010	12_wsp24_wdir000_s4011
MzMB	-1.51E+04	-9.28E+03	12_wsp26_wdir000_s2012	12_wsp12_wdir000_s4005
MxBR	-5.25E+04	2.34E+04	12_wsp12_wdir000_s3005	12_wsp24_wdir000_s4011
MyBR	-2.00E+04	2.04E+04	12_wsp26_wdir000_s3012	12_wsp20_wdir000_s3009
MzBR	-7.18E+02	6.23E+02	12_wsp24_wdir000_s6011	12_wsp26_wdir000_s3012
TTSDist	7.19E+00	-	12_wsp12_wdir000_s6005	-

For the combined individual pitch and flap control case, the lifetime fatigue loads are shown in Table 37, and the overall extreme loads in Table 38 (sensor names explained in Table 28).

Table 37: Fatigue loads for the combined individual pitch and flap control (IPC+IFC) case.

Sensor	Life time equivalent load	m	neq
MxTB	1.03E+05	4	1E+07
MyTB	7.24E+04	4	1E+07
MxTT	3.32E+04	4	1E+07
MyTT	3.47E+03	4	1E+07
MzTT	3.32E+04	4	1E+07
MxMB	4.09E+04	4	1E+07
MyMB	4.05E+04	4	1E+07
MzMB	1.69E+03	4	1E+07
MxBR	2.29E+04	10	1E+07
MyBR	2.20E+04	10	1E+07
MzBR	4.92E+02	10	1E+07
Pitch activity	8.95E+07	1	3E+06
Pitch bearing damage	2.16E+20	3	1E+07
Flap activity	4.09E+08	1	3E+06

Table 38: Extreme loads for the combined individual pitch and flap control (IPC+IFC) case.

Sensor	Min incl. psf	Max incl. psf	DLC min	DLC max
MxTB	-5.02E+04	2.80E+05	12_wsp26_wdir000_s2012	12_wsp14_wdir000_s2006
MyTB	-1.09E+05	1.36E+05	12_wsp26_wdir000_s2012	12_wsp26_wdir000_s2012
MxTT	-4.59E+04	2.96E+04	12_wsp22_wdir000_s3010	12_wsp22_wdir000_s3010
MyTT	7.47E+03	1.71E+04	12_wsp12_wdir000_s3005	12_wsp22_wdir000_s5010
MzTT	-2.89E+04	4.40E+04	12_wsp26_wdir000_s2012	12_wsp26_wdir000_s2012
MxMB	-4.50E+04	4.51E+04	12_wsp26_wdir000_s4012	12_wsp26_wdir000_s2012
MyMB	-3.81E+04	4.40E+04	12_wsp26_wdir000_s4012	12_wsp22_wdir000_s2010
MzMB	-1.52E+04	-9.28E+03	12_wsp26_wdir000_s2012	12_wsp12_wdir000_s4005
MxBR	-5.31E+04	1.72E+04	12_wsp12_wdir000_s3005	12_wsp26_wdir000_s4012
MyBR	-1.95E+04	2.07E+04	12_wsp26_wdir000_s3012	12_wsp20_wdir000_s5009
MzBR	-6.28E+02	8.55E+02	12_wsp26_wdir000_s4012	12_wsp26_wdir000_s2012
TTSDist	7.02E+00	-	12_wsp12_wdir000_s6005	-

For the combined control case, an example time series at 16mps showing the reduction of the flapwise root bending moment (**Figure 105**) and the corresponding flap activity (**Figure 106**) is shown.

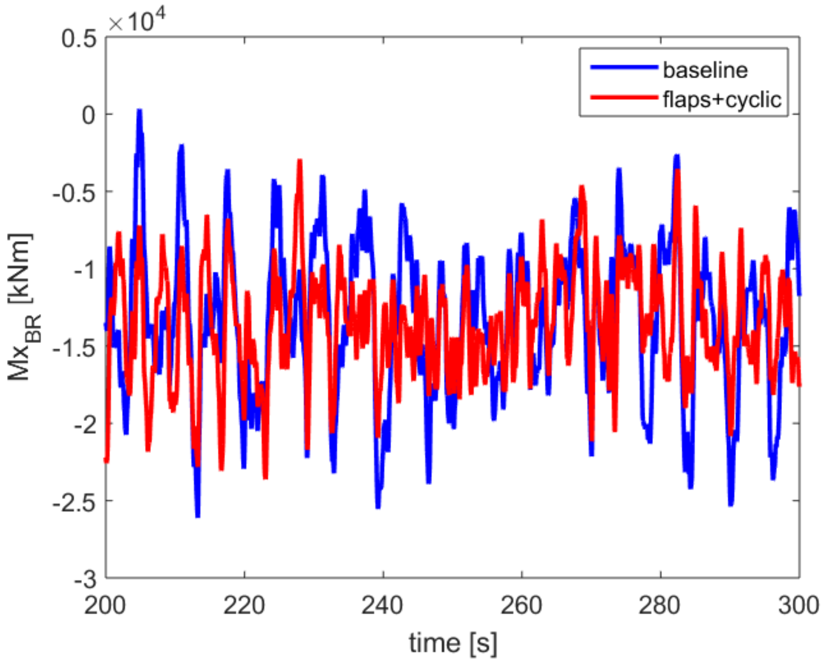

Figure 105: Time series of blade root flapwise bending moment for the baseline and combined control cases at 16m/s.

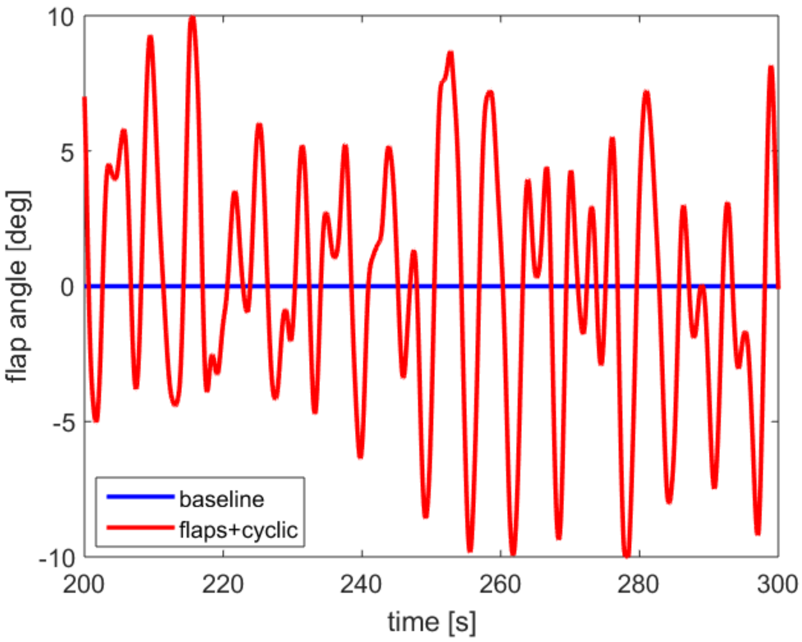

Figure 106: Time series of resulting flap angle for the baseline and combined control cases at 16m/s.

The lifetime fatigue loads (**Figure 107**) and overall extreme loads for all cases are compared in terms of the overall extreme maximum (**Figure 108**), extreme minimum (**Figure 109**). Also the lifetime pitch bearing damage and pitch and flap activities are included.

All the three control concepts significantly reduce the lifetime fatigue loads for certain load channels, mostly on the flapwise root moment (MxBR), which is the load channel targeted by the load control algorithms. The flap controls deliver a reduction of 23% while the pitch controls 23%, and the combined controls 25%. The load reduction is achieved at the cost of higher actuators activity: the pitch activity for the individual pitch configuration increase by a factor of 3 compared to the baseline one, but the pitch bearing equivalent damage increases only by a factor of 1.7, as the flapwise load variation is reduced. The flap control case presents a negligible increase of the pitch activity, while the pitch equivalent damage is reduced (-5%), as the loads on the bearing are alleviated. The combination of both flap and individual pitch returns the highest fatigue load alleviation, and also allows a slight decrease in the pitch bearing equivalent damage compared to the individual pitch control case. In terms of adverse effects, the flap controls result in slightly increased (3%) blade torsion loads due to the increased pitching moment, and the combined controls show some considerable increase in the tower bottom (mostly side-to-side) fatigue loads, which is probably a result of controller interaction and needs to be further investigated.

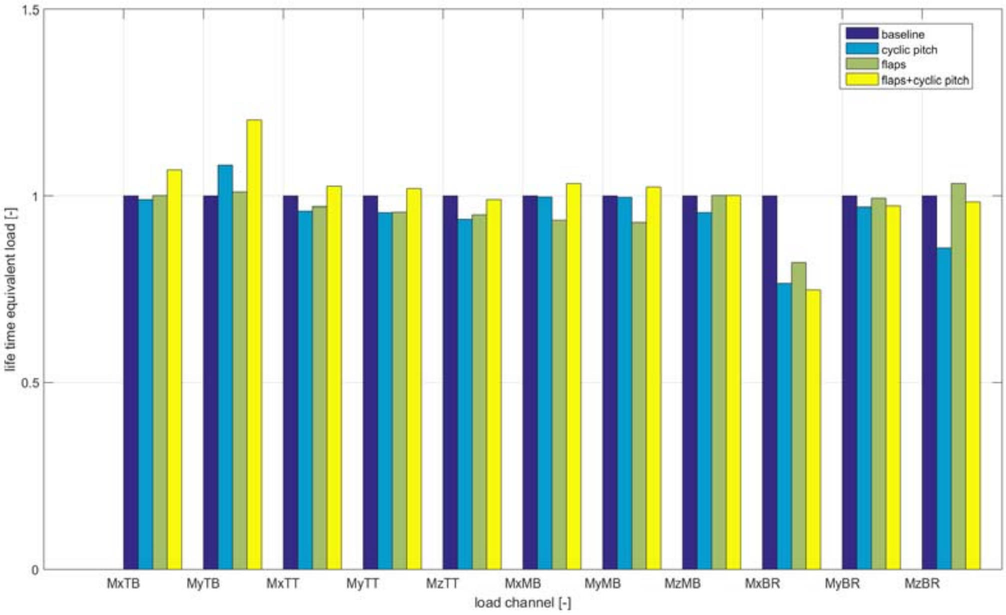

Figure 107: Comparison of lifetime fatigue loads between cases (loads normalized by baseline loads).

Although on a full DLB, overall extreme loads would be dominated by other DLCs rather than DLC1.2, comparison of extreme loads shows generally a potential for reduction of maximum loads in a series of load channels. In extreme minimum loads though, significant load increases take place in tower loads for all control methods, whereas a reduction potential is seen for bearing and tower top torsion loads. The design load cases in which the extreme loads appear (Table 32, Table 34, Table 36, Table 38), generally show that design loads generally occur at very high wind speeds close to cut out.

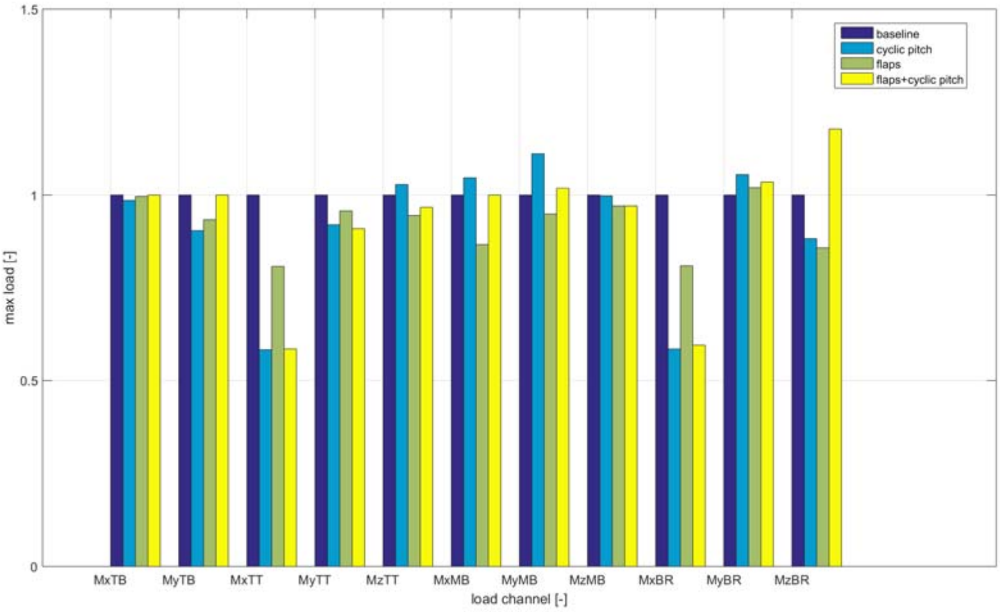

Figure 108: Comparison of extreme maximum loads between cases (loads normalized by baseline loads).

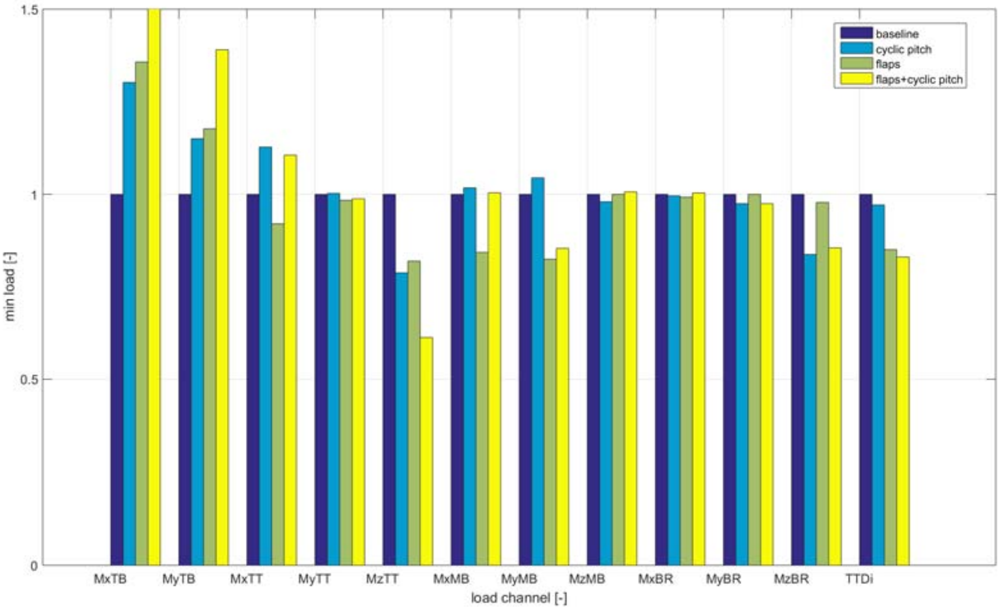

Figure 109: Comparison of extreme minimum loads between cases (loads normalized by baseline loads).

Representative statistics are also shown in

Table 39, focusing on the comparison of the range and variance of key load channels. The comparison control cases with the baseline case in terms of % difference of representative statistics is shown in Table 40.

The comparison of statistics shows that the individual pitch control reduces the average load signal variance more than the individual flap control, whereas the combined control does not give further decrease (while it does provide further decrease in fatigue load). Again, the pitch signal variance slightly decreases in the combined controller with the use of the flaps compared to the individual pitch case. The flap activity is also reduced in the combined case compared to the individual flap control case .

Table 39: Comparison of representative statistics of all cases (averaged over all load cases).

	MxBR min [kNm]	MxBR max [kNm]	MxBR std [kNm]	MxTT min [kNm]	MxTT max [kNm]	MxTT std [kNm]	Pitch std [deg]	Flap std [deg]
baseline	-5.29E+04	2.89E+04	7.89E+03	-4.15E+04	5.06E+04	8.56E+03	2.8923	0.0000
IPC	-5.27E+04	1.69E+04	5.35E+03	-4.69E+04	2.95E+04	6.86E+03	3.6709	0.0000
IFC	-5.25E+04	2.34E+04	5.92E+03	-3.82E+04	4.09E+04	7.27E+03	2.9096	8.3805
IPC+IFC	-5.31E+04	1.72E+04	5.40E+03	-4.59E+04	2.96E+04	7.03E+03	3.5531	6.6731

Table 40: % difference of representative statistics of control cases compared to the baseline (Negative sign denotes reduction. Flap std of IPC+IFC case compared to the IFC case).

	MxBR min	MxBR max	MxBR std	MxTT min	MxTT max	MxTT std	Pitch std	Flap std
IPC	-0.34	-41.52	-32.15	12.85	-41.62	-19.92	26.92	-
IFC	-0.58	-19.28	-24.89	-8.02	-19.12	-15.08	0.60	-
IPC+IFC	0.49	-40.64	-31.55	10.51	-41.50	-17.91	22.85	-20.37

In Figure 110, the short term equivalent load statistics for the blade root flapwise moment are shown for every wind speed, where all cases are compared. It is seen that on average the individual pitch and flap controls achieve considerable reduction of fatigue loading in full load operation, with increased alleviation when combined.

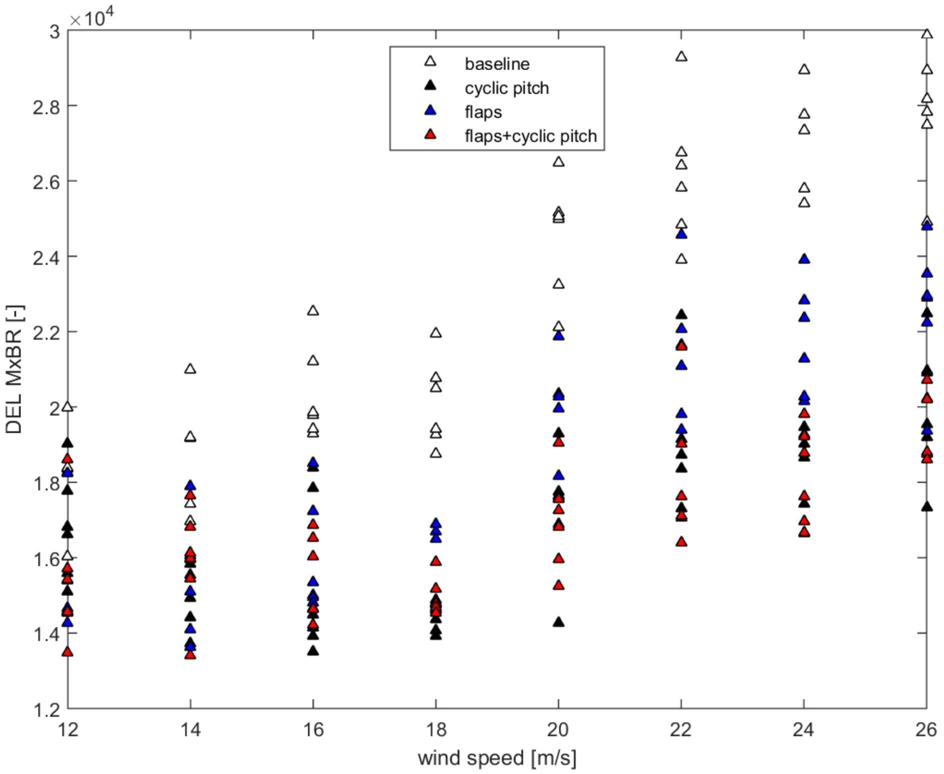

Figure 110: Comparison of flapwise root moment short term fatigue equivalent loads between all cases.

In **Figure 111**, the pitch bearing short term equivalent loads are shown for every wind speed, where all cases are compared. It is seen that on average the individual pitch controls increase considerable the bearing damage, while the flap controls slightly decrease it (compared to the baseline) and the combined controls show a slight decrease compared to the individual pitch control.

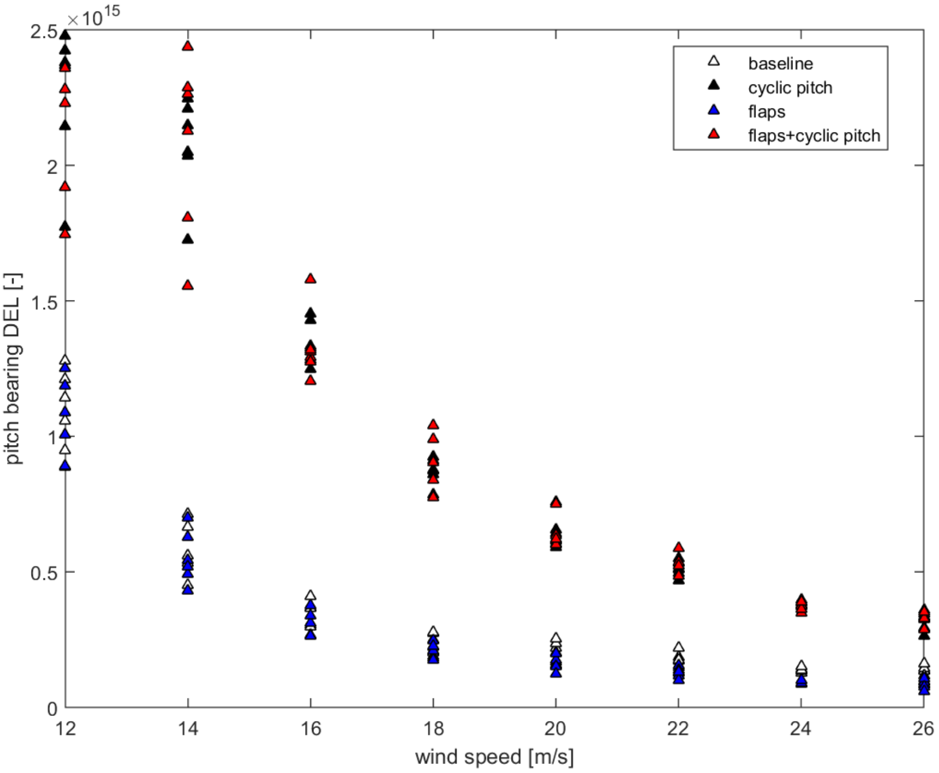

Figure 111: Comparison pitch bearing short term fatigue equivalent loads between all cases.

In **Figure 112**, the pitch activity is shown for every wind speed, where all cases are compared and the similar trend is seen as in the case of the pitch bearing damage. It is seen that on average the individual pitch controls greatly increase the activity as expected, while the flap controls slightly decrease it (compared to the baseline) and the combined controls show a slight decrease compared to the individual pitch control.

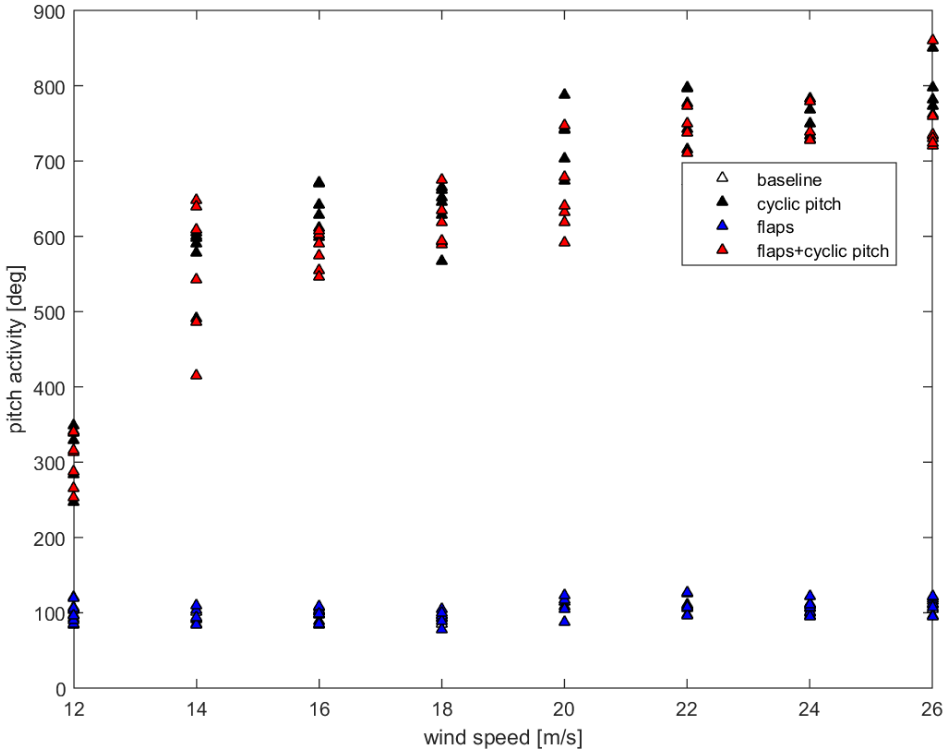

Figure 112: Comparison of pitch activity (distance travelled) for all cases.

In **Figure 113**, the flap activity is shown for every wind speed, where all cases are compared. It is seen that there is an average decrease in the flap activity in the combined case when compared to the flap only case.

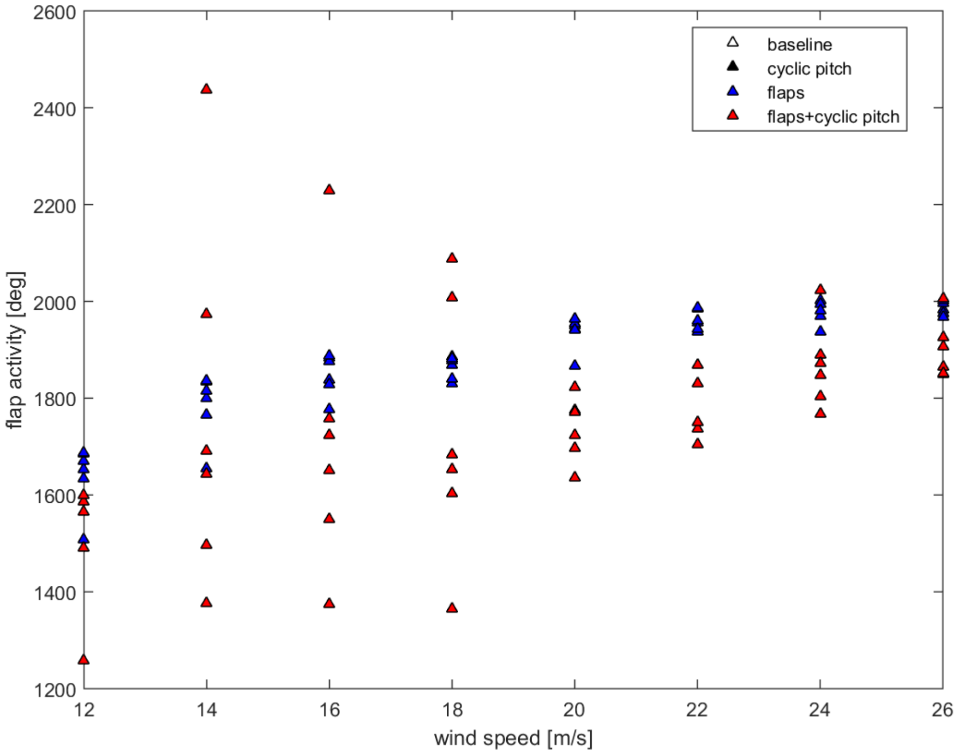

Figure 113: Comparison of flap activity (distance travelled) for all cases.

All load alleviation control concepts show no influence on average power performance, as they are all designed to be mainly operational above rated power conditions. The impact on the Annual Energy Production (AEP) is minimal; a decrease of less than 0.2% is reported.

In addition to the DLC1.2 cases, the flap fault cases defined in **Table 4** are simulated. The flap fault signals for the one flap motion to maximum limit (**Figure 114**) and the flap motions to zero, maximum and minimum limits (**Figure 115**) are shown. The flap actuator dynamics are visible at the time of the fault.

Compared to the baseline case extreme loads, the flap fault case DLC2.2f2 (asymmetric flap motion) shows increase of 3-5% in the resulting extreme blade root flapwise and edgewise bending moments, while the torsional moment increases considerably by 43%.

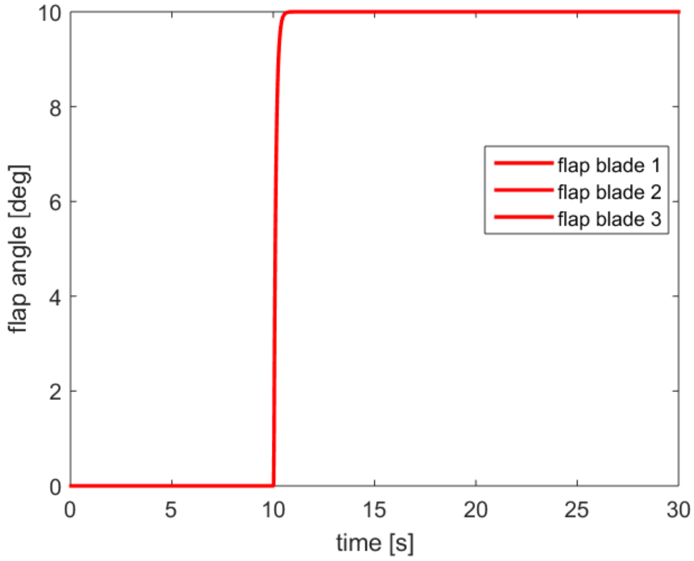

Figure 114: Flap fault signals for DLC 2.2f1.

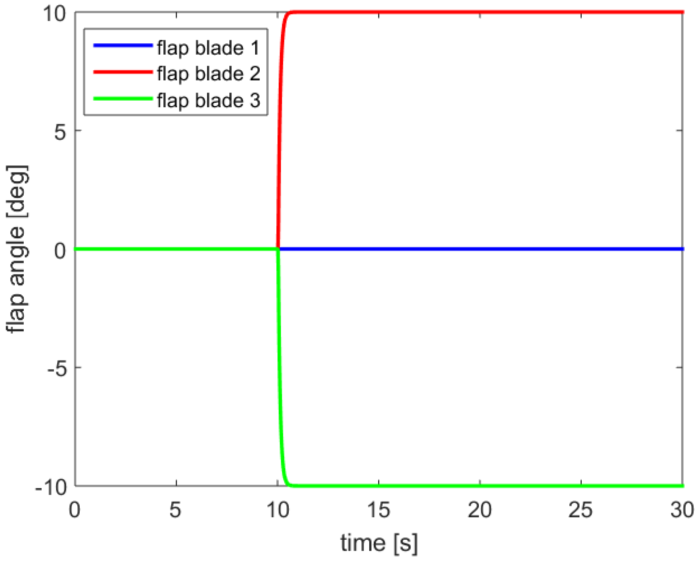

Figure 115: Flap fault signal for DLC 2.2f2.

5.6 Conclusions

- A representative flap system has been modelled in the aeroelastic tool HAWC2, where individual flap and pitch controllers are active for operation in above rated normal power production.
- Normal power production and flap fault design load cases are simulated with the full aeroelastic model in HAWC2.
- The baseline, individual pitch control, individual flap control and individual pitch and flap combined control cases are compared in terms of overall lifetime fatigue and extreme loads on major component load channels.
- All controllers achieve significant fatigue load reduction up to 25% in most of the load channels.

- Flap control shows a benefit over pitch control in terms of reducing the pitch bearing fatigue load, while the combined control reduces the flap activity compared to the flap control.
- A potential for also reducing extreme loads in a range of load channels is seen, while certain loads are considerably increased.
- The flap fault cases show a slight increase in extreme loads compared to the baseline operation.

5.7 References

[1] Madsen, H. A. et al., Towards an industrial manufactured morphing trailing edge flap system for wind turbines, Proceedings of EWEC 2014, Barcelona, Spain, 2014.

[2] Barlas, T. K. and van Kuik, G. A. M., Review of state of the art in smart rotor control research for wind turbines, Progress in Aerospace Sciences — 2010, Volume 46, Issue 1, pp. 1-27, 2010.

[3] Hansen, M. H. et al., Design Load Basis for onshore turbines, Technical report, DTU Vindenergi-E-0174(EN), 2015 (orbit.dtu.dk).

[4] IEC. IEC 61400-1. Wind turbines – Part 1: Design Requirements, 2005.

[5] Verelst, D., prepost-wind-dlc INDUFLAP_v0.1, http://dx.doi.org/10.5281/zenodo.13370.

[6] Pedersen, M. M., Post processing of Design Load Cases using Pdap, Technical report, DTU Vindenergi-I-0371(EN), 2014.

[7] Bak, C. et al Description of the DTU 10 MW Reference Wind Turbine, Technical report, DTU Vindenergi-I-0092, 2013.

[8] Larsen, T. J. et al., How 2 Hawc2, the user's manual, Technical report, Risø-R-1597(ver. 4-4)(EN), 2013.

[9] Bergami, L., Adaptive Trailing Edge Flaps for Active Load Alleviation in a Smart Rotor Configuration, PhD thesis, DTU Wind Energy, 2013.

[10] Bergami, L. and Gaunaa, M., ATEFlap Aerodynamic Model, a dynamic stall model including the effects of trailing edge flap deflection, Technical report, Risø-R-1792(EN), 2012.

[11] N. N. Sørensen. General purpose flow solver applied to flow over hills. Technical Report Risø-R-827(EN), 1995.

[12] Hansen, M. H. et al., Basic DTU Wind Energy controller, Technical report, DTU Vindenergi-E-0018(EN), Edition 2, 2015 (orbit.dtu.dk).

[13] Bossanyi, E. A., Further load reductions with individual pitch control, Wind Energy, 8 (4): 481-485.

[14] Bergami, L. and Hansen M. H., A Linear Time Invariant Model of a Smart Rotor with Adaptive Trailing Edge Flaps, Wind Energu, to appear.

[15] Hansen, M. H., Aeroelastic stability analysis of wind turbines using an eigenvalue approach, Wind Energy, 7:133-143, 2004.

6 VALIDATION 5: PURE ROTOR AERODYNAMIC SIMULATIONS WITH PRESCRIBED FLAP (ALL)

6.1 Pure Rotor Aerodynamic Simulations

Simulations of a pure stiff rotor configuration are performed in order to assess the impact of prescribed flap motion on the aerodynamic loads on a blade sectional and rotor integral level. Results of the engineering models used by DTU (HAWC2), TUD (Bladed) and NTUA (hGAST) are compared to the CFD predictions of USTUTT-IAG.

6.2 Operating Cases

All simulated cases concern a uniform constant flow wind input and constant rotor speed and blade pitch angle. The prescribed flap input (same on all blades) consists of a sinusoidal signal with max/min flap amplitude and frequency relevant multiples of the rotor frequency (1p, 3p, and 6p). Operating parameters are shown in Table 41.

Table 41: Operating parameters of simulated cases.

Case	11.4 m/s 1p sine	11.4 m/s 3p sine	11.4 m/s 6p sine	19 m/s 6p sine
Wind speed [m/s]	11.4	11.4	11.4	19
Rotor speed [rpm]	9.6	9.6	9.6	9.6
Pitch angle [deg]	0	0	0	16.432
Flap function	sine	sine	sine	sine
Flap frequency [n*p]	1	3	6	6
Flap max amplitude [deg]	±10	±10	±10	±10

6.3 Modelling Environment and Configuration

All engineering model cases utilise a stiff structure configuration, no blades precone, no rotor tilt and the prescribed control inputs. The simulated flap configuration is shown in Table 42. The pure aerodynamic results obtained from CFD have already been detailed in Chapter 2.

Table 42: Parameters of simulated flap configuration.

Flap configuration	
Chordwise extension	10%
Deflection angle limits	±10°
Spanwise length	8.9m (10% blade length)
Spanwise location	71.32m-62.40m (from rotor center)
Airfoil	FFA-W3-241
Max ΔC_l	0.4

The 2D lift/drag/moment polars are generated for the case of the simulations of NTUA (hGAST) using the code FOIL2W, using a Reynold's number of 4.5×10^6, for transitional conditions, corresponding to flap mid-span conditions at a wind speed of 10 m/s. The same polars are used for the simulations of Bladed (TUD). On the other hand, for the simulations of DTU (HAWC2), the polars are generated using EllipSys2D, for a Reynold's number between 6×10^6-12×10^6, for free transition with turbulence intensity 0.1, 3D corrected using Bak's model.

6.4 Results

The presented simulation results consist of time series of sectional loads (out-of-plane and in-plane forces) at the 75% radial section (flap mid-span) and integral rotor response (thrust and power), shown for one revolution. Furthermore, the radial distribution of sectional forces is compared for the time instances where the flap is at neutral and extreme positions.

11.4m/s – 1p flap input

The flap input signal at 1p frequency is shown in Figure 116. The sectional axial (out-of-plane) and tangential (in-plane) forces are shown in Figure 117 and Figure 118. The rotor thrust and power are shown in Figure 119 and Figure 121.

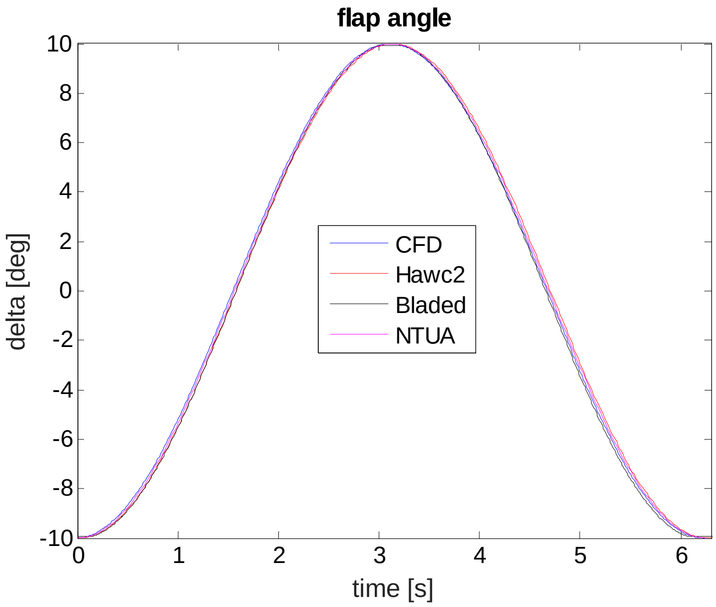

Figure 116: Prescribed flap angle, wind speed 11.4 m/s, flap angle sine 1p

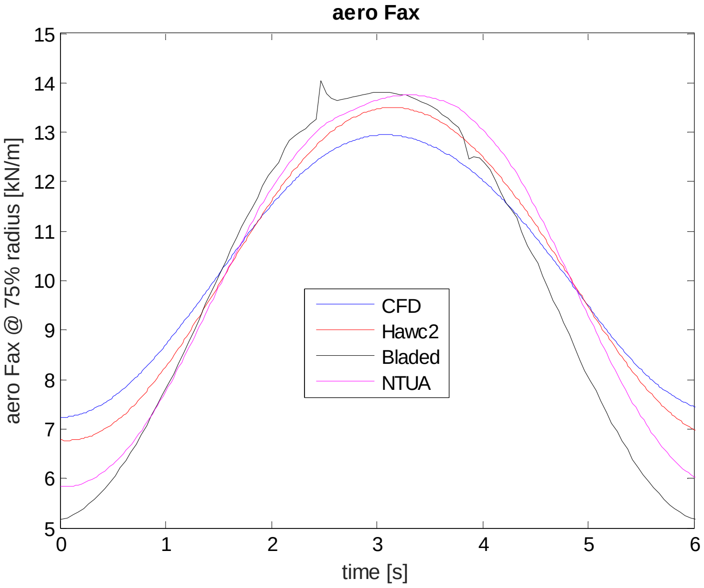

Figure 117: Axial sectional aerodynamic force, wind speed 11.4 m/s, flap angle sine 1p

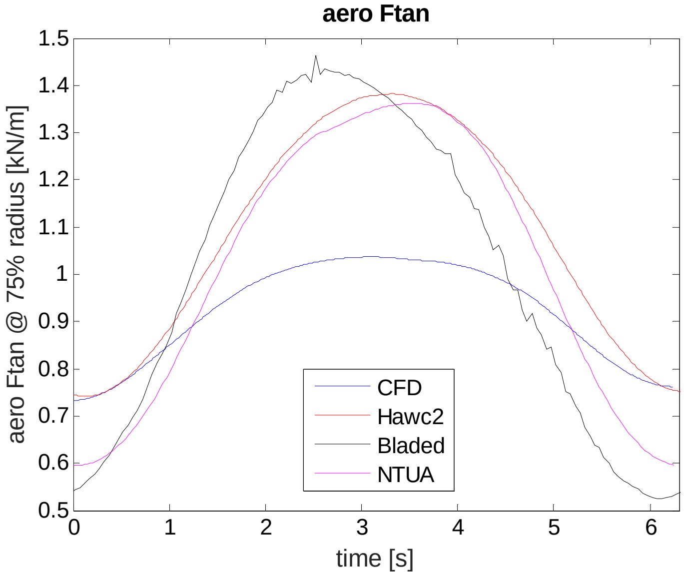

Figure 118: Tangential sectional aerodynamic force, wind speed 11.4 m/s, flap angle sine 1p

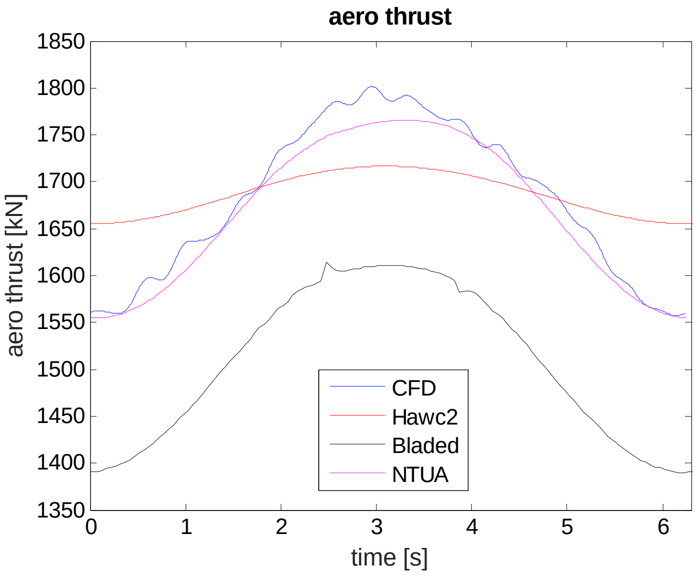

Figure 119: Rotor thrust, wind speed 11.4 m/s, flap angle sine 1p

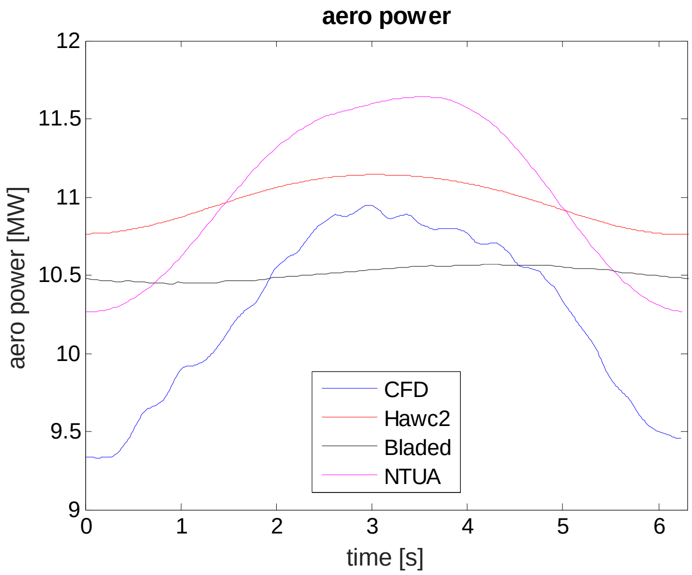

Figure 120: Rotor power, wind speed 11.4 m/s, flap angle sine 1p

The sectional axial (out-of-plane) and tangential (in-plane) force radial distributions are shown for the time instance when the flap is at neutral position (Figure 121 and Figure 122), for the time instance when the flap is at maximum positive position (Figure 123 and Figure 124), and for the time instance when the flap is at maximum negative position (Figure 125 and Figure 126).

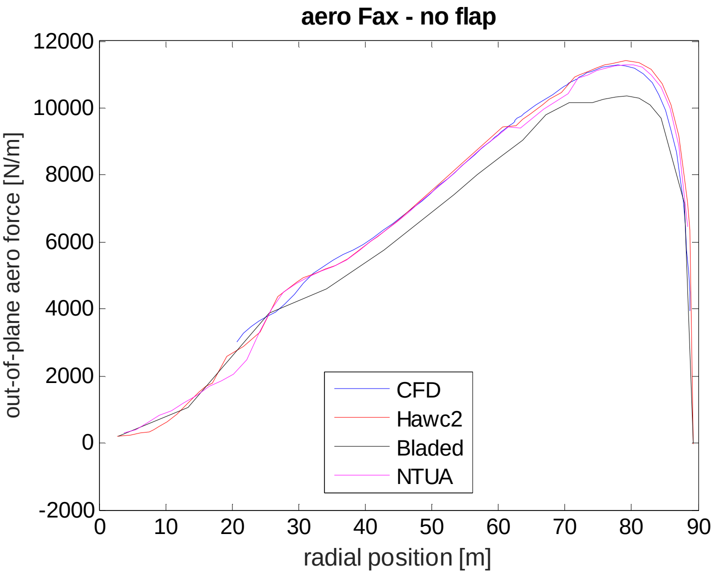

Figure 121: Axial sectional aerodynamic force, wind speed 11.4 m/s, flap neutral position

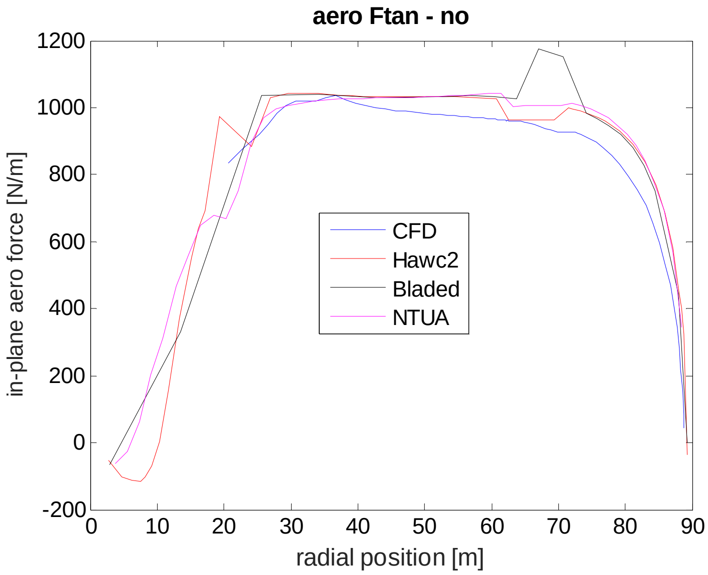

Figure 122: Tangential sectional aerodynamic force, wind speed 11.4 m/s, flap neutral position

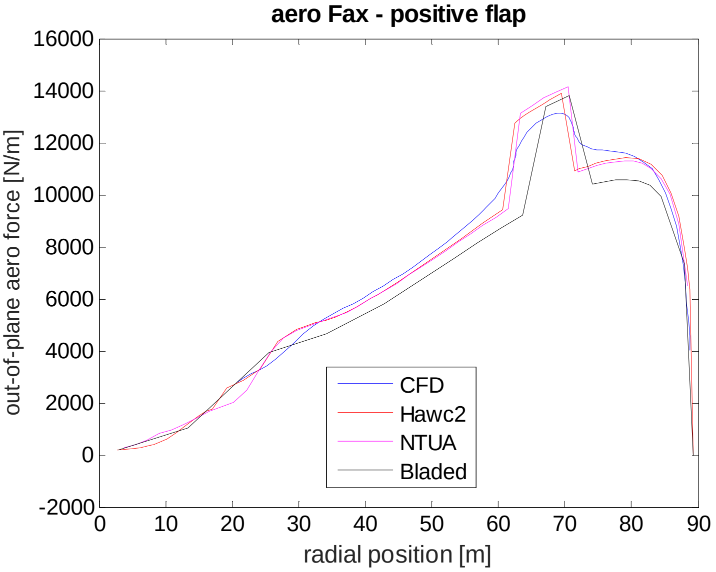

Figure 123: Axial sectional aerodynamic force, wind speed 11.4 m/s, flap positive 10° position

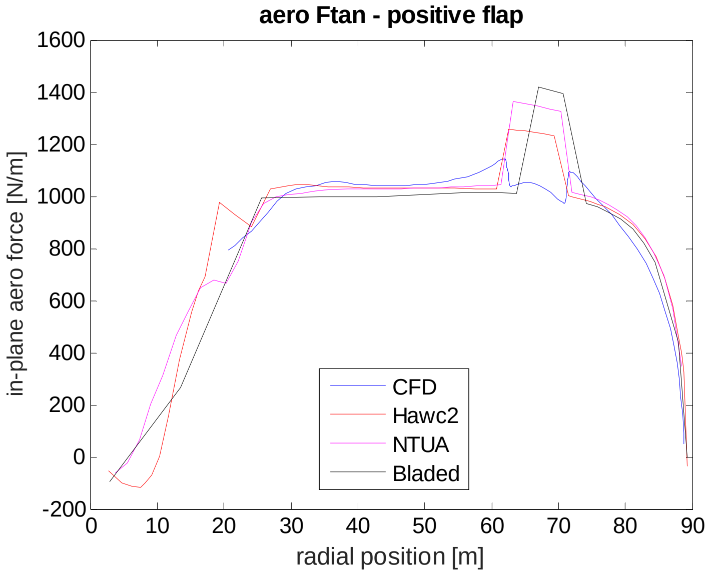

Figure 124: Tangential sectional aerodynamic force, wind speed 11.4 m/s, flap positive 10° position

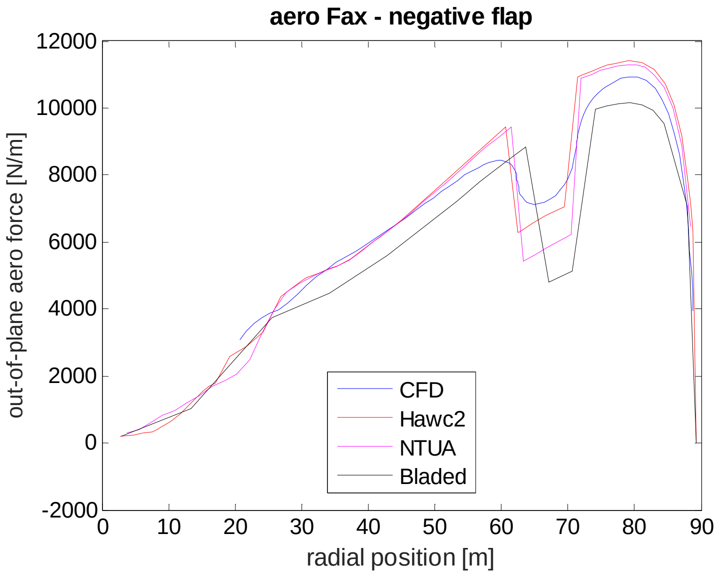

Figure 125: Axial sectional aerodynamic force, wind speed 11.4 m/s, flap negative 10° position

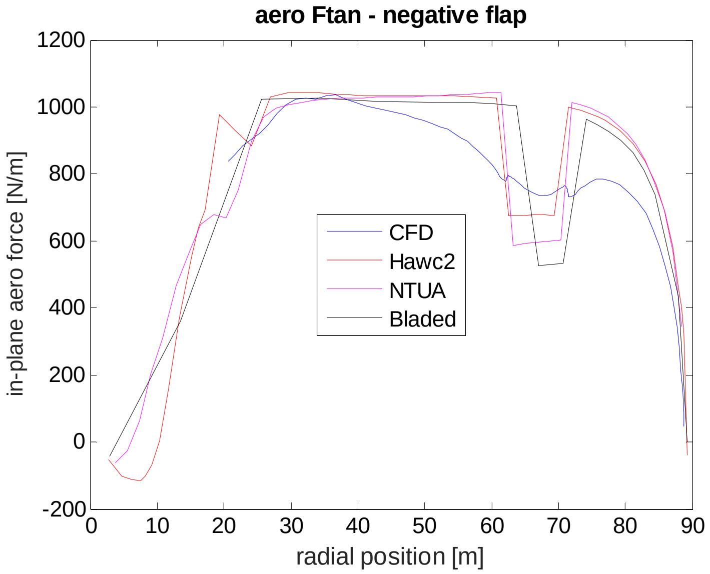

Figure 126: Tangential sectional aerodynamic force, wind speed 11.4 m/s, flap negative 10° position

It is seen that the predictions of the sectional axial force variation in time due to the flap action are comparing well, but the tangential force variation is largely underpredicted by CFD compared to the engineering models due to a higher prediction of the drag force. As the CFD simulations have been conducted under fully turbulent conditions, a higher drag is expected with regard to the provided polars. In terms of radial distribution, the axial force comparison is fair, with the expected smoothing of distribution around the flap region predicted by CFD. The tangential force distribution is quite different with the local increase/decrease due to the flap action being more evident in the engineering models. Due to the shown discrepancies, the rotor thrust and power variations show higher variations in CFD compared to the engineering models.

11.4m/s – 3p flap input

The flap input signal at 3p frequency is shown in Figure 127. The sectional axial (out-of-plane) and tangential (in-plane) forces are shown in Figure 128 and Figure 129. The rotor thrust and power are shown in Figure 130 and Figure 131.

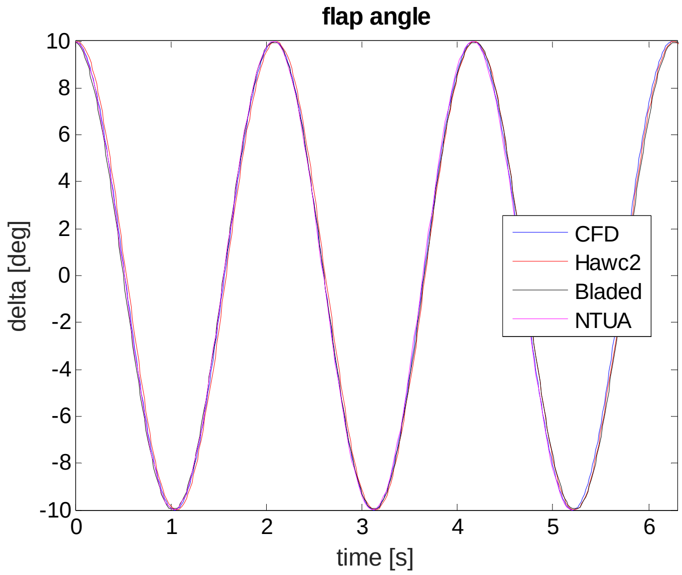

Figure 127: Prescribed Flap Angle, wind speed 11.4 m/s, flap angle sine 3p

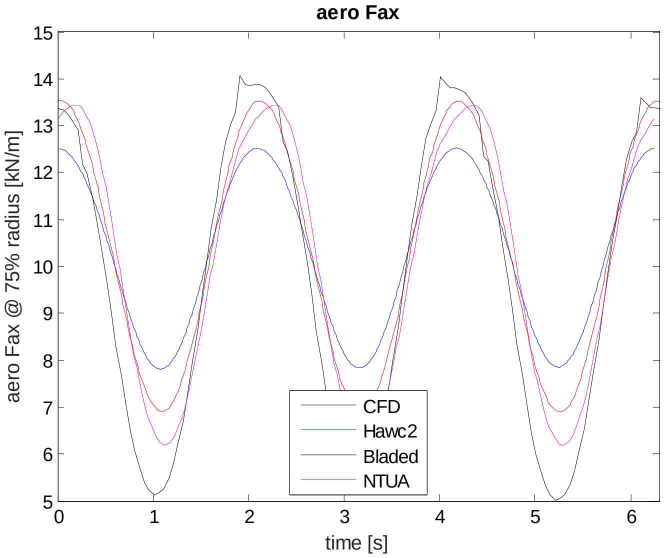

Figure 128: Sectional out-of-plane aerodynamic force, wind speed 11.4 m/s, flap angle sine 3p

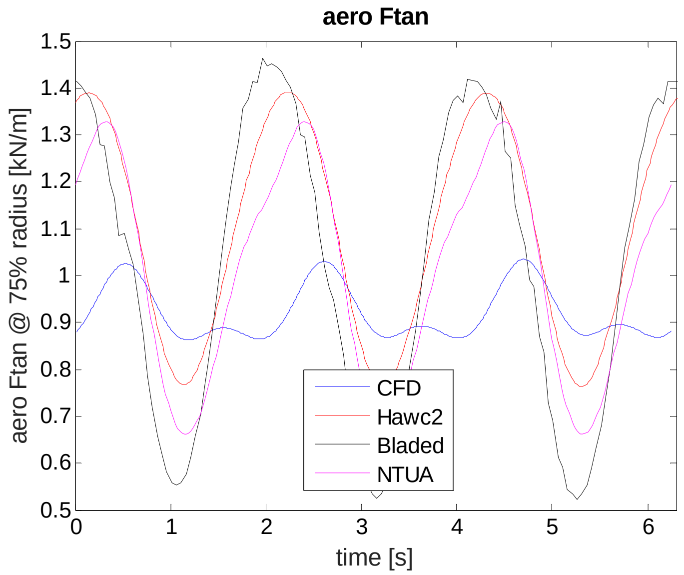

Figure 129: Sectional in-plane aerodynamic force, wind speed 11.4 m/s, flap angle sine 3p

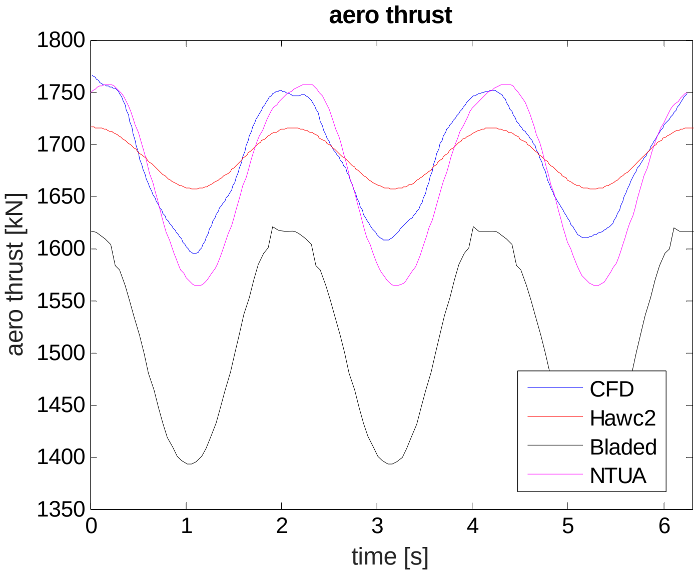

Figure 130: Rotor Thrust, wind speed 11.4 m/s, flap angle sine 3p

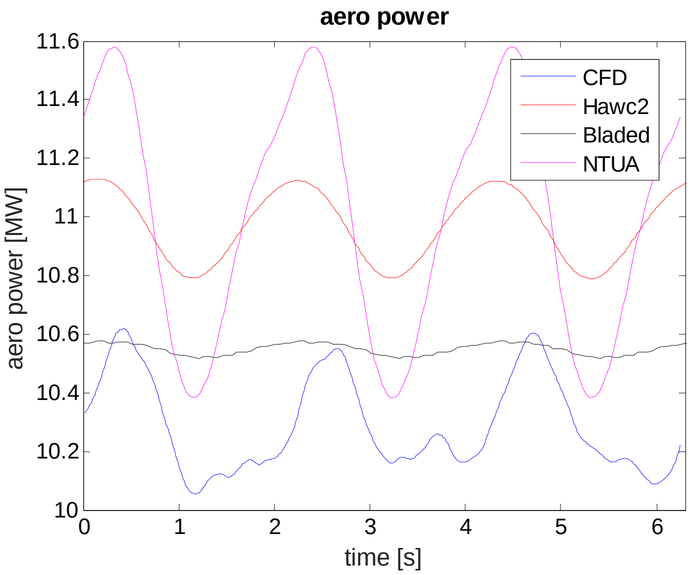

Figure 131: Aerodynamic Power, wind speed 11.4 m/s, flap angle sine 3p

The sectional axial (out-of--plane) and tangential (in-plane) force radial distributions are shown for the time instance when the flap is at neutral position (Figure 132 and Figure 133), for the time instance when the flap is at maximum positive position (Figure 134 and Figure 135), and for the time instance when the flap is at maximum negative position (Figure 136 and Figure 137).

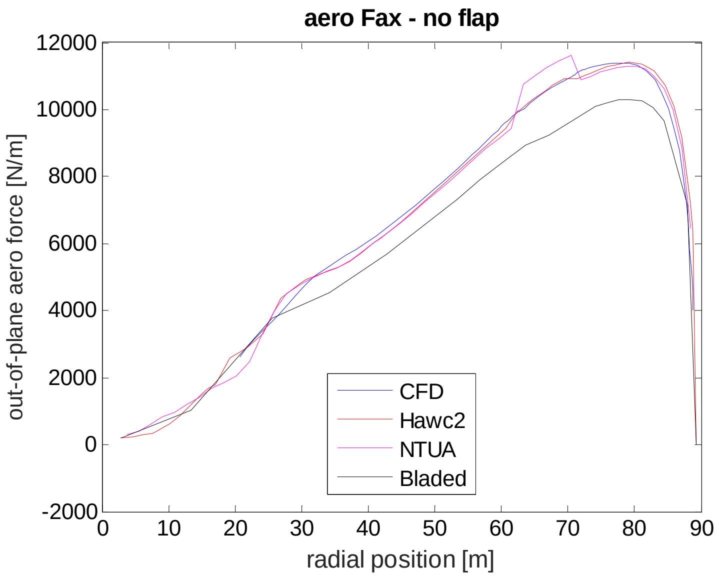

Figure 132: Axial sectional aerodynamic force, wind speed 11.4 m/s, flap angle sine 3p, flap neutral

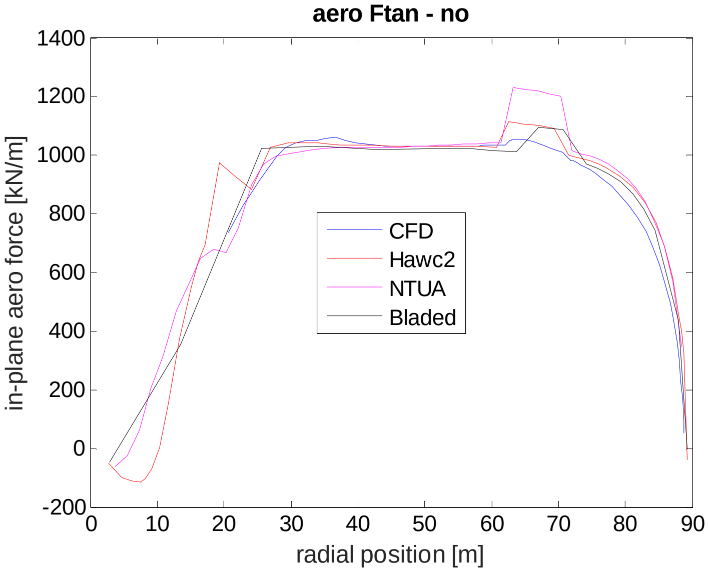

Figure 133: Tangential sectional aerodynamic force, wind speed 11.4 m/s, flap angle sine 3p, flap neutral

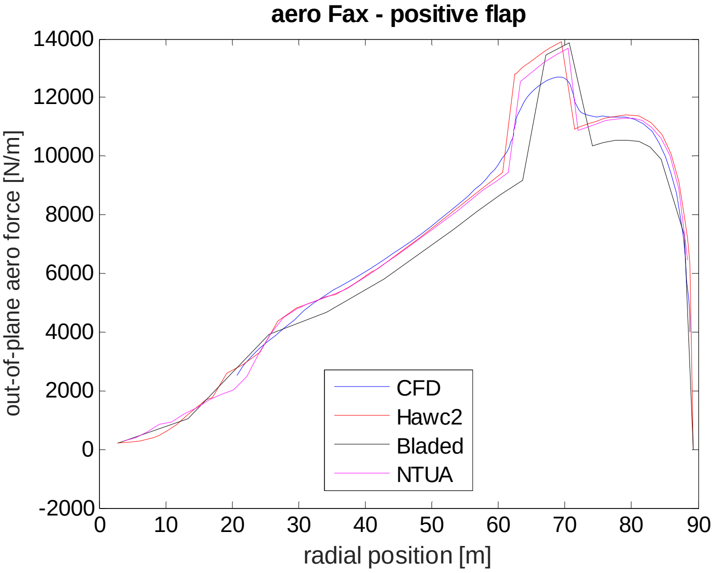

Figure 134: Axial sectional aerodynamic force, wind speed 11.4 m/s, flap angle sine 3p, flap positive

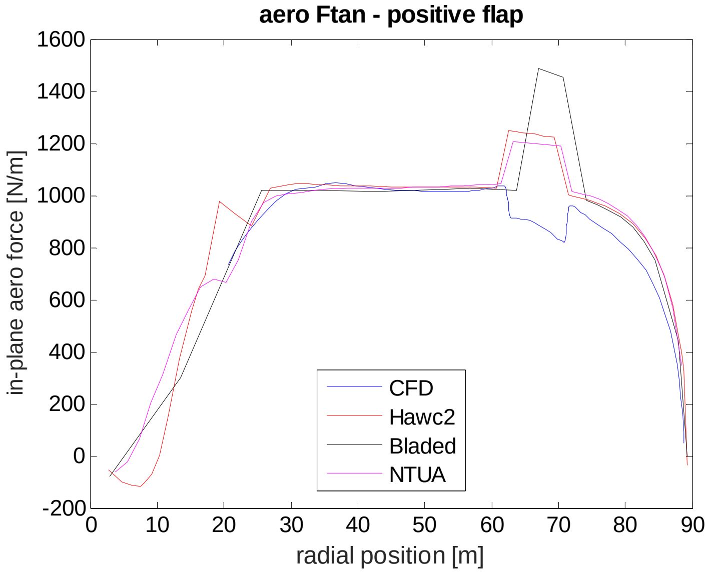

Figure 135: Tangential sectional aerodynamic force, wind speed 11.4 m/s, flap angle sine 3p, flap positive

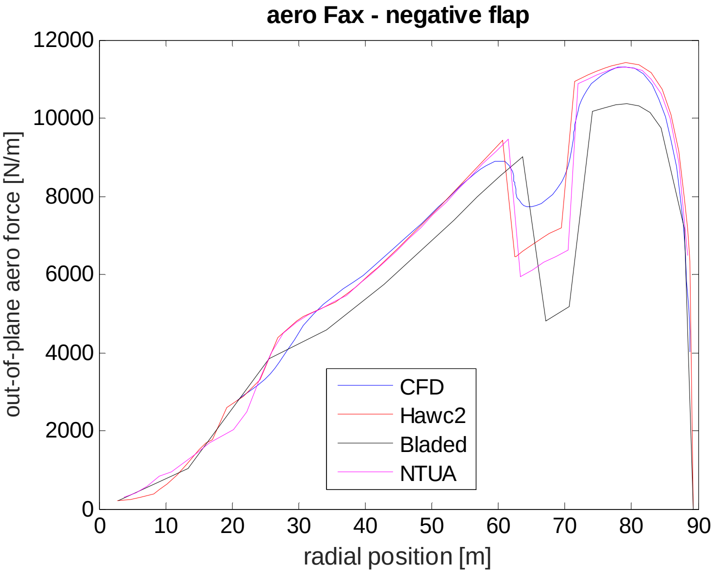

Figure 136: Axial sectional aerodynamic force, wind speed 11.4 m/s, flap angle sine 3p, flap negative

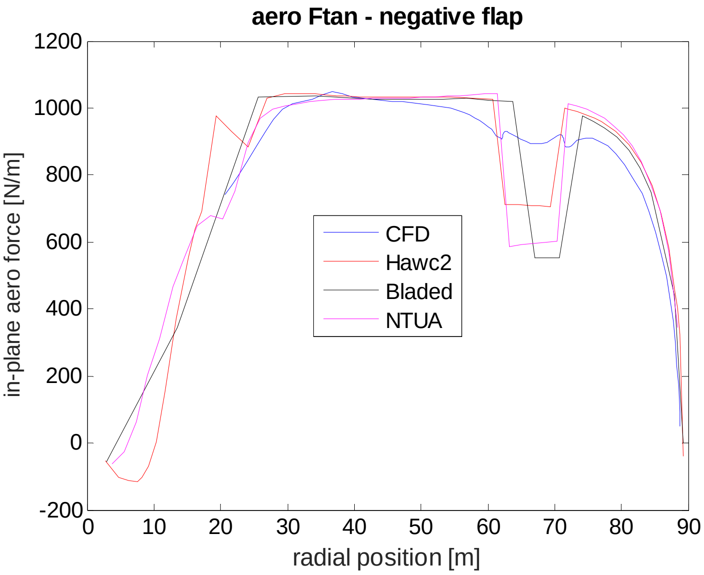

Figure 137: Tangential sectional aerodynamic force, wind speed 11.4 m/s, flap angle sine 3p, flap negative

It is seen that at higher flap frequency the sectional axial force variation in time due to the flap action are slightly overpredicted in the engineering models, but the tangential force variation is largely underpredicted by CFD due to the higher prediction of drag and a secondary variation (at 6P) is seen once per cycle. While this variation is also seen in the NTUA results, the magnitude is far smaller than the 3P variations. In terms of radial distribution, the axial force comparison shows a considerable overprediction of the variation by the engineering models, with the expected smoothing of distribution around the flap region predicted by CFD. The tangential force distribution is quite different with the local increase/decrease due to the flap action being more evident in the engineering models.

11.4m/s – 6p flap input

The flap input signal at 6p frequency is shown in Figure 138. The sectional axial (out-of-plane) and tangential (in-plane) forces are shown in Figure 139 and Figure 140. The rotor thrust and power are shown in Figure 141 and Figure 142.

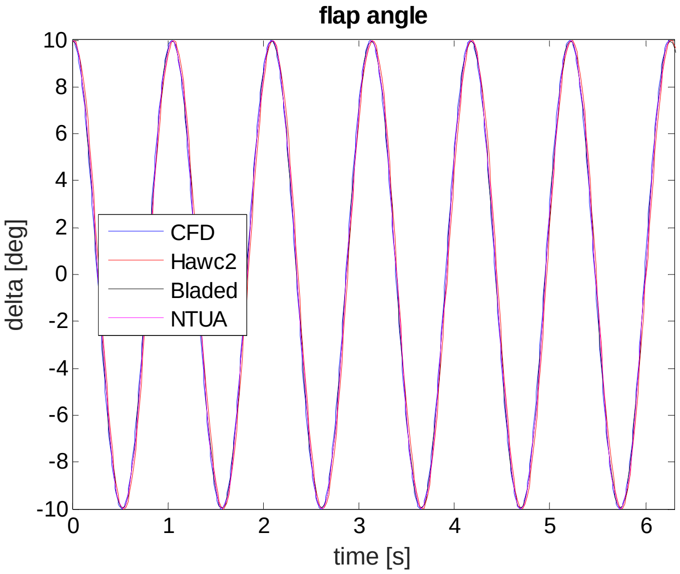

Figure 138: Prescribed Flap Angle, wind speed 11.4 m/s, flap angle sine 6p

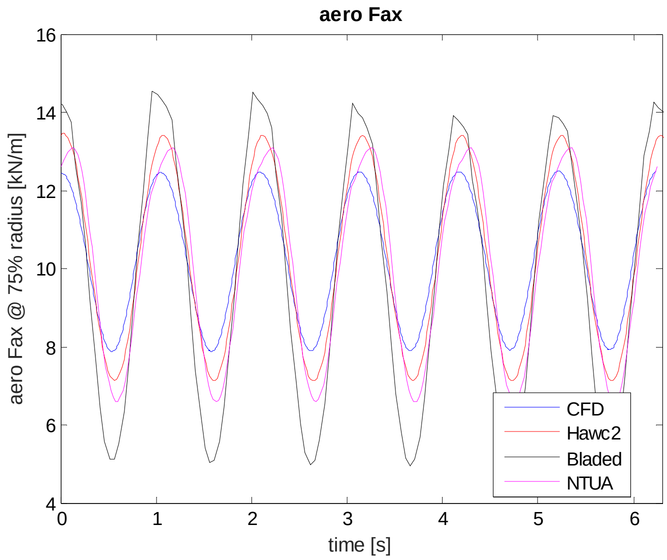

Figure 139: Axial sectional aerodynamic force, wind speed 11.4 m/s, flap angle sine 6p

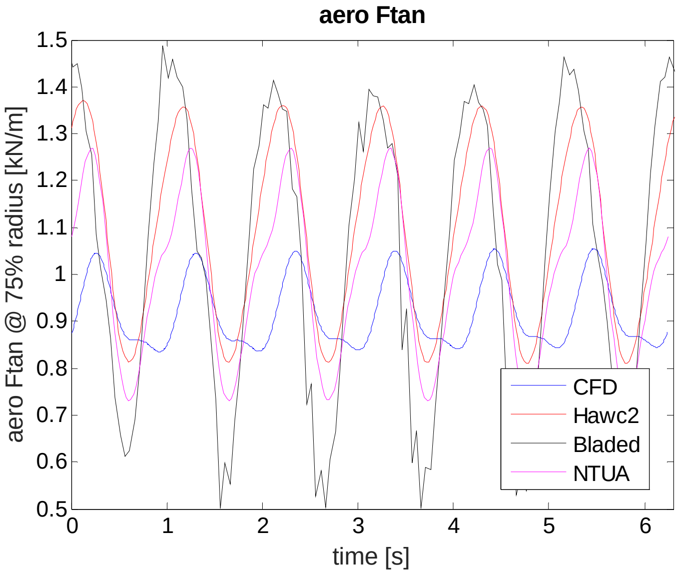

Figure 140: Tangential sectional aerodynamic force, wind speed 11.4 m/s, flap angle sine 6p

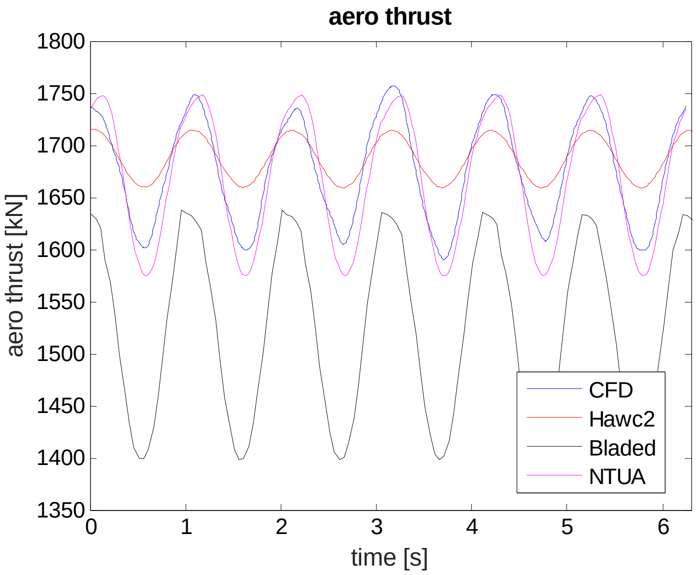

Figure 141: Rotor thrust, wind speed 11.4 m/s, flap angle sine 6p

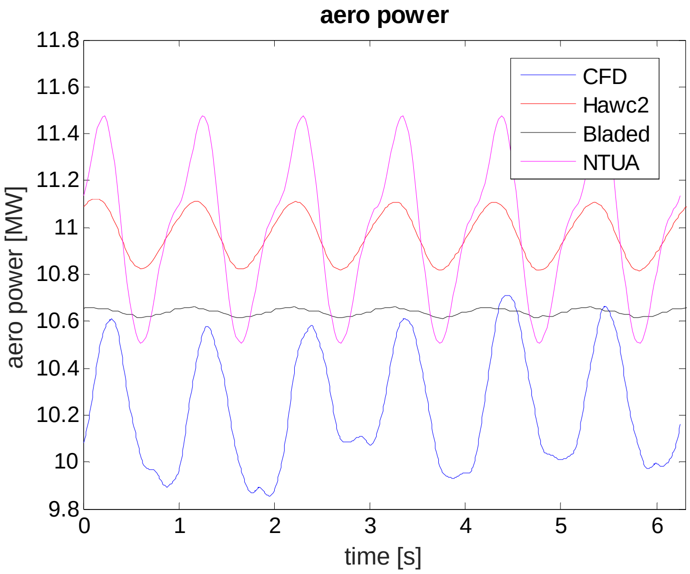

Figure 142: Rotor aerodynamic power, wind speed 11.4 m/s, flap angle sine 6p

The sectional axial (out-of--plane) and tangential (in-plane) force radial distributions are shown for the time instance when the flap is at neutral position (Figure 143 and Figure 144), for the time instance when the flap is at maximum positive position (Figure 145 and Figure 146), and for the time instance when the flap is at maximum negative position (Figure 147 and Figure 148).

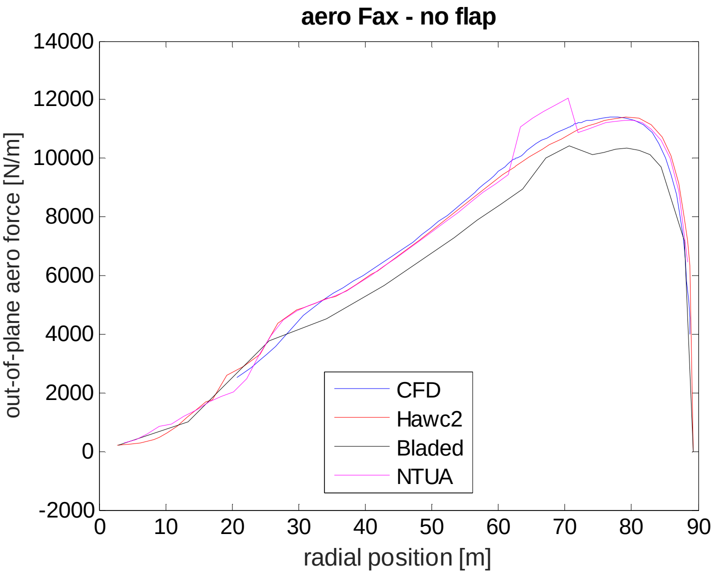

Figure 143: Axial sectional aerodynamic force, wind speed 11.4 m/s, flap angle sine 6p, flap position neutral

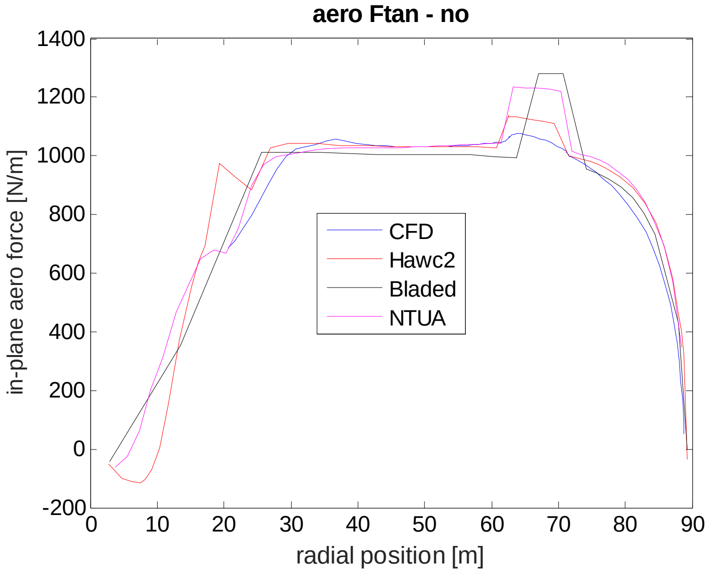

Figure 144: Tangential sectional aerodynamic force, wind speed 11.4 m/s, flap angle sine 6p, flap neutral

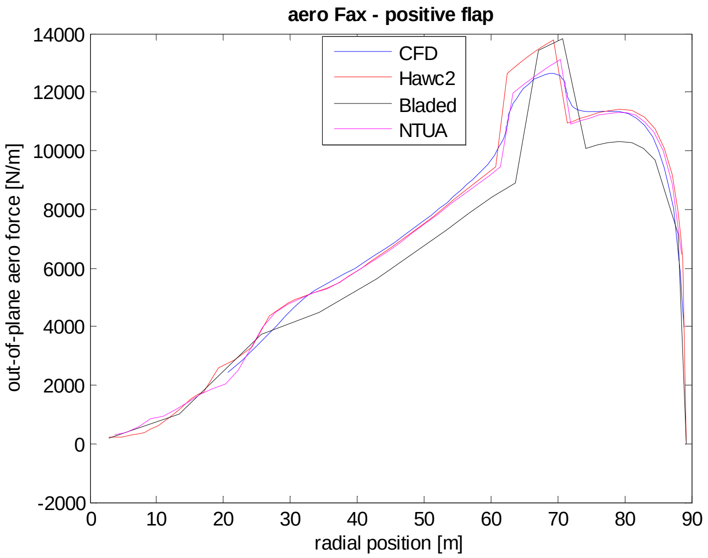

Figure 145: Axial sectional aerodynamic force, wind speed 11.4 m/s, flap angle sine 6p, flap positive

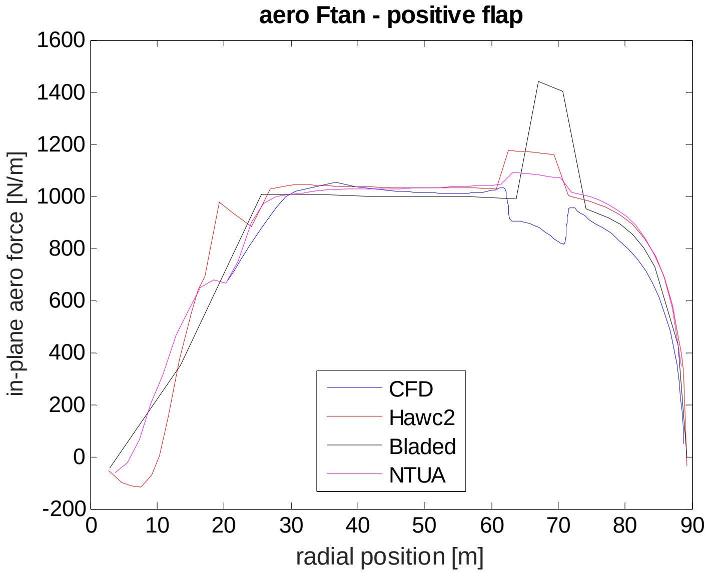

Figure 146: Tangential sectional aerodynamic force, wind speed 11.4 m/s, flap angle sine 6p, flap positive

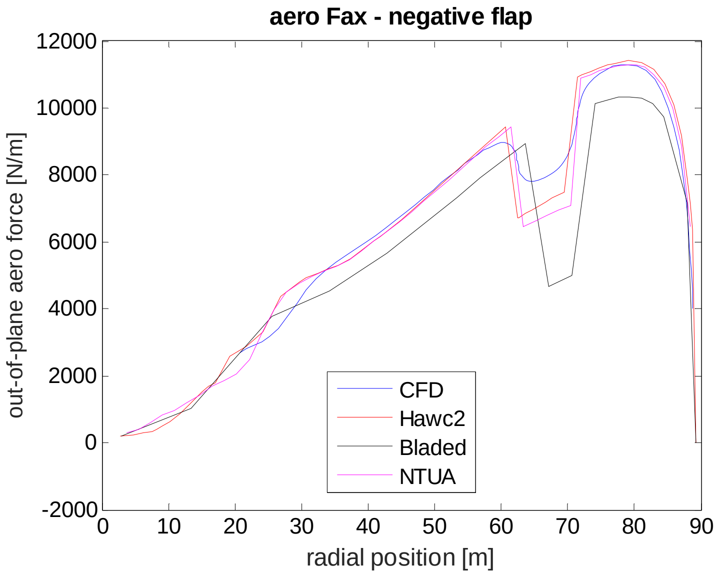

Figure 147: Axial sectional aerodynamic force, wind speed 11.4 m/s, flap angle sine 6p, flap negative

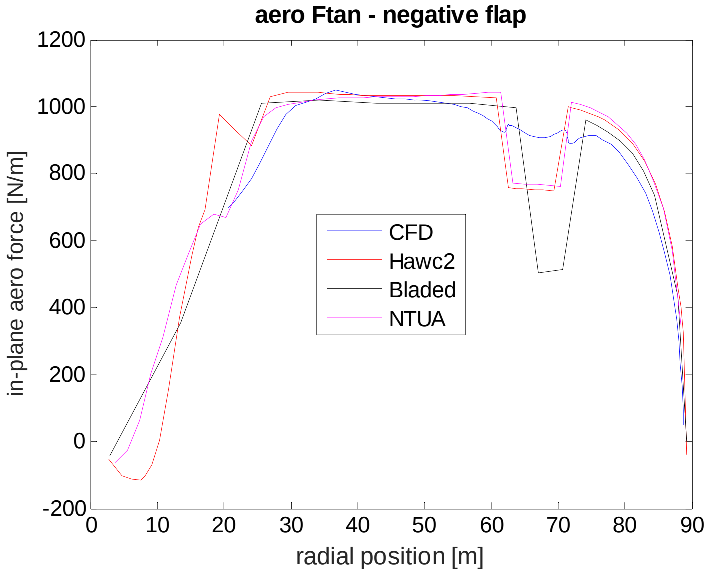

Figure 148: Tangential sectional aerodynamic force, wind speed 11.4 m/s, flap angle sine 6p, flap negative

It is seen that at even higher flap frequency the sectional axial force variation in time due to the flap action are slightly overpredicted in the engineering models with the resulting phase delay is underpredicted, but the tangential force variation is largely underpredicted by CFD due to the higher prediction of drag and a secondary variation is seen once per cycle. In terms of radial distribution, the axial force comparison shows a considerable overprediction of the variation by the engineering models, with the expected smoothing of distribution around the flap region predicted by CFD. The tangential force distribution is quite different with the local increase/decrease due to the flap action being more evident in the engineering models.

19m/s – 6p flap input

The flap input signal at 6p frequency is shown in Figure 149. The sectional axial (out-of-plane) and tangential (in-plane) forces are shown in Figure 150 and Figure 151. The rotor thrust and power are shown in Figure 152 and Figure 153.

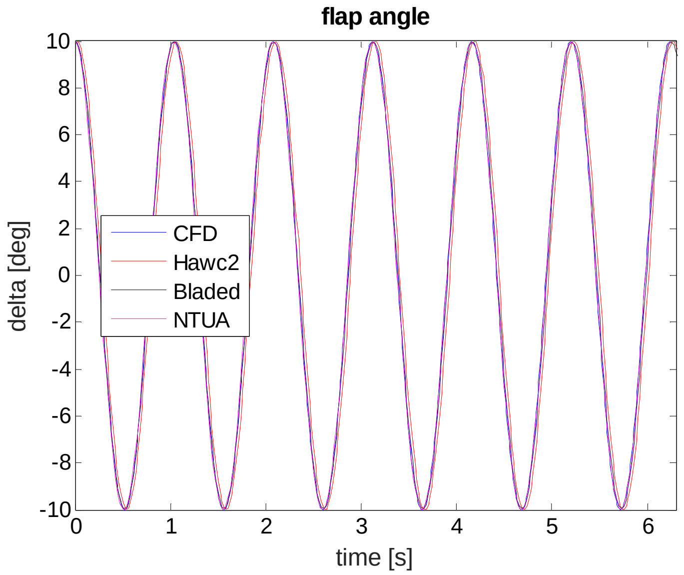

Figure 149: Prescribed flap angle, wind speed 19 m/s, flap angle sine 6p

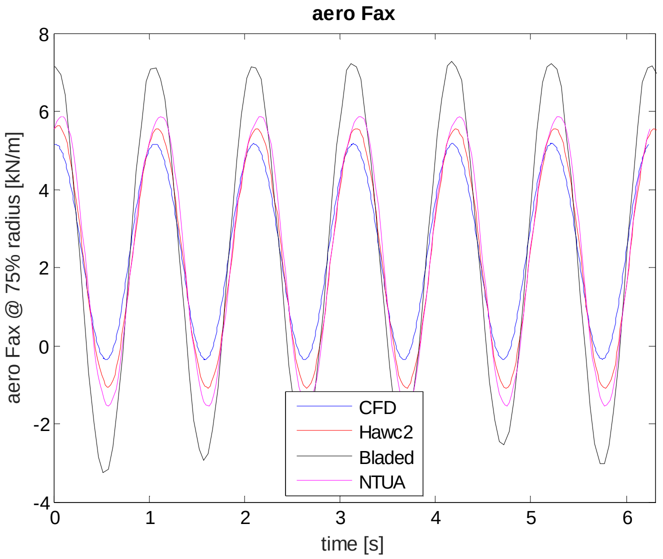

Figure 150: Axial sectional aerodynamic force, wind speed 19 m/s, flap angle sine 6p

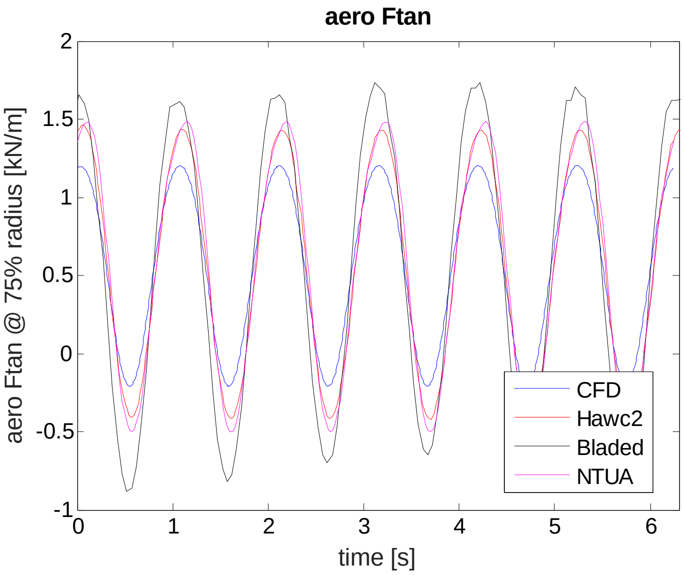

Figure 151: Tangential sectional aerodynamic force, wind speed 19 m/s, flap angle sine 6p

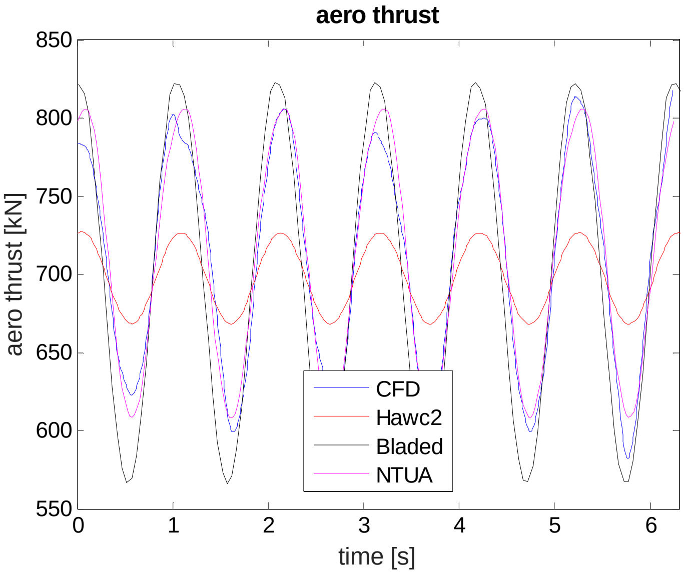

Figure 152: Rotor Thrust, wind speed 19 m/s, flap angle sine 6p

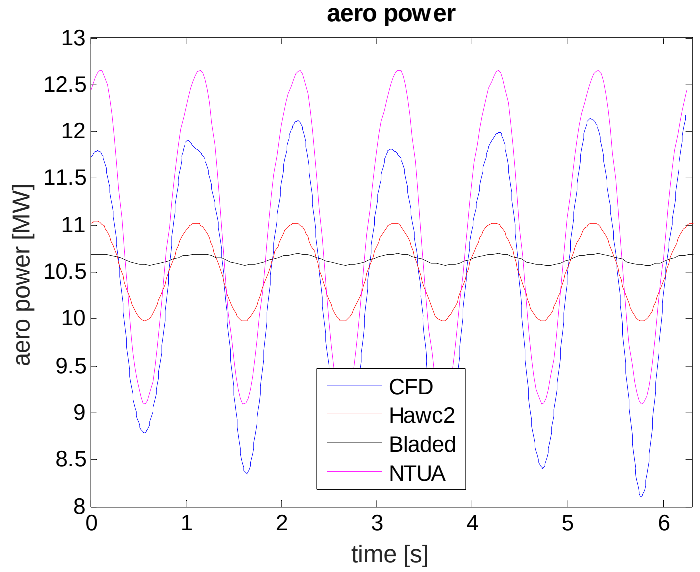

Figure 153: Rotor Power, wind speed 19 m/s, flap angle sine 6p

The sectional axial (out-of--plane) and tangential (in-plane) force radial distributions are shown for the time instance when the flap is at neutral position (Figure 154 and Figure 155), for the time instance when the flap is at maximum positive position (Figure 156 and Figure 157), and for the time instance when the flap is at maximum negative position (Figure 158 and Figure 159).

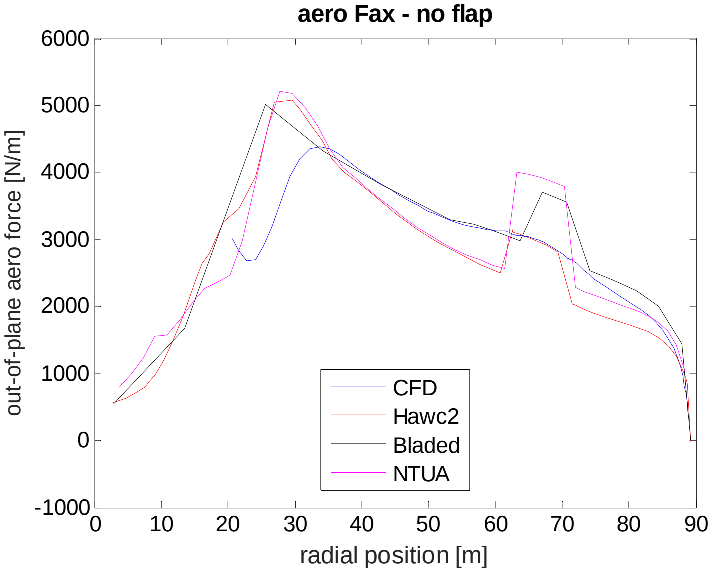

Figure 154: Axial sectional aerodynamic force, wind speed 19 m/s, flap angle sine 6p, flap neutral

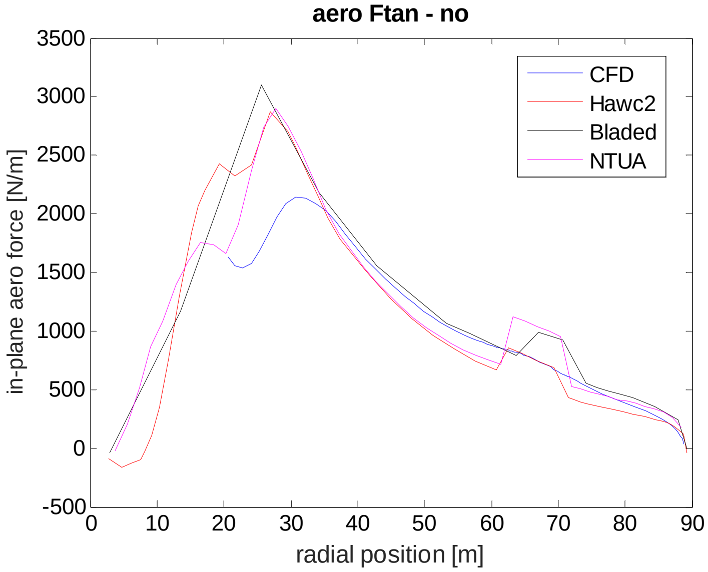

Figure 155: Tangential sectional aerodynamic force, wind speed 19 m/s, flap angle sine 6p, flap neutral

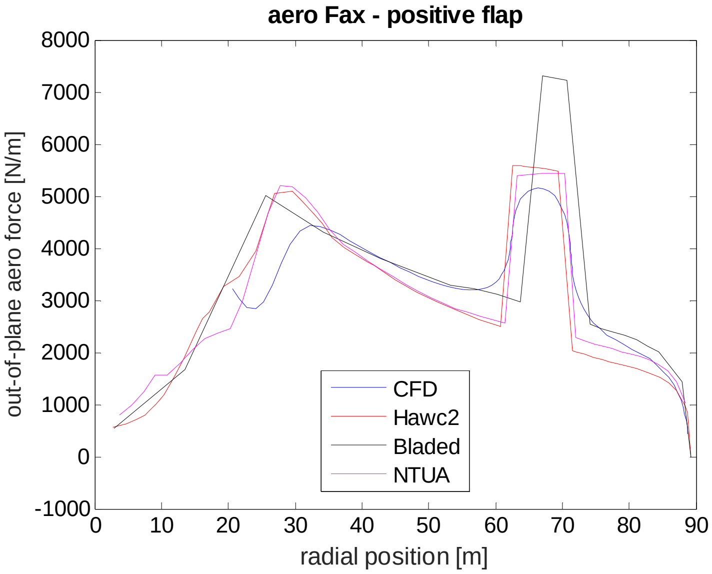

Figure 156: Axial sectional aerodynamic force, wind speed 19 m/s, flap angle sine 6p, flap positive

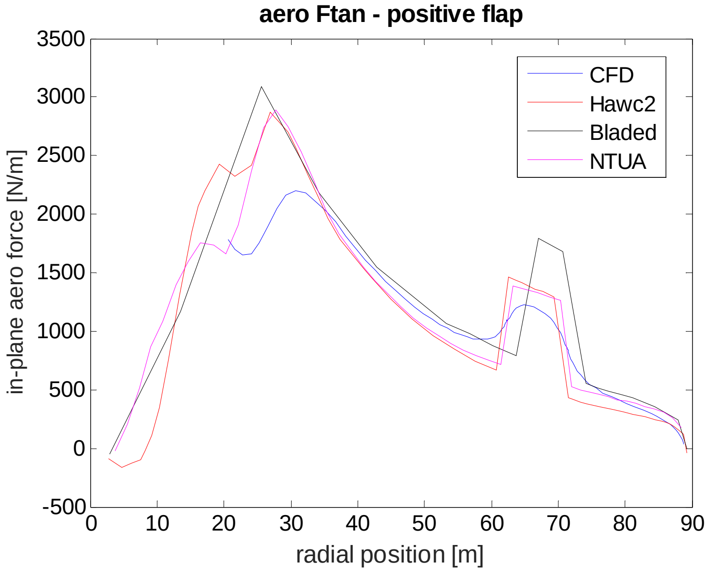

Figure 157: Tangential sectional aerodynamic force, wind speed 19 m/s, flap angle sine 6p, flap positive

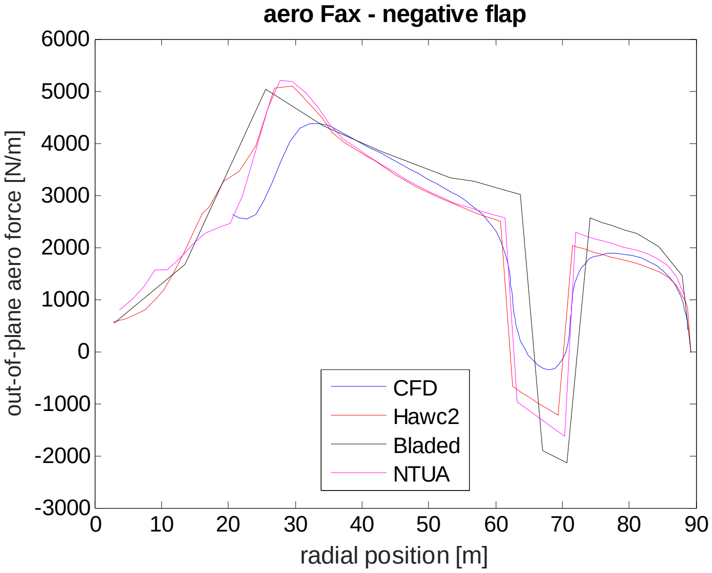

Figure 158: Axial sectional aerodynamic force, wind speed 19 m/s, flap angle sine 6p, flap negative

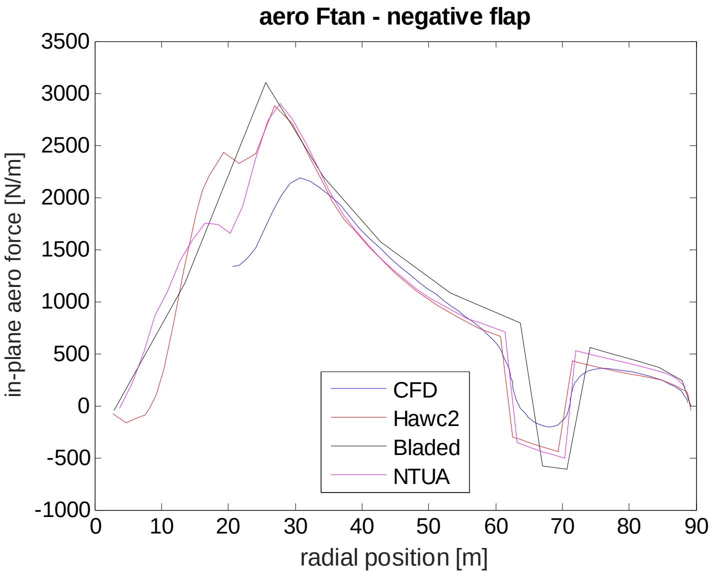

Figure 159: Tangential sectional aerodynamic force, wind speed 19 m/s, flap angle sine 6p, flap negative

In this case, both the sectional axial and tangential force variations in time due to the flap action are slightly overpredicted in the engineering models. In terms of radial distribution, both the axial and tangential force comparisons shows a overprediction of the variation by the engineering models, with the expected smoothing of distribution around the flap region predicted by CFD.

In **Table 43**, the statistics of sectional out-of-plane and in-plane loads and rotor thrust and power are shown, comparing predictions between CFD and the engineering models. Generally for all cases, the axial force variation at the flap mid-span compares, while the tangential force variation is largely overpredicted in the engineering models.

Table 43: Comparison of statistics for 1p sine, 11.4 m/s

case	CFD	HAWC2	Bladed	NTUA
Fax min [kN/m]	7.23	6.77	4.52	5.83
Fax max [kN/m]	12.95	13.56	14.67	13.75
Fax std [kN/m]	2.01	2.44	3.16	2.89
Ftan min [kN/m]	0.73	0.74	0.41	0.60
Ftan max [kN/m]	1.04	1.38	1.49	1.36
Ftan std [kN/m]	0.10	0.23	0.32	0.28
Thrust min [kN]	1557	1655	1339	1554
Thrust max [kN]	1802	1717	1614	1766
Thrust variation [kN]	81.00	22.30	80.63	76.59
Power min [MW]	9.33	10.76	10.45	10.27
Power max [MW]	10.95	11.37	10.57	11.64
Power variation [MW]	0.53	0.14	0.10	0.50

Table 44: Comparison of statistics for 3p sine, 11.4 m/s

case	CFD	HAWC2	Bladed	NTUA
Fax min [kN/m]	7.81	6.89	5.13	6.20
Fax max [kN/m]	12.52	13.54	14.06	13.43
Fax std [kN/m]	1.66	2.38	3.16	2.61

Ftan min [kN/m]	0.86	0.76	0.55	0.66
Ftan max [kN/m]	1.03	1.39	1.47	1.32
Ftan std [kN/m]	0.06	0.22	0.32	0.23
Thrust min [kN]	1595	1657	1393	1564
Thrust max [kN]	1767	1716	1621	1757
Thrust variation [kN]	52.24	21.00	80.60	69.62
Power min [MW]	10.06	10.79	10.52	10.38
Power max [MW]	10.62	11.13	10.58	11.58
Power variation [MW]	0.16	0.12	0.02	0.40

Table 45: Comparison of statistics for 6p sine, 11.4 m/s

case	CFD	HAWC2	Bladed	NTUA
Fax min [kN/m]	7.88	7.13	5.13	6.60
Fax max [kN/m]	12.49	13.46	14.55	13.09
Fax std [kN/m]	1.62	2.24	3.30	2.32
Ftan min [kN/m]	0.84	0.81	0.50	0.73
Ftan max [kN/m]	1.06	1.37	1.48	1.27
Ftan std [kN/m]	0.07	0.19	0.30	0.17
Thrust min [kN]	1590	1659	1398	1575
Thrust max [kN]	1757	1715	1638	1748
Thrust variation [kN]	50.46	19.63	84.87	61.95
Power min [MW]	9.86	10.82	10.61	10.51
Power max [MW]	10.71	11.12	10.66	11.48
Power variation [MW]	0.25	0.10	0.02	0.31

Table 46: Comparison of statistics for 6p sine, 19 m/s

case	CFD	HAWC2	Bladed	NTUA
Fax min [kN/m]	-0.36	-1.09	-3.25	-1.54
Fax max [kN/m]	5.17	5.64	7.10	5.87
Fax std [kN/m]	1.96	2.38	3.63	2.66
Ftan min [kN/m]	-0.21	-0.42	-0.88	-0.50
Ftan max [kN/m]	1.20	1.46	1.74	1.48
Ftan std [kN/m]	0.50	0.66	0.90	0.71
Thrust min [kN]	582.1	668.1	566.3	608.4
Thrust max [kN]	818.0	727.4	822.7	805.9
Thrust variation [kN]	69.38	20.91	90.66	70.99
Power min [MW]	8.11	9.98	10.58	9.09
Power max [MW]	12.17	11.04	10.69	12.65
Power variation [MW]	1.25	0.38	0.04	1.27

6.5 Conclusions

- Overall, the prediction of the variation of the flap mid-span sectional axial force compares fairly between CFD and the engineering models.
- The flap mid-span tangential force is largely over-predicted in the engineering models.
- Compread to HAWC2, CFD largely overpredicts the rotor thrust variation, while power variation compares better at higher flap frequencies.

- Of the engineering models, it is seen that the tangential force overprediction of Bladed is the highest, however it remains within reasonable bounds.
- The response of the engineering models comes closer to the CFD predictions at higher wind speeds, which is also the region where trailing edge flaps are expected to be used to the greatest extent.
- The close correlation between the axial response of the engineering models and of CFD is of greater interest since blade flapwise loads are specifically targeted by the controllers used in this report. For more advanced applications, closer attention is required to be devoted to correlating other aerodynamic phenomena.
- Further insight into 3D aerodynamic effects are expected in the Deliverable D3.2 of the AVATAR project (www.eera-avatar.eu).

7 CONCLUSIONS

In the previous deliverable, the active load control concept of trailing edge flaps was shown to have the highest technology-readiness level for improving wind turbine rotor design through the attenuation of blade loads. In this report, different numerical environments were used to analyse the load reduction potential of the trailing edge flaps, and to identify modifications necessary for its in-field implementation. The report identifies various research directions necessary for an in-field implementation of the trailing edge flap rotor concept.

As a high-fidelity benchmark, CFD was used to simulate the full turbine in steps. An unsteady aerodynamic simulation was performed, and it was found that for frequencies upto 1P, unsteady effects play no role in the aerodynamic response. Beyond this frequency, aerodynamic hysteresis becomes increasingly visible in the results. This points towards a need for including unsteady corrections in engineering codes for simulating flap behaviour. These results also indicate that there exists an aerodynamic bandwidth for the flap actuator which will limit high-frequency load alleviation of the flap actuator. Further, it is seen that sharp changes in the flap command signal can lead to extremely high transient aerodynamic forces. To mitigate such forces, future flap control algorithm need to incorporate constraint handling with limits on demanded flap rates.

Three engineering codes were used to investigate flap controllers. For pure flap control, and for small spanwise sizes of flaps (10%), an average blade load reduction across all cases of 12% is observed. On the other hand, when combined with pitch control, and for an increased spanwise size of the flaps (30%), blade load reductions upto 25% are observed. It is to be noted that with increasing blade fatigue load reduction, extreme loads in the turbine may increase. Future investigations should focus on the reduction of loads (both fatigue and extreme) across all turbine components simultaneously.

Three different extensions to the basic flap/pitch controller combination are investigated:

- Idling controller: High wind speeds beyond cut out can be directly responsible for extreme turbine loads. It is shown that a flap controller can mitigate these loads.
- Frequency-separated flap/pitch controller: If the pitch controller is designed only for 1P loads, with the flap controller targetting higher frequencies, pitch system damage is substantially reduced, while the flap controller does not hit its deployment angle limits, thereby achieving the same load reduction potential with less actuator stress.
- Subspace predictive repetitive control: This model-free adaptive algorithm is shown capable of tuning turbine flap controllers online using controller data.

Finally, a comparison has been made across the engineering codes and CFD results for a purely aerodynamic case to verify the results of the previous chapters. Axial loading results in all cases are very close to each other, and since the focus of this report has been on blade flapwise load reductions, the degree of fidelity achieved by the engineering codes is considered adequate and the load reduction potential results are considered to be of acceptable accuracy. For the engineering codes, unsteady 3D corrections are important. These corrections are implemented in the hGAST and in HAWC2, but not in Bladed, and the improvements achieved through such corrections are clearly visible in the results. To further align CFD and the engineering codes, 3D trailed wake interaction effects that producing smoothening of the CFD results need to be considered by the engineering models. Also, attention needs to be focussed on the alignment of tangential and drag-related forces across the numerical codes.

In conclusion, verified numerical simulations show that rotor load reductions of 8-25% can be achieved with the integrated use of trailing edge flap actuators, which is currently the most technology-ready advanced load reduction concept available.

Future work needs to investigate the causes of discrepancy between the numerical simulation results, with focus on the improvement of 3D corrections using the lessons learnt from CFD. The results of these investigations need to be verified against the prototype experiments that will be conducted for the next deliverable. Several alternatives for optimising the performance of combined pitch and flap load controllers have been demonstrated in this report, these controllers need to be tested thoroughly for all major design-driving load cases occurring during the wind turbine lifetime. Further, validating the novel controllers in a real-time experimental environment will ensure a proof of concept for a successful in-field implementation of combined load control.